ZTF-FCT
Zientzia eta Teknologia Fakultatea
Facultad de Ciencia y Tecnología

eman ta zabal zazu

Universidad del País Vasco
Euskal Herriko Unibertsitatea

Optical functionalities of liquid crystals: laser devices and nonlinear optics

by

Gerardo Sanz Enguita[*]

Advisors

César Luis Folcia Basa[*]

and

Josu Ortega Aperribay[**]

[*]Department of Condensed Matter Physics

[**]Department of Applied Physics II

A thesis to apply for the degree of Doctor of Physics, mention "Doctor Europeus"

October 2016

Resumen

Funcionalidades ópticas en cristales líquidos: dispositivos láser y óptica no lineal

Hoy en día los cristales líquidos (CLs) están presentes en múltiples aplicaciones cotidianas. Habitualmente en dispositivos visuales como pantallas de móviles, televisores o relojes. El presente trabajo se centra en dos propiedades ópticas de los mismos, ambas con un amplio potencial tecnológico aunque no tan extendidas entre las aplicaciones cotidianas. Una de las propiedades es la capacidad que las fases colestéricas tienen para la amplificación de luz y por lo tanto para la emisión láser. A esta propiedad le dedicaremos la mayor parte de esta tesis, en concreto los capítulos 2, 3, 4 y 5. La segunda propiedad a la que nos referimos es la gran capacidad de respuesta óptica no lineal. A esta propiedad le dedicaremos el capítulo 6.

En el capítulo 1 se hace una descripción general del estado líquido cristalino, describiéndose las principales moléculas que componen los cristales líquidos y las mesofases más habituales que estos presentan. En particular nos centramos únicamente en aquellas mesofases que son relevantes para este trabajo.

Como ya se ha dicho, los capítulos 2, 3, 4 y 5 tratan sobre láseres de cristal líquido colestérico (CLC). Estos materiales presentan un ordenamiento helicoidal de sus moléculas que le confieren propiedades fotónicas. El capítulo 2 es una amplia introducción a este tipo de dispositivos. En él, se describe el fundamento teórico necesario para comprender el origen de la "photonic band gap" o banda prohibida (BP). A su vez se muestra como la existencia de la BP da lugar a una peculiar distribución en la densidad de los modos ópticos dentro del CLC, y como esto puede usarse para la emisión láser; para posteriormente mostrar de forma detallada un caso práctico de emisión láser. Al final del

capítulo se expone un modelo de ecuaciones cinéticas propuesto recientemente para describir el funcionamiento de dichos láseres. Este modelo es típico de láseres de estado sólido. En él, las peculiaridades de la cavidad fotónica del CLC se introducen a través del tiempo de vida media de un fotón dentro de la misma, τ_c. Dicho modelo es muy importante para esta tesis ya que posteriormente es usado en los capítulos 3, 4 y 5.

El capítulo 3 estudia la dependencia que la eficiencia de estos láseres tiene en distintas variables de la muestra; como por ejemplo, el espesor, el así llamado coeficiente de pérdidas distribuidas (β) o la densidad de moléculas de colorante (N). Dicho estudio se realiza tanto desde el punto de vista experimental como del teórico y se centra principalmente en el espesor de la muestra. Para esto, primero se presentan una serie de medidas experimentales que muestran las dependencias del umbral de emisión láser y de la eficiencia láser con el espesor de la muestra. Posteriormente, mediante simulación numérica del modelo descrito al final del capítulo 2 se comparan nuestros resultados experimentales con los derivados de dicho modelo. Cabe destacar que, para esto, previamente se realizan algunas mejoras al modelo propuesto. No obstante, antes de obtener los resultados teóricos y con el fin de comprender mejor el funcionamiento de estos dispositivos, también simulamos la evolución de población de los distintos niveles energéticos del colorante. Dicha evolución de poblaciones, permite una buena comprensión de la dinámica del láser. Posteriormente, se usa dicho sistema de ecuaciones para hallar expresiones analíticas que relacionen el umbral de laseo y la eficiencia láser con distintos parámetros de la muestra como, por ejemplo, el espesor, N o β. Una vez deducidas estas expresiones se comparan los resultados derivados de las mismas con los obtenidos experimentalmente y mediante simulación numérica. Se encuentra una gran concordancia entre los 3 métodos. Los 3 procedimientos muestran que existe un espesor para el cual el umbral de emisión láser es mínimo y otro

espesor, cercano al anterior, para el que la eficiencia láser es máxima. Si bien el espesor para el mínimo umbral de emisión láser no está bien definido dentro del error experimental, sí lo está el espesor para el cual la eficiencia es máxima. Por otro lado, de las predicciones teóricas se desprende que el espesor óptimo para estos dos parámetros apenas depende de N y de β; al menos dentro de rangos razonables. Además mediante dicho modelo se comprende con claridad por qué la existencia de un nivel triplete del colorante imposibilita la obtención de láseres continuos.

En el capítulo 4 se estudia la cinética de los pulsos de emisión del láser. En particular estudiamos el perfil temporal de los pulsos emitidos en función de la energía de bombeo. De nuevo, este estudio consta de una parte experimental y otra teórica. El enfoque teórico se realiza mediante la simulación numérica del modelo de ecuaciones cinéticas descrito en el capítulo 2 y usado en el capítulo 3. Tanto los resultados experimentales como los teóricos muestran como muy por debajo del umbral láser la anchura de los pulsos emitidos es similar a la de la bomba. Conforme aumenta la energía de bombeo los pulsos se estrechan hasta alcanzar una anchura mínima justo en el umbral. Cabe destacar que en nuestro caso la anchura experimental del mínimo estaba limitada por la resolución del fotodiodo empleado. Por encima del umbral, del mismo modo que ocurre en láseres de estado sólido, aparecen oscilaciones de relajación. Dichas oscilaciones ocurren de manera un tanto irregular debido a perturbaciones térmicas y mecánicas. Además, la anchura media de los pulsos va aumentando conforme aumenta la energía de bombeo. A su vez, abordamos el controvertido problema de explicar la alteración que experimenta el espectro de fluorescencia del colorante cuando este es introducido en el CLC. Según los resultados experimentales de algunos autores, el tiempo de vida de fluorescencia (τ_f) del colorante no se ve alterado por la cavidad fotónica. Usando el mismo modelo teórico que en los casos anteriores, mostramos que los pulsos fluorescentes que

emite la muestra son inversamente proporcionales al tiempo de vida radiativo del colorante ($\propto 1/\tau_r$). A su vez la duración de dichos pulsos viene regida por τ_f. Por lo tanto, las variaciones de los tiempos de vida radiativos y no radiativos deben compensarse entre sí.

A pesar de su potencial tecnológico, estos láseres adolecen de un gran inconveniente: se degradan y dejan de funcionar en tiempos relativamente cortos. Es por esto que en el capítulo 5, el último dedicado a láseres de CLC, tratamos de determinar los orígenes de este deterioro. Como primer paso para caracterizar dicha degradación, se mide como varían los espectros de emisión láser y de fluorescencia conforme la muestra se degrada. La causa última de dicho deterioro es la degradación de las moléculas de colorante debido a su calentamiento. Esta degradación tiene una doble cara. Por un lado disminuye la densidad de moléculas de colorante operativas (N) y por otro lado las moléculas degradadas actúan como centros dispersores aumentando β vía dispersión. Volviendo de nuevo al modelo de ecuaciones cinéticas vemos que en nuestro caso particular la degradación se explica perfectamente debido a una disminución de N. No obstante, en los rangos de concentración habituales una disminución de N, como la observada, apenas afectaría a la operación del láser. Curiosamente, nuestros datos experimentales muestran como paralelamente a la degradación láser se produce un aumento de la luz de bombeo dispersada, lo que presumiblemente aumentará β. Por este motivo realizamos un estudio experimental para caracterizar este aumento de la dispersión Asumiendo un modelo de dispersión de Rayleigh se observa que, a pesar de que en el presente caso el aumento de β queda totalmente eclipsado por la disminución de N, la dispersión puede, en determinados casos, anular la acción láser por sí solo. En otras palabras, el aumento de β no debe de ser ignorado. De todos modos, en última instancia ambos fenómenos son causados por la degradación de las moléculas de colorante. En parte, el problema puede abordarse mediante la

mejora de los parámetros de la cavidad láser de CLC. Esto permitiría usar fuentes de bombeo de baja potencia. Sin embargo, ya que el origen del problema de la estabilidad de láser es el calentamiento de las moléculas de colorante, el rendimiento de los láseres CLC debería mejorar notablemente usando colorantes con bajos rendimientos cuánticos para el nivel de triplete. En este sentido, el uso de moléculas fluorescentes especiales con poblaciones pequeñas del nivel triplete ha permitido, recientemente, fabricar láseres de CLC de onda continua. Una vez más, queda claro el efecto pernicioso del estado triplete. De todos modos cabe destacar que, manteniendo un bombeo con baja frecuencia de repetición y energías razonables, esta degradación no ocurre o es despreciable. De hecho para la mayoría de las medidas de esta tesis se han usado muestras que han resultado operativas durante muchos meses e incluso años.

Hasta aquí, la tesis ha tratado sobre CLCs y su peculiar comportamiento fotónico. No obstante, los CLs poseen otras propiedades ópticas interesantes entre las que destaca la capacidad de presentar gran respuesta óptica no lineal. Entre ellas hemos estudiado la generación de segundo y tercer harmónicos (GSH y GTH). Al igual que la amplificación de la luz, estas propiedades son de gran interés tecnológico. En el último capítulo de esta tesis, el 6, tratamos dichas propiedades. Para ello, en primer lugar se describe el trasfondo teórico de estos fenómenos no lineales así como las cualidades que debe presentar un CL para presentar GSH y GTH. Posteriormente se estudia la GSH en un CL cuya geometría molecular ha sido diseñada expresamente para optimizar determinadas componentes de su tensor de SH. A este CL se lo conoce como 'trímero'. Los resultados muestran que, hasta la fecha, se trata del CL más eficiente para la GSH, al menos bajo condiciones no resonantes. Además, para completar dicha caracterización, se relacionan las propiedades de respuesta no lineal a nivel molecular con los resultados experimentales a nivel macroscópico.

Se obtiene un buen acuerdo entre ambos resultados. Por último se comprueba que además de una gran capacidad para la GSH, nuestra molécula también se muestra muy eficiente en la GTH.

Table of contents

Foreword

Nowadays the society would hardly be able to recognize itself without liquid crystals. Liquid crystals (LCs) are present in devices we use every day, like mobile phones, computers, watches, TVs, etc., whose displays are based on different LC technologies. Furthermore, many other devices have been designed to make use of specific properties of LCs. Thus, LCs are used, for example, in the development of ultrafast light modulators[1], lasers[2], or photovoltaic cells[3, 4].

This dissertation deals with optical properties of LCs. Particularly it is focused on two features of technological interest. On the one hand, it concerns with the ability of cholesteric liquid crystals (CLCs) for coherent light amplification (lasing). On the other hand, we study the capability for nonlinear optical response of LCs.

First of all, in Chapter 1 we give a general description of the LC state of matter. In such introduction we describe the most common mesophases that these materials present, paying special attention to those that will exhibit the materials studied in this dissertation.

In a general framework, this work deals with two different topics. The major part of this dissertation is concerned with CLCs. The key feature of these materials is the existence of a photonic band-gap for visible light. We focus on such feature together with its ability for light amplification. In this respect, in Chapter 2 we describe in detail the theoretical background of CLC lasers and the features that a CLC must exhibit in order to be exploited for lasing. Besides, we present an experimental example of such behavior. Then, Chapters 3, 4 and 5 are dedicated to the study of some particular aspects of such devices. Particularly, in Chapter 3 we study the dependence of the CLC laser

performance on different parameters, especially on sample thickness. Next, in Chapter 4 we focus in the kinetics of laser emission in CLC lasers. Finally, in Chapter 5 we throw some light into the problem of laser degradation, which is one of the main drawbacks of these devices.

On the other hand, the last chapter of this dissertation deals with a different topic. This is, nonlinear optics. Particularly we focus on second harmonic generation (SHG). In this respect, the theoretical background of SHG is explained and a novel trimer compound, exhibiting a SmC* ferroelectric mesophase, is studied. Besides, third harmonic generation was also observed and characterized in the isotropic phase of this material.

The results presented in this dissertation highlight the promising future that LCs deserve as key tools for new technologic devices.

[1] N. Collings, W. A. Crossland, P. J. Ayliffe, D. G. Vass, and I. Underwood, *Applied Optics*, **28**, 4740, (1989).

[2] V. I. Kopp, Z.-Q. Zang, and A. Z. Genack, *Opt. Lett*. **23**, 1707 (1998).

[3] M. Carrasco-Orozco, W. C. Tsoi, M. O'Neill, M. P. Aldred, P. Vlachos and S. M. Kelly, *Adv. Mat.* **18**, 1754, (2006).

[4] L. Schmidt-Mende, A. Fechtenkötter, K. Müllen,E. Moons, R. H. Friend, J. D. MacKenzie, *Science*, **293**, 1119, (2001).

CHAPTER I

INTRODUCTION TO LIQUID CRYSTALS

1.1 Introduction

Liquid crystals (LC) refer to an intermediate state of matter between solids and liquids so they also exhibit properties between those of an isotropic liquid and a crystalline solid. LC phases (mesophases) lack of long-range tridimensional order, as that shown by solid crystals. But unlike liquids, LCs show long-range orientational order. In addition, some LC mesophases also show positional order in one or even in two dimensions. In some especial cases the periodicity can be in three dimensions as for example in blue phases[1, 2]. A LC material can present different mesophases under different conditions. When a compound forms LC mesophases by the addition of a solvent, we say that it is a lyotropic LC[3]. When different mesophases appear when varying temperature the compound is said to be thermotropic. This dissertation will only deal with thermotropic compounds. A more exact definition is that of P.G. de Gennes: '*They are systems whose components keep "liquid order" in at least one direction in space and a certain degree of anisotropy*'[4].

There are no written rules about what kind of materials will show LC phases but it is known that molecules must possess a high structural anisotropy; thus their shape is an important precondition. So they must present an anisotropic geometry in order to promote a preferred orientation.

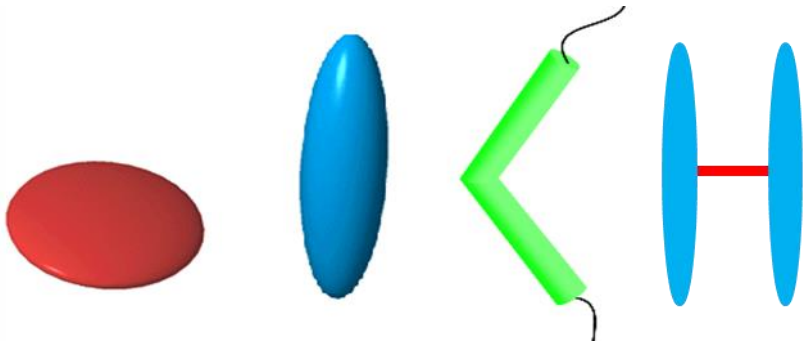

Fig. 1. Typical shape of LC molecules. From left to right: discotic, calamitic or rod-shaped, banana and H-shaped molecules.

Traditionally LCs have been divided into calamitic when they are composed of elongated or rod-shaped molecules, and discotic when composed of disk-shaped molecules. However, other geometries have also been studied as those of bent-core LCs (with boomerang or banana shape)[5, 6, 7] or H-shaped compounds[8]. In fact, as we will see further, in this dissertation we will deal with a new type of H-shaped molecule. Fig. 1 shows a sketch of some of these typical molecular compounds.

In this chapter we are going to introduce briefly the main characteristics of the most common LC phases, paying especial attention to the mesophases involved in the different studies carried out in this dissertation.

1.2 LC phases

In a mesophase molecules can flow freely as in a liquid whereas certain long-range order is maintained. Depending on what type of order is kept several clearly different mesophases have been identified. Some of the most interesting ones are: Nematic (N), smectic A (SmA) and smectic C (SmC) phases[4] (see Fig. 2). In addition, the mentioned mesophases can be chiral or non-chiral. The chirality in a mesophase is indicated by the superscript *. In the majority of cases, chiral mesophases appear when a chiral dopant is added or when the constituent molecules of the mesophase are chiral themselves. A molecule is said to be chiral when it cannot be superposed onto its mirror image (see Fig. 3).

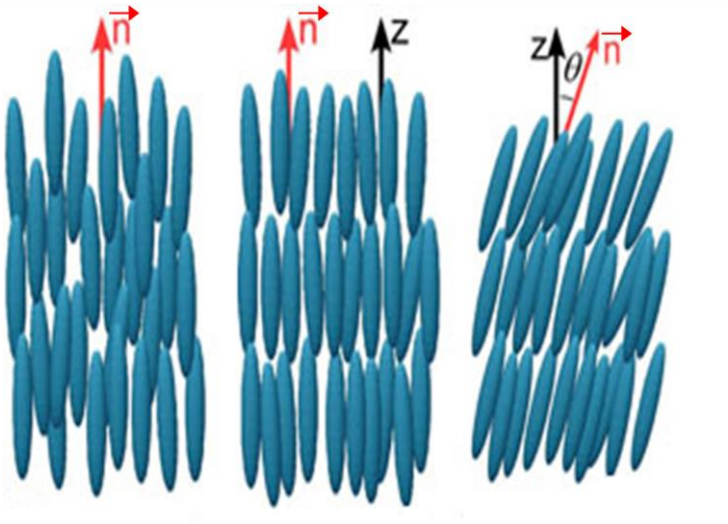

Fig. 2. Typical LC phases of a calamitic compound. From left to right: Nematic phase (only orientational order), smectic A phase (orientational order and arrangement in layers) and smectic C phase (also orientational order and arrangement in layers but molecules are tilted within layers). **n**, **z** and θ denote the molecular director, the layer normal and the tilt angle respectively.

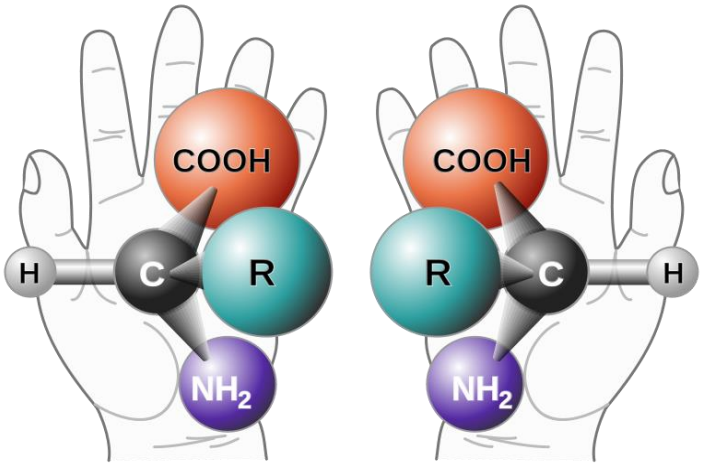

Fig. 3. A typical example of chirality is found in our hands.

We now give a more detailed description of several mesophases.

1.2.1 The N phase

In N phases molecules present liquid order. The centers of mass of the molecules are random in space and the translational movement of the

molecules is free. Thus, this phase has no long-range positional order. Nevertheless, molecules tend to keep certain directional order, pointing along a preferred direction. Due to this fact, we say that N phases exhibit orientational order. The preferred direction is known as the director and is represented by **n**. This phase is depicted in Fig. 2. Liquid crystal molecules do not have rotational symmetry around their long axis because they are like 'boards' rather than like 'cylinders'. However, when they are packed in a N phase, their short axes do not present orientational order, i.e. they rotate freely along the long axis. As a consequence, N phases always have rotational symmetry around the director. In addition, N phases present the so-called head-tail invariance. This can be understood as the invariance with respect to 180º rotations around an axis perpendicular to **n**. Therefore the point symmetry group assigned to them is ∞/mm (in international notation)[4], which prevents spontaneous polarization to appear.

The degree of order in N phases is characterized by an order parameter denoted by S:

$$S = \frac{1}{2}\langle 3\cos^2(\theta) - 1\rangle\,, \tag{1.1}$$

where θ is the angle between the long axis of each molecule and **n** (see Fig. 4) and <> denotes statistical average.

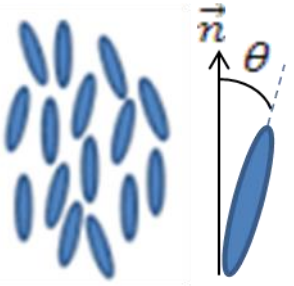

Fig. 4. Scheme of the nematic phase and of the orientational order of its individual molecules.

If we dissolve in the nematic liquid a molecule that is chiral the structure undergoes a helical distortion. The same distortion occurs if the material is composed by pure chiral molecules. This gives rise to the so-called cholesteric nematic phase (N*).

1.2.2 The N phase*

The N* phase is locally nematic and was first discovered in 1888[9]. Again, chiral nematic phases (CLC) present liquid order and the molecular orientation shows a preferred axis. However, the director is not constant in space but describes a helix whose axis is perpendicular to the director. The helix is right-handed or left-handed depending on the molecular chirality. The distance over which the LC molecules undergo a full 360º twist is known as the chiral-pitch P (see Fig. 5). The pitch can be varied by means of several methods as, for example, adding different concentrations of chiral dopants or by varying the temperature. The symmetry point group associated to this phase is ∞/mm.

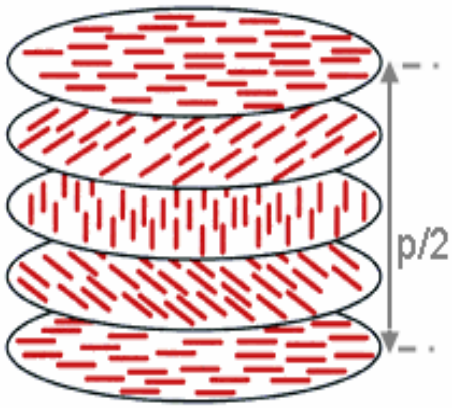

Fig. 5. Arrangement of molecules in the N* phase (the successive planes have been drawn for convenience, but do not have any specific physical meaning). Note that the structure repeats itself every half-pitch $P/2$, since in this phase directors at 0^0 and $\pm 180^0$ are equivalent.

In general, nematic phases present dielectric anisotropy. Therefore, they have different dielectric constants parallel ($\varepsilon_{\parallel}$) and perpendicular ($\varepsilon_{\perp}$) to their

molecular director. Thus, the twist of the LC molecules, results in a periodic modulation of the local dielectric constant of the LC. This periodic modulation causes Bragg reflection for certain optical modes. Such phenomenon can be exploited for several technological applications, inter-alia for lasing. In chapter 2 we will explain such phenomenon in more detail.

1.2.3 The SmA phase

These phases are more ordered than the nematic ones. In a SmA phase, molecules arrange themselves into parallel layers, which are more or less equally spaced. Within layers, molecules also present orientational order, as depicted in Fig. 2. In other words, there exists liquid order inside the layer, and molecules tend to align their directors perpendicularly to the layers.

The symmetry point group associated to this phase is ∞/mm and, therefore spontaneous polarization is forbidden.

1.2.4 The SmC phase

This mesophase also presents molecular arrangement in layers. Each layer is still a two-dimensional liquid, and orientational order is present within layers. Nevertheless the director is tilted with respect to the layer normal. The symmetry point group is $2/m$ and, therefore, no spontaneous polarization is allowed. This phase is sketched in Fig. 2.

1.2.5 The SmC phase*

If the SmC phase is formed by chiral molecules, chiral smectic C phase appears. In this mesophase molecules are also tilted within layers but the direction of tilt rotates from layer to layer around the layer normal giving rise to a helical configuration. See Fig. 6.

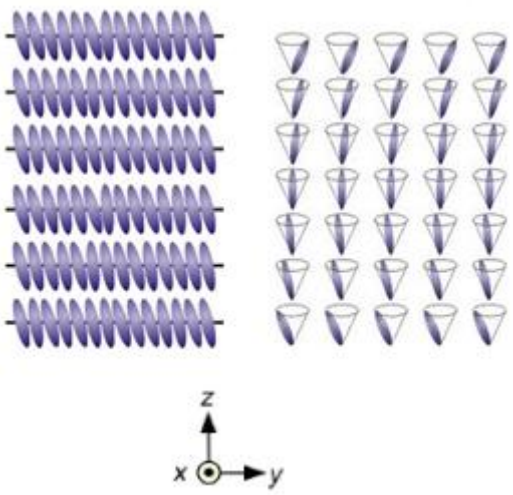

Fig. 6. Left: SmC mesophase. Right: SmC*mesophase.

At this point it is worth re-examining the elements of symmetry present in SmC mesophases:

-A plane of symmetry (z, y) in the reference frame of Fig. 6.

-A twofold axis (C_2) parallel to the x axis in Fig. 6.

-An inversion point.

Introduction of chirality suppresses the plane and the inversion centre. Thus, polarization appears along the C_2 axis. According to the remark made first by R.B Meyer[10], SmC*'s are ferroelectric; but because of the helical precession of the molecular director, a more rigorous denomination for this structure is helielectric. If an electric field parallel to the smectic layers is applied above a certain threshold the helix can be easily unwound and a true ferroelectric state is obtained. Thus, the phase suffers a transition to a ferroelectric state, where all the molecules are tilted in the same direction as in the SmC phase (see Fig. 7). Unfortunately, once that the field is removed the phase goes back to the ground state becoming again a helielectric state. However, if besides an electric field a properly treated glass surface is used, the unwinded ferroelectricity can be

stabilized[11]. Under such conditions, the SmC* becomes actually ferroelectric and is named surface stabilized ferroelectric liquid crystal.

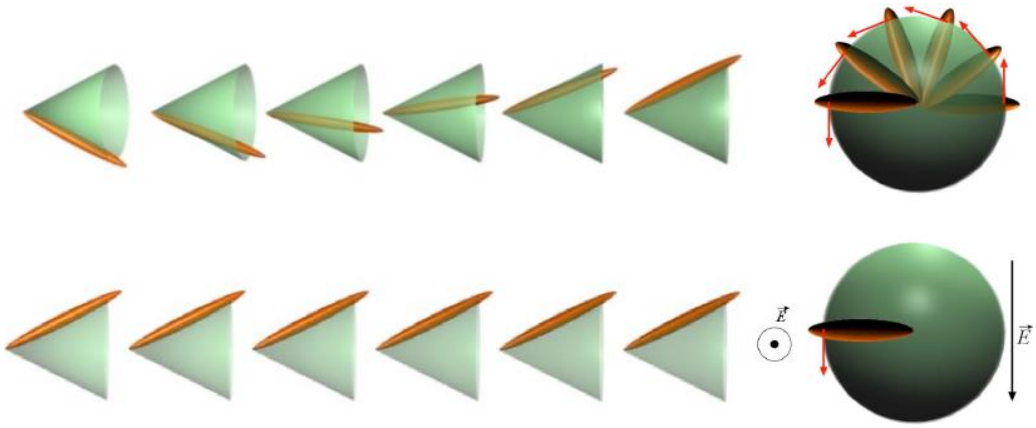

Fig. 7. Top: A half pitch of the helix in the SmC* phase: side view (left) and top view (right). The latter view shows the orientation of the spontaneous polarization in each layer (red arrows). Bottom: The helix unwound due to the reorientation of the dipoles by an electric field.

LCs can also give rise to other mesophases, as for example columnar ones, mesophases that exhibit positional order in two dimensions or modulated mesophases. Nevertheless a full description of LC phases is beyond the scope of this work since we will only deal with the N*, the SmC and the SmC* phases and some of its optical applications.

References

[1] T. Seideman, *Rep. Prog. Phys*. **53**, 659 (1990).

[2] D. Armitage and F. P. Prince, *J. Physique Coll.* **36**, 133 (1975).

[3] A. G. Petrov, "*The lyotropic state of matter*", Gordon & Breach (1999).

[4] P. G. de Gennes and J. Prost, "*The Physics of Liquid Crystals",* Clarendon Press (1993).

[5] G. Pelzl, I. Wirth and W. Weissflog, *Liquid crystals*, **28**, 969 (2001).

[6] T. Niori, T. Sekine, J. Watanabe, T. Furukawa and H. Takezoe, *J. Mater. Chem*. **6,** 1231 (1997).

[7] R. Amaranatha Reddy and C. Tschierske, *J. Mater. Chem.* **16**, 907 (2006).

[8] J. Martínez-Perdiguero, Y. Zhang, C. Walker, J. Etxebarria, C. L. Folcia, J. Ortega, M. J. O'Callaghan and U. Baumeister, *J. Mater. Chem.* **20**, 4905 (2010).

[9] F. Reinitzer, *Monatsh. Chem*. **9**, 421 (1888).

[10] R.B. Meyer, L. Liebert, L. Strzelecki and P. Keller, *J. Phys*. **36**, 69 (1975).

[11] N. A. Clark and S. T. Lagerwall, *Appl. Phys. Lett.* **36**, 899 (1980).

CHAPTER II

INTRODUCTION TO LIQUID CRYSTAL LASERS

2.1 Introduction

Most of the applications of liquid crystals are based on the response of the molecular director under the application of electric fields, which results in changes of their optical properties. Furthermore, most of these applications are based on the nematic phase. In this part of the dissertation we will focus on the cholesteric phase (CLC) and in its ability for light amplification. This phase is locally nematic and was first discovered in 1888[1].

The CLC mesophase poses different features. One of them is the existence of a helicoidal arrangement of the molecular director which gives rise to a photonic band gap for light. Photonic band gaps are known in different materials and can exist in one, two or three dimensions. This feature, depends on the number of directions in which periodicity exists. The existence of a band gap can be used for lasing. The first report of lasing in a CLC material dates from 1998 and was carried out by Kopp[2], later, lasing has been found in a wide variety of LC structures: blue phases I and II[3, 4, 5], cholesteric droplets[6, 7, 8] , polymerized cholesteric droplets[9] and paintable LC emulsions and films[8, 10]. Although other mesophases posses some features different from those characteristic of the cholesteric phase (for example, blue phase II can lase in three spatial directions[3]), the cholesteric is the most used phase for LC lasers because it is easily formed and it exhibit a broad temperature range.

Part of the recent interest in CLC lasers originates from different promising technological features. For example, due to the fact that the helical pitch can be easily modified by external stimuli, the lasing wavelength in CLC lasers can be tuned by means of several tuning mechanisms: temperature[11, 12], electric field[13, 14, 15], mechanical stress[16], or even by light irradiation[17, 18, 19]. That is not possible, in general, in solid-state lasers. Furthermore, other advantages are: low threshold lasing, high efficiency of energy conversion and ease of construction.

In the first part of this dissertation we will explain the fundaments of the CLC lasers. In addition, some of the concepts related to the peculiarities of the fluorescence spectra in CLCs will be experimentally demonstrated. In the next chapter about this subject we will study the CLC laser performance, paying special attention to the role of sample thickness. In the fourth chapter we will focus in the kinetic behavior of the laser emission and finally, in the last section, the problem of the degradation of CLC lasers will be studied.

2.2 The forbidden band in CLCs

Here, we are going to show the main theoretical fundaments to understand the origin of the photonic band gap in CLCs.

2.2.1 Bulky CLC

First, consider the case of a bulk CLC, i.e. an infinite thick sample. The director configuration is sketched in Fig. 1. We will call right handed helix, to one as that sketched in Fig. 1. This is a helix where the director describes clockwise rotation in the positive direction of z, for an observer looking against the $+z$ direction.

Fig. 1. CLC director configuration. x, y and z are the coordinate axes in the laboratory reference system.

In Fig. 1, in the system of reference x, y, z, the director $\mathbf{n}(z)$ varies in the space according to

$$n_x = \cos(\theta)\ , \tag{2.1}$$

$$n_y = \sin(\theta)\ , \tag{2.2}$$

and

$$n_z = 0\ , \tag{2.3}$$

where $\theta = q_0 z$ is the angle between the x axis and $\mathbf{n}(z)$ and $q_0 = \frac{2\pi}{P}$ where P is the helical pitch.

Let us consider an electromagnetic wave with angular frequency ω propagating in the $+z$ direction of Fig. 1. We can express this wave as

$$E_x(z,t) = E_x(z)\exp[-i\omega t] \tag{2.4}$$

and

$$E_y(z,t) = E_y(z)\exp[-i\omega t]\ , \tag{2.5}$$

where $E_{x,y}(z)$ are complex functions.

We assume that the medium has no free charges, is nonconductive, the relative dielectric tensor and the magnetic permittivity are independent of time and that this last one is a scalar. Under these assumptions from the Maxwell equations we can obtain the wave equation given by:

$$\nabla^2\mathbf{E} = \mu\,\overleftrightarrow{\varepsilon}\,\frac{\partial^2\mathbf{E}}{\partial t^2}\ , \tag{2.6}$$

where μ is the magnetic permeability and $\overleftrightarrow{\varepsilon}$ is the dielectric permittivity tensor.

Due to the fact that we have a rotating molecular director as we move along z, the corresponding dielectric tensor $\overleftrightarrow{\varepsilon}$ can be expressed as[20]

$$\overleftrightarrow{\varepsilon} = \frac{(\varepsilon_{\parallel} + \varepsilon_{\perp})}{2}\begin{pmatrix} 1 & 0 \\ 0 & 1 \end{pmatrix} + \frac{(\varepsilon_{\parallel} - \varepsilon_{\perp})}{2}\begin{pmatrix} \cos(2q_0 z) & \sin(2q_0 z) \\ \sin(2q_0 z) & -\cos(2q_0 z) \end{pmatrix}, \qquad (2.7)$$

where $\varepsilon_{\parallel}$ and $\varepsilon_{\perp}$ are the components of the dielectric permittivity parallel and perpendicular to the director.

Introducing Eqs. (2.4), (2.5) and (2.7) in Eq. (2.6) we arrive to

$$\frac{d^2E_x(z)}{dz^2} = \left(\frac{\omega}{c}\right)^2 \left[\frac{(\varepsilon_{\parallel} + \varepsilon_{\perp})}{2}E_x(z) + \frac{(\varepsilon_{\parallel} - \varepsilon_{\perp})}{2}\left[E_x(z)\cos(2q_0 z) + E_y(z)\sin(2q_0 z)\right]\right] \qquad (2.8)$$

and

$$\frac{d^2E_y(z)}{dz^2} = \left(\frac{\omega}{c}\right)^2 \left[\frac{(\varepsilon_{\parallel} + \varepsilon_{\perp})}{2}E_y(z) + \frac{(\varepsilon_{\parallel} - \varepsilon_{\perp})}{2}\left[E_x(z)\sin(2q_0 z) - E_y(z)\cos(2q_0 z)\right]\right], \qquad (2.9)$$

where c is the speed of light in vacuum.

Making the change of variable

$$E^{\pm} = E_x(z) \pm iE_y(z) \qquad (2.10)$$

and after some mathematical calculations, Eqs. (2.8) and (2.9) give rise to

$$-\frac{d^2E^+}{dz^2} = k_0^2E^+ + k_1^2E^-\exp[i2q_0 z] \qquad (2.11)$$

and

$$-\frac{d^2E^-}{dz^2} = k_0^2E^- + k_1^2E^+\exp[-i2q_0z]\,, \tag{2.12}$$

where

$$k_0^2 = \left(\frac{\omega}{c}\right)^2\frac{(\varepsilon_\parallel + \varepsilon_\perp)}{2} \tag{2.13}$$

and

$$k_1^2 = \left(\frac{\omega}{c}\right)^2\frac{(\varepsilon_\parallel - \varepsilon_\perp)}{2}\,. \tag{2.14}$$

From Eqs. (2.11) and (2.12) it is straightforward to obtain

$$E^+ = a\,\exp[i(l+q_0)z] \tag{2.15}$$

and

$$E^- = b\,\exp[i(l-q_0)z]\,, \tag{2.16}$$

where a and b are two constants determined by equations

$$[(l+q_0)^2 - k_0^2]a - k_1^2b = 0\,, \tag{2.17}$$

$$-k_1^2a + [(l-q_0)^2 - k_0^2]b = 0\,. \tag{2.18}$$

Eqs. (2.17) and (2.18) only have non-trivial solution if

$$[(-k_0^2 + l^2 + q_0^2)^2] - 4q_0^2l^2 - k_1^4 = 0\,. \tag{2.19}$$

As $\varepsilon_\parallel$ and $\varepsilon_\perp$have fixed values, for a given frequency ω Eq. (2.19) gives four possible roots of l. These values of l can be real or complex; in the case of real values the relation between l and ω is called the dispersion relation. Fig. 2 shows the typical form of the dispersion relation $\omega(l)$. From Fig. 2 it is clear that $\omega(l)$ has two branches. The interval separating the upper and the lower branches is the so-called band gap or forbidden band. In general, for each ω

there are four real values of l. Due to the parity of $\omega(l)$, these roots can be grouped into two pairs of values with the same magnitude and different sign. We will refer to them as $+l_1$, $-l_1$ and $+l_2$, $-l_2$. An exception is the forbidden gap where the relation (2.19) has only two real roots $l_1^{\pm}$. The other two roots are pure imaginary and therefore give rise to evanescent waves. From Eq. (2.19) it can be easily obtained that the forbidden band is determined by the relation:

$$\frac{2\pi c}{Pn_e} < \omega < \frac{2\pi c}{Pn_0}. \tag{2.20}$$

Each root $\pm l_i$ defines a normal mode of propagation determined by certain values of a and b. These quantities determine the state of polarization of the normal modes and can be obtained by solving Eqs. (2.17) and (2.18).

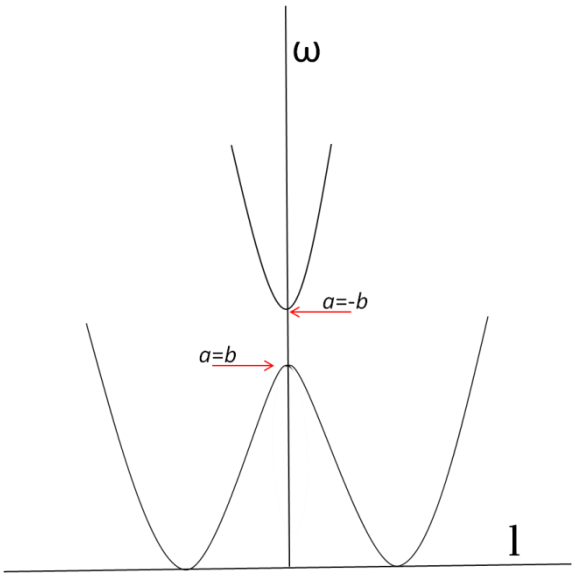

Fig. 2. Dispersion relation for propagating normal modes in a CLC. The frequency interval between $a = b$ and $a = -b$ is the photonic bandgap.

By introducing a and b in Eqs. (2.15), (2.16) and using Eqs. (2.4), (2.5) and (2.10) we can find the form of the normal modes of propagation along the z direction in the x, y, z system of reference. Typically, these normal modes are elliptically polarized and are given by:

$$E_{ix}^{\pm}(z,t) = \frac{\left(a\exp\left[i\left(l_i^{\pm}+q_0\right)z\right]+b\exp\left[i\left(l_i^{\pm}-q_0\right)z\right]\right)}{2}\exp[-i\omega t] \qquad (2.21)$$

and

$$E_{iy}^{\pm}(z,t) = i\frac{\left(b\exp\left[i\left(l_i^{\pm}-q_0\right)z\right]-a\exp\left[i\left(l_i^{\pm}+q_0\right)z\right]\right)}{2}\exp[-i\omega t]\,. \qquad (2.22)$$

As we are concerned with the photonic properties of CLCs we will focus the attention on the band gap region and the surrounding region.

In the edge of the band gap $l = 0$. At this point, using the dispersion relation (2.19) and Eqs. (2.17) and (2.18) we find two possible cases: $a = b$ and $a = -b$.

Let us first focus in the case $a = b$. From Eqs. (2.17) and (2.18) it is straightforward that

$$\omega = \frac{2\pi c}{P\sqrt{\varepsilon_{\parallel}}} = \frac{2\pi c}{Pn_e}\,. \qquad (2.23)$$

Therefore the situation corresponds to the low frequency band gap edge.

So

$$E_x(z,t) = a\exp[-i\omega t]\cos(\theta) \qquad (2.24)$$

and

$$E_y(z,t) = a\exp[-i\omega t]\sin(\theta). \qquad (2.25)$$

Then, for the low frequency edge (and thus for the long wavelength edge), the normal mode is linearly polarized and oscillates in every point along the direction of the CLC director. Notice that since we are in the band gap edges, it is immediate from Fig. 2 that $\frac{d\omega}{dl} = 0$, i.e. the group velocity is null. So at the low frequency edge we have a standing wave that is linearly polarized along the molecular director at every z.

Let us now focus on the high frequency edge. In that case $l = 0$ and $a = -b$. From Eqs. (2.17) and (2.18) it is immediate that

$$\omega = \frac{2\pi c}{P\sqrt{\varepsilon_\perp}} = \frac{2\pi c}{Pn_0}\,, \tag{2.26}$$

$$E_x(\,z,t\,) = -ib\exp[-i\omega t]\sin(\theta) \tag{2.27}$$

and

$$E_y(\,z,t\,) = ib\exp[-i\omega t]\cos(\theta)\,. \tag{2.28}$$

Then, for the high frequency edge (and thus for the short wavelength edge), the normal mode is a standing wave linearly polarized that oscillates at every point perpendicularly to the director. Both standing modes are in the origin of lasing in CLCs.

Apart from the band gap edges modes, with $l = 0$, we can also analyze how are the other normal modes in the region of interest, i.e. for wavelengths comparable to the helical pitch. An important parameter characterizing the polarization state of a wave is the ellipticity ρ. In our case is given by:

$$\rho = \frac{-2lq_0}{k_0^2 - l^2 - q_0^2 - k_1^2}\,. \tag{2.29}$$

Taking into account that for small birefringence

$$k_1 \ll k_0\,. \tag{2.30}$$

We obtain from Eq. (2.19)

$$l_1^{\pm} = \pm(k_0 + q_0) \tag{2.31}$$

and

$$l_2^{\pm} = \pm(k_0 - q_0)\,. \tag{2.32}$$

By substituting the corresponding l_i values in Eq (2.29) we obtain $\rho \approx \pm 1$ which corresponds to right and left circularly polarized modes respectively ($a = 0$ or $b = 0$). The corresponding electric fields, in the x, y, z system of reference, can be straightforwardly obtained from Eqs. (2.21) and (2.22).

Summarizing the previous results. When we have a CLC of infinite thickness, along its helix there are four possible optical normal modes of propagation. Two of them travelling forwards and two backwards. In the vicinity, but outside, of the forbidden band, these modes are circularly polarized. Two of them right handed and two left handed. Within the forbidden band there are only two normal modes. These normal modes are circularly polarized with opposite handedness to that of the helix, one travelling forward and the other backwards. Interestingly, at each band edge only exist three normal modes: two of them circularly polarized with a handedness opposite to that of the helix. And a standing wave linearly polarized. In the low frequency edge, oscillates following the director at every z and in the high frequency edge oscillates perpendicularly to the director.

2.2.2 Finite CLC sample

Now, let's focus our attention on the more realistic case of a finite CLC confined between two substrates (see Fig. 3). To study this case we are going to follow the procedure used by other authors[21, 22].

Consider the case of an incident wave perpendicularly to the sample, i.e. in the helix axis direction. We are interested in knowing the normal modes of transmission. These normal modes are defined as those whose state of polarization remains unaltered after having been transmitted through the sample.

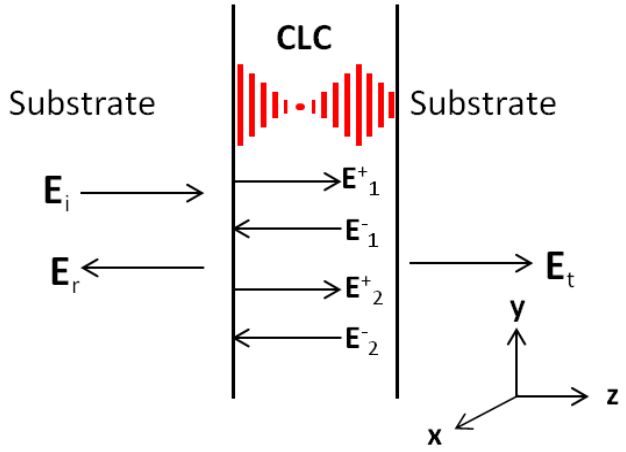

Fig. 3. Sample configuration in the laboratory reference system x, y, z. i ,r and t denote the incident, reflected, and transmitted waves respectively. $\mathbf{E}_i^{\pm}$ are the normal modes of a bulky cholesteric system, shown in Eqs. (2.21) and (2.22).

The mathematical solution of this problem is more difficult than that of a bulky CLC because in a finite sample we have to take into account the boundary conditions of the CLC with the substrate.

For calculating the transmitted and reflected electric fields through the finite CLC sample, we have to apply the required conditions at each boundary, i.e. the tangential components for $\mathbf{E}$ and $\mathbf{H}$[23] must be continuous. For a sample of thickness d these conditions are:

$$\mathbf{E}_i(0) + \mathbf{E}_r(0) = \mathbf{E}_1^+(0) + \mathbf{E}_1^-(0) + \mathbf{E}_2^+(0) + \mathbf{E}_2^-(0)\,, \tag{2.33}$$

$$\mathbf{H}_i(0) + \mathbf{H}_r(0) = \mathbf{H}_1^+(0) + \mathbf{H}_1^-(0) + \mathbf{H}_2^+(0) + \mathbf{H}_2^-(0)\,, \tag{2.34}$$

$$\mathbf{E}_t(d) = \mathbf{E}_1^+(d) + \mathbf{E}_1^-(d) + \mathbf{E}_2^+(d) + \mathbf{E}_2^-(d) \tag{2.35}$$

and

$$\mathbf{H}_t(d) = \mathbf{H}_1^+(d) + \mathbf{H}_1^-(d) + \mathbf{H}_2^+(d) + \mathbf{H}_2^-(d)\,. \tag{2.36}$$

Notice that the normal modes described by the Eqs. (2.21) and (2.22) must be used as the fields inside the sample. From Eqs. (2.33-2.36) the transmitted and

reflected electric fields can be obtained from a given incident electric field by means of a 4x4 transference matrix:

$$\begin{bmatrix} E_{ix} \\ E_{iy} \\ E_{rx} \\ E_{ry} \end{bmatrix} = \overleftrightarrow{A} \begin{bmatrix} E_{tx} \\ E_{ty} \\ 0 \\ 0 \end{bmatrix}, \tag{2.37}$$

where $\overleftrightarrow{A}$ is a 4x4 transference matrix that depends on the sample parameters. The detailed procedure of the calculation of $\overleftrightarrow{A}$ can be found in Refs. 21 and 22.

A normal mode is a wave that does not change its polarization but changes its field amplitude and phase. Therefore there exist a relationship between the incident and transmitted electric fields given by:

$$\begin{pmatrix} E_{tx} \\ E_{ty} \end{pmatrix} = t \begin{pmatrix} E_{ix} \\ E_{iy} \end{pmatrix}, \tag{2.38}$$

where t is a complex number. By introducing this relation into Eq. (2.37) the transmission normal modes can be obtained. In general four normal modes can be obtained for a given angular frequency of the incident electromagnetic wave. They are nearly circularly polarized, two of them right handed and two of them left handed. For each polarization there is a mode travelling in the $+z$ direction and another mode travelling in the $-z$ direction. The transmission modes with a handedness opposite to that of the CLC helix can always propagate through the sample as in the case of a bulky CLC. Furthermore, their transmittance T is an oscillating function that deviates slightly from 1 independently of the wavelength (see Fig. 4 (a)). We will refer to them as non forbidden modes.

On the other hand, for the transmission modes with the same handedness as that of the CLC helix, there is a region of the spectrum where propagation is forbidden, this is why we will call them forbidden modes. Fig. 4 (b) represents the transmittance T for these modes: Outside the forbidden region T describes

small oscillations around 1. Near the band edges, these oscillations become sharp and show a local maximum at both band edges. Within the forbidden band T is almost 0. An experimental example of this behavior is shown in Fig. 5. An analytic expression of these normal modes and their eigenvalues can be found in the literature, for example, in Refs. 21 and 22.

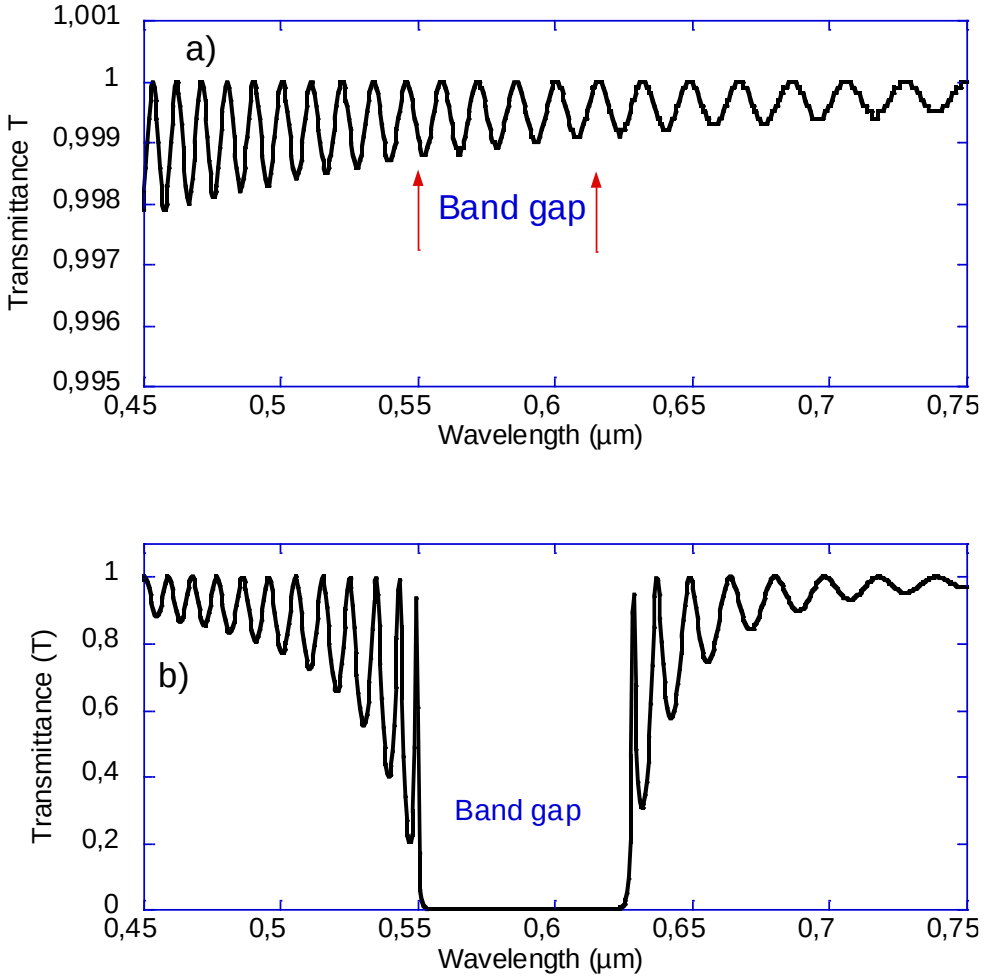

Fig. 4. (a) Transmittance of the non forbidden, and (b) forbidden modes in a typical CLC sample.

The transmitted and reflected intensities can be obtained by considering that $R + T = 1$. When unpolarized light impinges on the sample, the transmitted intensity can be easily calculated by means of the decomposition of the light into two circularly polarized waves of opposite handedness. As a consequence,

the selective reflection always occurs for the component of the same handedness as the helix. Due to this fact many CLCs show bright colors. We present in Fig. 6 two typical cases of selective reflection in the optical spectrum.

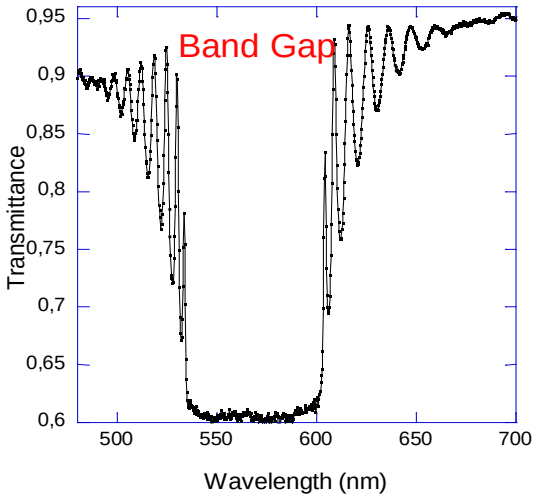

Fig. 5. Experimental measurement of the transmittance spectrum for unpolarized light of a typical CLC.

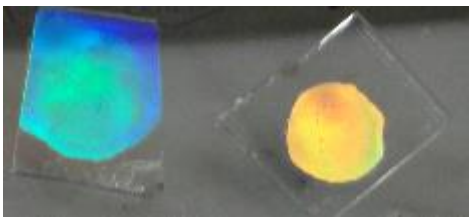

Fig. 6. Selective reflections in a typical CLC at the blue and orange regions of the optical spectrum.

The position of the band gap and thus the color due to selective reflection depends, as in the case of a bulky CLC, on the material parameters and on the helix pitch. Such dependence can be written as

$$P = \frac{2\lambda_B}{n_o + n_e}, \tag{2.39}$$

where λ_B is the wavelength corresponding to the middle of the band gap and, n_o and n_e are the ordinary and extraordinary refractive indexes perpendicular and parallel to the molecular director respectively.

2.3 The density of optical states (DOS)

The origins of lasing also requires the understanding of the concept of density of optical states (DOS). In this dissertation we will define the DOS as:

$$DOS = \frac{dk(\omega)}{d\omega}\,, \tag{2.40}$$

which is the inverse of the group velocity[24] and can be defined as the number of wave vectors k per unit of angular frequency ω. Evidently modes with a small group velocity (quasi-standing waves) are of interest in order to obtain lasing in a cavity. These modes in its turn present the highest values of DOS.

In infinite and homogeneous optical media such relation is analytically accessible by solving Maxwell equations and, calculating the DOS is a simple problem. Also, in bulky CLCs the dispersion relation is analytically accessible and the DOS can be obtained by simple differentiation of Eq. (2.19). Nevertheless, calculating the DOS in a finite CLC is not a trivial task.

For calculating the DOS in a finite sample it is necessary to know the dispersion relation $k(\omega)$. The general procedure is reported by Dowling and Bedickson in Ref. 25. The method consists in obtaining the transmission coefficients of the optical eigenmodes of the sample that in general are complex quantities given by:

$$t = x + iy\,, \tag{2.41}$$

The corresponding phase to each mode for a sample of thickness L is

$$\varphi = kL\,. \tag{2.42}$$

This quantity can be obtained from the transmission coefficient by means of the following expression:

$$\tan\varphi = \frac{y(\omega)}{x(\omega)}\,. \tag{2.43}$$

Then, by simple differentiation of Eq. (2.43) with respect to ω, the DOS can be obtained and is given by:

$$DOS = \left(\frac{1}{L}\right)\frac{\left(y'x - x'y\right)}{(x^2 + y^2)}\,, \tag{2.44}$$

where primes indicate derivatives with respect to ω.

2.3.1 DOS in a Fabry Perot Cavity

Since our main purpose is to use CLCs as optical resonators, it is illustrative to get a first insight into a classical optical resonator as a Fabry-Perot (F-P) cavity. A F-P cavity is a simple device which confines light by two reflecting mirrors (see Fig. 7).

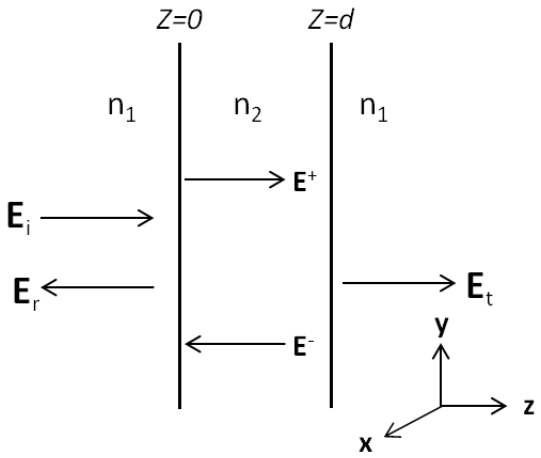

Fig. 7. Configuration of fields in a Fabry Perot cavity. n_i denote the indexes of refraction.

Applying the boundary conditions for **E** and **H** at $z = 0$ and at $z = d$:

$$\begin{pmatrix} E_i \\ E_r \end{pmatrix} = \frac{1}{2n_1}\begin{pmatrix} n_1 + n_2 & n_1 - n_2 \\ n_1 - n_2 & n_1 + n_2 \end{pmatrix}\begin{pmatrix} E^+ \\ E^- \end{pmatrix} \tag{2.45}$$

and

$$\begin{pmatrix} E^+ \\ E^- \end{pmatrix} = \frac{1}{2n_2}\begin{pmatrix} (n_1 + n_2)\exp[-ik_2 d] & 0 \\ 0 & (n_1 - n_2)\exp[ik_2 d] \end{pmatrix}\begin{pmatrix} E_t \\ E_t \end{pmatrix}, \tag{2.46}$$

where $k_2 = \frac{n_2 \omega}{c}$.

Combining Eqs. (2.45) and (2.46) and operating one arrives to:

$$E_t = \frac{(1 - r^2)}{\sqrt{1 - 2r^2\cos(x) + r^4}}\exp[i(k_2 d + \psi)]E_i \ , \tag{2.47}$$

where $x = 2k_2 d$, $r = \frac{n_2 - n_1}{n_2 + n_1}$ and $tan(\psi) = \frac{r^2 \sin(x)}{1 - r^2\cos(x)}$.

Then, using Eqs. (2.47) and (2.44), the DOS of a F-P cavity can be written as

$$DOS = \frac{n_2}{c}\frac{(1 - r^4)}{(1 + r^4 - 2r^2\cos(x))} \ . \tag{2.48}$$

The maximum DOS occurs when $\cos(x) = 1$:

$$DOS_M = \frac{n_2}{c}\left(\frac{1 + r^2}{1 - r^2}\right)$$

In Fig. 8 we show the typical shape for the transmittance T and the DOS as a function of x. For the simulation, we have considered that the reflectance of the mirrors is of 0.9. Notice that peaks and valleys of the DOS coincide with those of T. Modes with low DOS are almost completely reflected since their transmittance is very small. On the other hand, modes with high DOS can be transmitted through the cavity since their reflectance is small. This behavior can

also be interpreted by means of the group velocity. High DOS modes correspond low V_g. In such cases, quasi-standing waves are formed in the cavity. Photons corresponding to those modes 'stay' long time inside the cavity. Such modes dissipate energy slowly out of the cavity so a high electromagnetic energy can be stored in such modes.

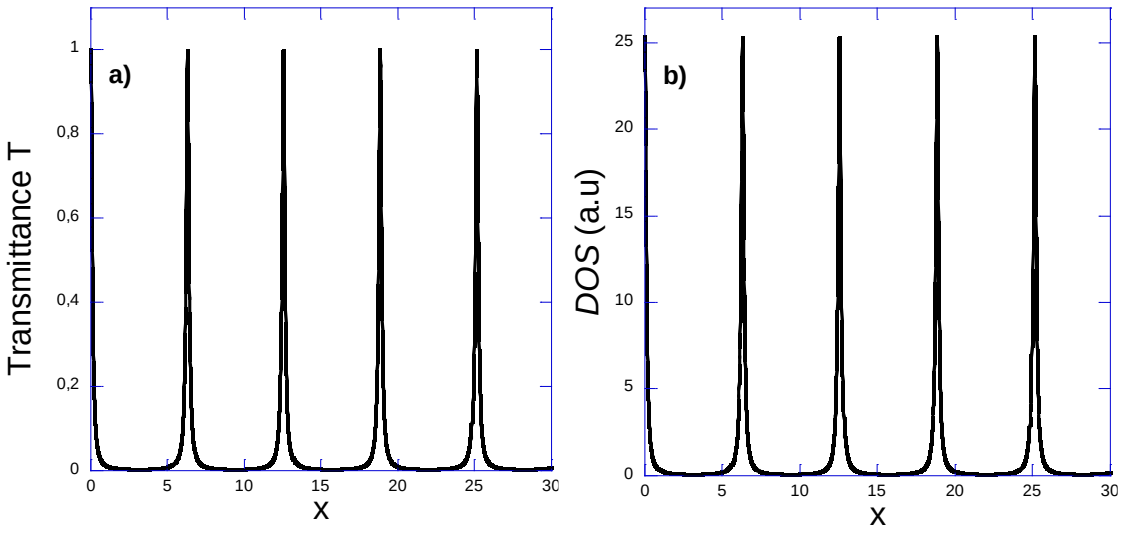

Fig. 8. (a) Transmittance and (b) DOS in a Fabry Perot Cavity.

2.3.2 DOS in an infinite CLC

Turning back to the case of a bulky CLC the DOS can be calculated by simple differentiation of Eq. (2.19). Focusing our attention on the vicinity of the stop band, the DOS of the non-forbidden modes is almost constant independently of the wavelength. On the other hand, the DOS of the forbidden modes diverges at the band edges (see Fig. 9). This divergence can also be understood looking at the dispersion curve in Fig 2. As can be seen, at the edges of the photonic band gap the group velocity becomes 0; thus the DOS of such modes diverges.

This behavior has important implications. For example, since the DOS is infinite at the band edges, an infinite quantity of electromagnetic energy can be stored

within the photonic cavity with the wavelength corresponding to that of the band edges.

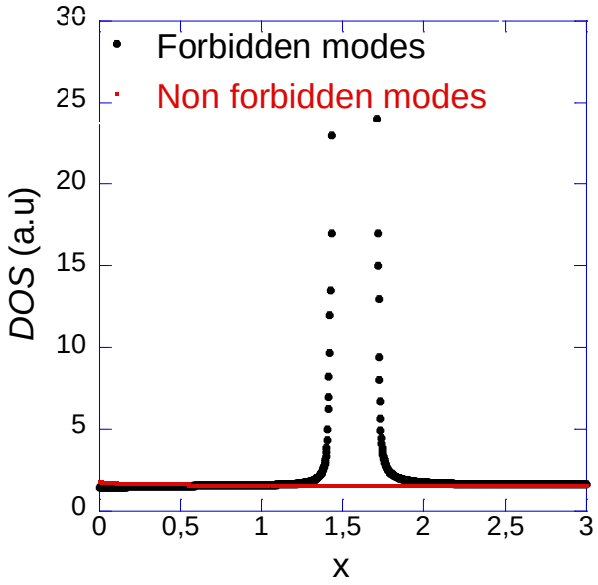

Fig. 9. DOS of the two normal modes in an infinite CLC. $x = \frac{\lambda}{P}$.

2.3.3 DOS in a finite CLC

In the case of a finite CLC sample, the dispersion relation is quite complex and the differentiation results in a rather complicated function. However, DOS can also be obtained analytically[26].

Applying Eq. (2.44) it can be shown that the representation of DOS *vs.* wavelength of the forbidden modes presents peaks and valleys outside the stop band, such peaks coincide with those of the transmittance (see Fig. 10 (a) and (b)). The amplitude of the oscillations increases near the band edges and has two characteristic maxima located at both edges of the forbidden band. Inside the forbidden band the DOS is close to 0.

Similarly to the case of the Fabry-Perot cavity, the enhanced DOS at the band edges is useful for storing electromagnetic energy of the corresponding

wavelengths. In other words, electromagnetic modes corresponding to the band edge wavelength are quasi-standing waves since their group velocity is small.

On the other hand, the thicker the sample, the higher the DOS peaks at the band edges and the smaller the transmission inside the photonic band gap. Evidently DOS tends to infinite at the edges for the limit of an infinite sample as previously explained.

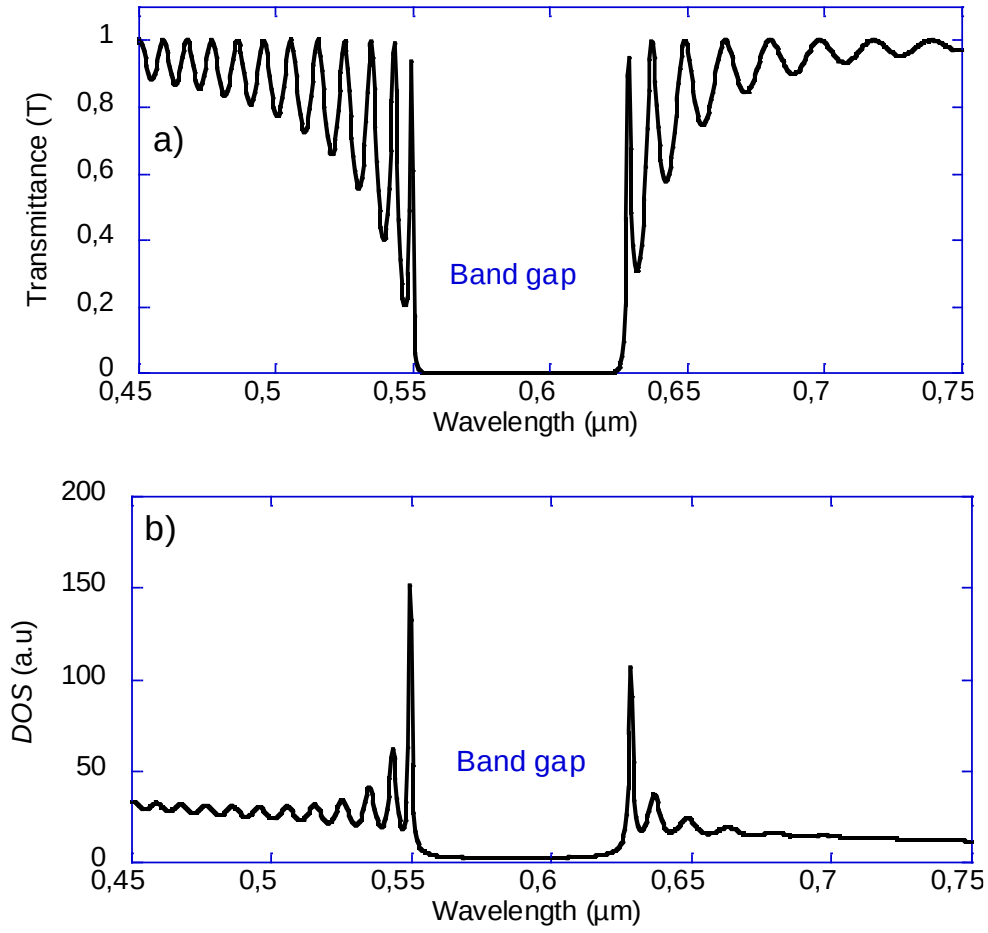

Fig. 10. (a) Transmittance and (b) DOS of the forbidden modes in a typical CLC sample. P = 600 nm, L =12 μm.

For the non-forbidden modes the DOS is almost constant over the entire wavelength range and describes small oscillations (Fig. 11 (b)). The transmittance of these modes is near 1 (see Fig. 11 (a)) and describes small oscillations around 1. Again, peaks and valleys in the transmittance coincide

with those of the DOS. However, oscillations in T and DOS are so small that are not appreciable in Fig. 11.

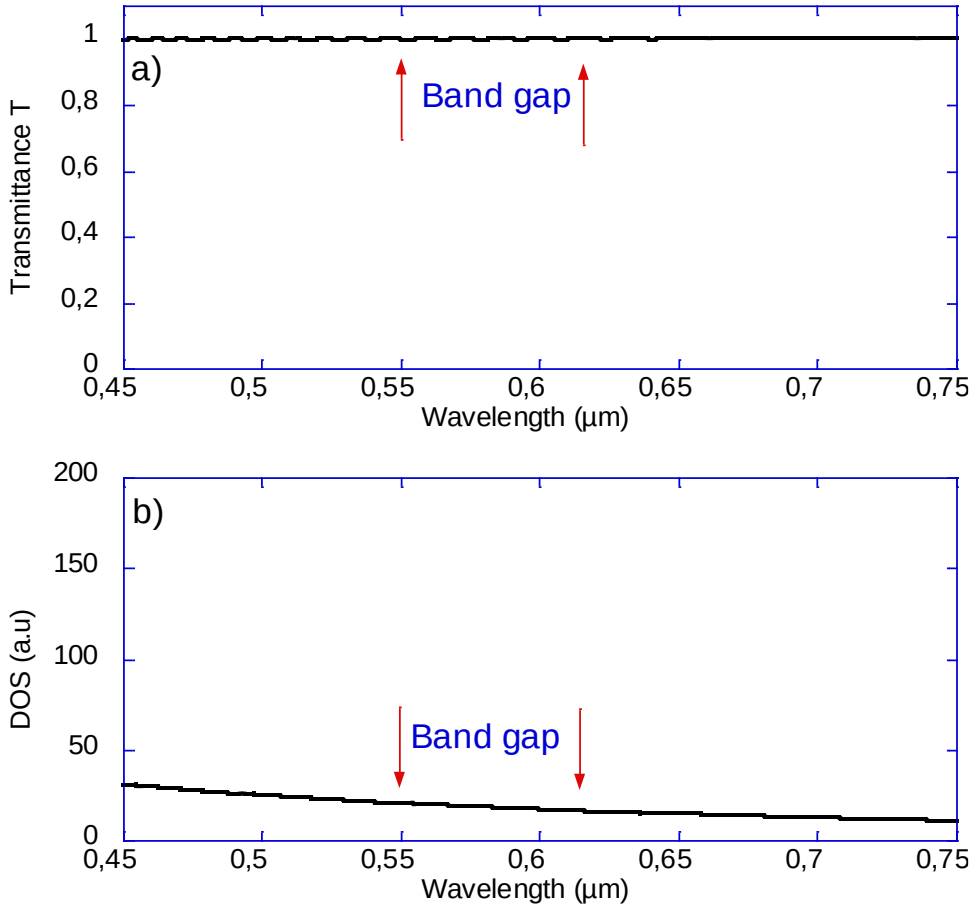

Fig. 11. (a) Transmittance and (b) DOS of the non-forbidden modes in a typical CLC sample. P = 600 nm, L =12 μm.

2.4 Fermi's golden rule

Fermi´s golden rule relates the emission rate $W(\omega)$ of an oscillating dipole with the DOS. If $\hat{\boldsymbol{\mu}}$ is the dipole moment operator, $\mathbf{r}$ is the position of the oscillating dipole and $\mathbf{E}$ is the electric field of the normal modes, then

$$W(\omega) = C\ DOS|\hat{\boldsymbol{\mu}} \cdot \mathbf{E}(\omega, \mathbf{r})|\,, \tag{2.49}$$

where C is a constant.

From Eq. (2.49) it is clear that the emission rate and, therefore, the intensity of emission of the dipole are proportional to the DOS. So the emission spectrum of a light source embedded in a CLC cavity will be proportional to the DOS of the cavity. As a consequence a light source will emit more light at the edge modes of the forbidden band due to the enhancement of DOS.

2.5 Liquid crystal lasers

The photonic properties of a CLC cavity can be exploited for laser emission. Due to the peculiar DOS spectrum of the forbidden modes, and because of Fermi's golden rule, the emission spectrum of a light source embedded within the cavity is completely altered with respect to its emission spectrum in an isotropic solvent. Such source will emit much more photons at the edge modes. An alternative interpretation in terms of electromagnetic waves can be made taking into account that the DOS is the inverse of the group velocity. Therefore light emission at the edges of the photonic band gap will form quasi-standing waves at these modes.

For achieving band edge laser emission, is necessary to introduce a light harvester in the CLC. This light harvester is usually a dye dispersed in the mixture, as for example DCM. In other cases a LC can be synthesized with a light harvester as part of its structure. In this case no dye dispersed in the CLC mixture is needed. For example, many liquid crystals, due to their chemical composition, absorb and emit in the ultraviolet. This is why ultraviolet lasing can be achieved without any dye[27].

Another requisite is fundamental. The emission spectrum of the light harvester must overlap the photonic band. Furthermore, in order to minimize the lasing threshold the maximum of the non-altered emission spectrum must be matched

with the lasing band edge[26]. An example of this situation is shown in Fig. 12. Most of the dyes, that are commonly used, present a high linear dichroism. Therefore, the efficiency of the exciting and stimulated emitting modes highly depends on their state of polarization respect to the dye orientation. Both band edges are not equivalent, in this respect, and the one at which lasing occurs depends on the order parameter of the dye molecules respect to the director of the host CLC. If dye molecules lie along the director, lasing occurs at the long wavelength edge and if they lie perpendicularly to the director, lasing happens at the short wavelength edge. In an infinite CLC this can be understood since at the long wavelength edge mode the polarization state of the electric field is locally parallel to the molecular director whereas at the short wavelength one is perpendicular.

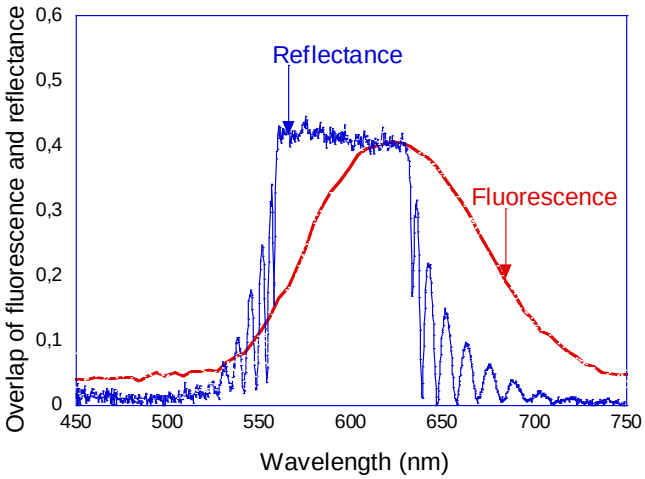

Fig. 12. Overlap of the non-altered fluorescence spectrum of DCM with the band gap of a CLC sample. Notice that the maximum of fluorescence almost matches the long edge wavelength of the forbidden band.

When the emitting molecules are excited, some of them will spontaneously emit a photon in any direction and with many possible optical modes. Light emitted in the direction of the helix can be decomposed in forbidden and non forbidden modes. Non forbidden photons, independently of their wavelength, will

'escape' from the cavity due to their relatively low DOS and thus high V_g. On the other hand, forbidden photons are not allowed so their emission is suppressed. When the forbidden modes match the wavelengths of the band edges, they have a greatly enhanced DOS. This, results in a high emission rate at these modes. In other words, since their V_g is very small, these modes form quasi-standing waves, and photons are 'kept' within the cavity, dissipating energy slowly out of the cavity. These photons produce stimulated emission among excited dyes. Due to the properties of stimulated emission[24], the new emitted photons will have the same optical properties and they will stimulate in its turn other dyes. This is an amplification effect. The quasi-stationary wave leaks energy outside the cavity at a very low rate. The emerging radiation is laser light that, as previously seen, is circularly polarized with the same handedness as that of the helix. Calculations suggest[21] that the suppressed radiation within the photonic band is transferred to the band edges.

In order to maintain the population of excited dyes in the laser cavity a pumping source is required. In CLC lasers, usually a pulsed Nd:YAG laser is used. It is important to choose a pumping wavelength near the absorption maximum of the dye. If the wavelength of the pump overlaps the forbidden band, part of the pumping intensity will be reflected. In those cases it is desirable to use circularly polarized light with opposite handedness to that of the helix. The minimum pumping energy required for laser generation is called the threshold energy. One of the objectives in CLC lasers is lowering the threshold as much as possible. A challenging target in this respect is to diminish the threshold energy as much as to allow using simple and economic pumping sources.

2.5.1 An example of CLC lasing

At this point we are going to present experimental evidence of the above mentioned concepts. With this aim we prepared a CLC mixture of the classical nematic LC E7 (Synthon) with a chiral twisting agent (compound 2 in reference 28) and the classical dye 4-(dicyanomethylene)-2-methyl-6-(p-dimethylaminostyryl)-4H-pyran (DCM), (Aldrich) in proportions 95:5:1 (wt.-%) respectively. The mixture was introduced into a commercial glass cell of 9.9 μm of thickness. The glasses were treated with parallel-rubbed polyimide layers. By using a polarized optical microscope we observed a high quality alignment in the CLC phase (Cano's geometry).

The pump source was a Nd:YAG laser operating at the second-harmonic frequency (wavelength 532 nm). Pulses of 14 ns and with a repetition rate of 5 Hz were used. The pump source was focused on the sample using a lens of 20 cm of focal length; the spot size at the sample was of 40 μm of diameter. The incident light was circularly polarized with a handedness opposed to that of the CLC sample. The angle of incidence of the pump beam was 45^0. The emitted signal, around the sample normal, was collected using a lens of 5 cm of diameter and of 5cm of focal length. This signal was focused on an optical-fiber spectrometer with a resolution (FWHM) of $\Delta\lambda$ =0.5 nm. Fig. 13 shows the experimental setup used in this experiment.

Measurements were made at the temperature of 22 ^{0}C. First, we measured the reflectance spectrum of the sample. The reflection band appeared between 559 nm and 634 nm (see Fig. 14), thus the helical pitch was of 367 nm. The calculation is straightforward considering Eq. (2.39) and the typical indexes of refraction of E7 at room temperature.

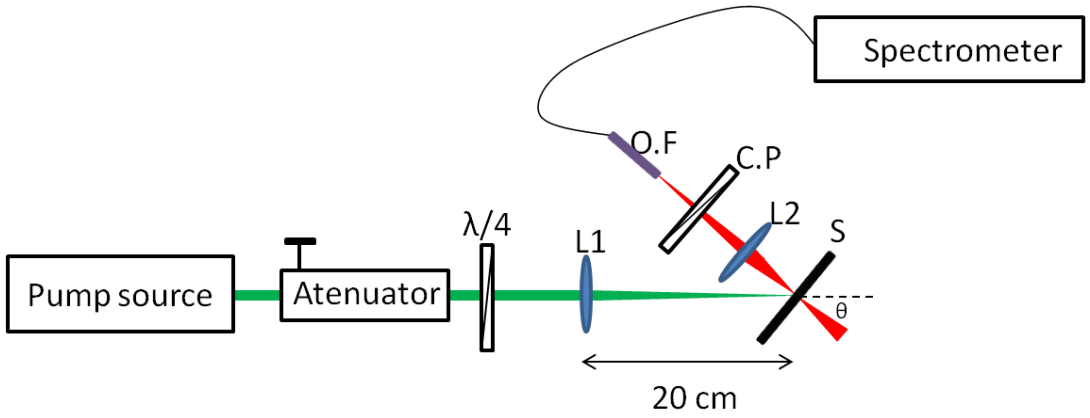

Fig. 13. Experimental setup. L1 and L2 are lenses 1 and 2 respectively, S is the sample, θ is the angle of incidence, and O.F is the abbreviation for optical fiber.

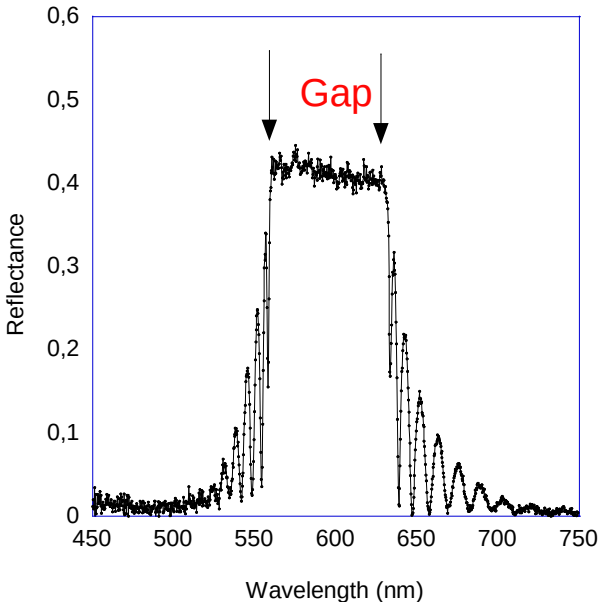

Fig. 14. Reflectance spectrum of the CLC sample. Unpolarized light was used in this measurement.

In order to measure the isotropic emission spectrum of DCM, we dissolved a small quantity of dye in ethanol and simply approached the optical fiber of the spectrometer to the container in order to detect the emitted light. The obtained spectrum is represented in Fig. 15.

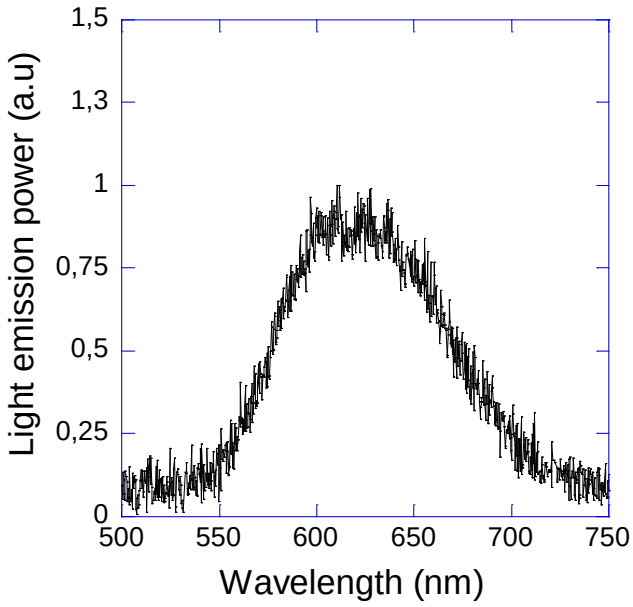

Fig. 15. Normalized fluorescence spectrum of the DCM dissolved in ethanol.

Then, we measured the fluorescence spectrum of the dye dissolved in the photonic structure using the experimental setup schematized in Fig. 13. The results are shown in Fig. 16.

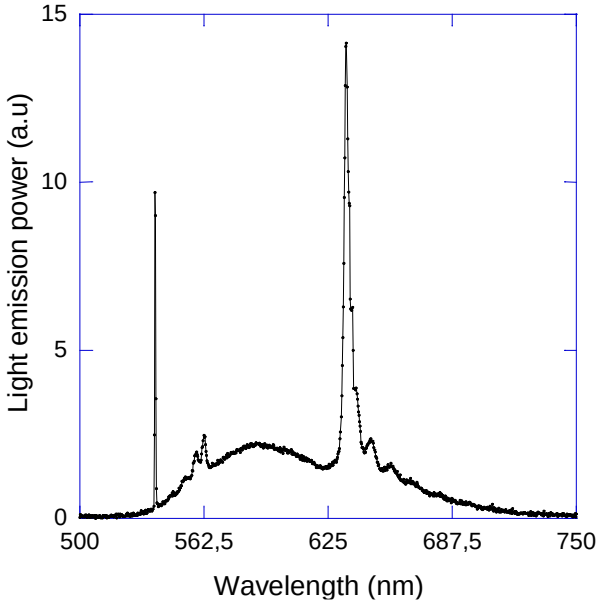

Fig. 16. Fluorescence spectrum of the DCM dissolved in the CLC host. Unpolarized light was measured. The line at 532 nm corresponds to the pumping laser.

Finally, we analyzed the fluorescence polarization by using circular polarizers corresponding to both hands (see Fig. 13). The obtained spectra are shown in Fig. 17.

Looking at Figs. 14-16 we can see that, since the reflection band overlaps the emission spectrum of the dye, its fluorescence is greatly altered. Furthermore, in Fig. 17 (b) we can see that such alteration barely affects the shape of LCP light spectrum (it is almost the same as the one shown in Fig. 15). The small peak observed at 634 nm in the LCP spectrum can be attributed to two facts. On the one hand, the most important reason is that the circular polarizer is not perfectly circular so a small part of the RCP component leaks through the LCP polarizer. On the other hand, and less important, strictly speaking, the normal modes are no perfectly circularly polarized but slightly elliptically polarized[21]. As a consequence, a small part of the intense RCP component at the band edge of the spectrum (Fig. 17(a)) leaks through the LCP polarizer.

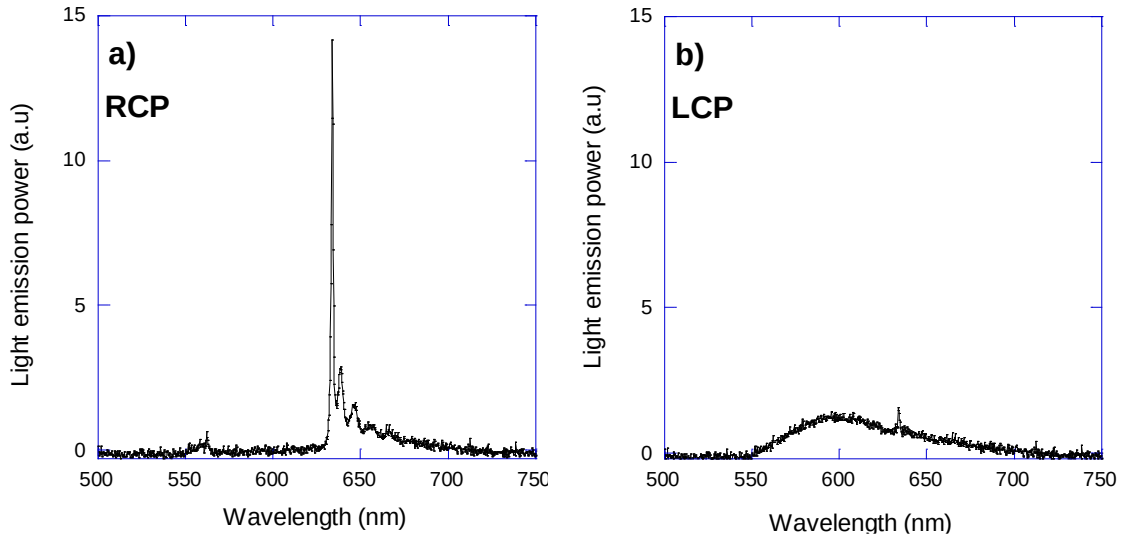

Fig. 17. Fluorescence spectra of the right circularly polarized mode RCP (a) and, left circularly polarized mode LCP (b) of the dye within the CLC host.

The RCP component of the spectrum is drastically modified as expected (Fig. 17 (a)). It is suppressed within the band gap and enhanced at the edges. In our

case, the enhancement is greater at the long wavelength edge of the stop band. This fact is related to the order parameter of the dye molecules respect to the local director of the CLC host; for DCM in E7, the dye aligns preferentially parallel to the director, and thus, is parallel to the electric field of the mode corresponding to the long wavelength band edge. This is the optimum electric field configuration to excite the dye. On the contrary, for short wavelength mode the electric field is perpendicular to the molecular director and thus the configuration is the worst.

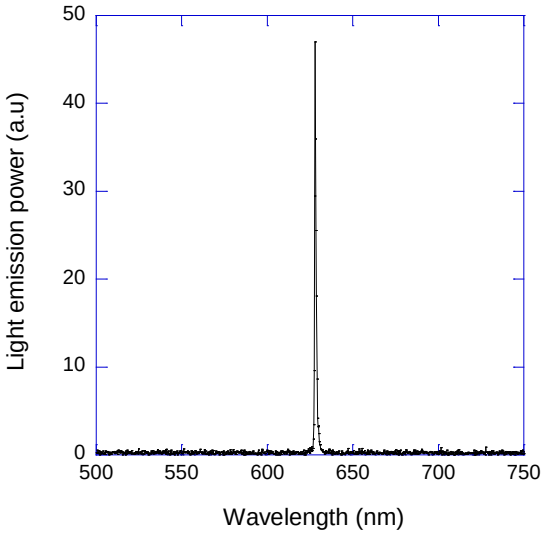

Fig. 18. Laser radiation spectrum. The peak position corresponds to 634 nm.

Laser was observed just at the long wavelength edge of the stop band (634 nm) when the pump power was increased above a threshold (see Fig. 18). The polarization of the laser light was RCP i.e., with the same handedness as that of the CLC material. This demonstrates that the feedback for lasing action is provided by the reflection of RCP light in the cavity.

2.6 Radiation dwelling time

In conventional lasers based on Fabry-Perot cavities, the rate at which radiation decreases inside the cavity is the inverse of a characteristic time known as the dwelling time τ_c. This decrease in radiation is due to photon leakage because of the use of semitransparent mirrors, absorption losses in the medium and diffraction on the edges of mirrors. The dwelling time is a very important parameter to characterize the efficiency of a laser.

In CLC lasers, at the edges of the forbidden band, the optical density of states presents a very pronounced maximum. This fact implies a small group velocity and thus a long dwelling time for photons inside the CLC cavity. In these lasers the decrease in radiation intensity inside the cavity is due to photon leakage through the substrates of the sample and to losses because of radiation absorption and/or scattering in the CLC. Taking into account these losses due to absorption and scattering, the radiation dwelling time has been approximately calculated as[29, 30]

$$\frac{1}{\tau_c} = \frac{c}{n}\left(\beta + \frac{4P^2}{\alpha^2 L^3}\right), \tag{2.50}$$

where L is the is the length of the resonant cavity, β is a coefficient of distributed losses, which accounts for the absorption and scattering in the CLC sample, $n = \sqrt{\frac{n_o^2+n_e^2}{2}}$ is the mean refractive index, $\alpha = \frac{(n_o^2-n_e^2)}{(n_o^2+n_e^2)}$ is the optical anisotropy parameter and P is the pitch.

2.7 Rate equations for laser generation

Here we are going to explain with some detail the model of kinetic equations for laser generation proposed by Shytkov and Palto [JETP, **118**, 822 (2014)][30].

These equations are based on a laser scheme of three electronic levels: the ground singlet level S_0, first excited singlet level S_1 and ground triplet level T_0. This is sketched in Fig. 19.

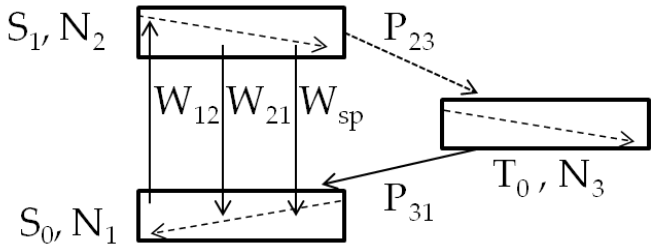

Fig. 19. Diagram of energy levels in a dye molecule. Solid arrows indicate radiative transitions; dashed arrows indicate thermal processes within an energy band, and the doted arrow indicates intercombination transitions from an excited singlet to a triplet level.

In Fig. 19:

-w_{12} is the probability of induced transition from S_0 to S_1 upon absorption of a pumping photon. $w_{12} = \frac{\sigma_a I_a}{h\nu_a}$,[31] where ν_a is the frequency of the absorbed pumping photons, h is the Plank constant, σ_a is the cross section of absorption, and I_a is the intensity of the pumping radiation.

-w_{21} is the probability of induced transition from S_1 to S_0 upon the emission of a photon. $w_{21} = \frac{\sigma_e I_e}{h\nu_e}$,[31] where ν_e is the frequency of the emitted photons, σ_e is the cross section of induced emission, and I_e is the intensity of emitted light.

-$w_{sp} = \frac{1}{\tau_{21}}$ is the probability of spontaneous transition from S_1 to S_0 upon emission of a photon. τ_{21} is the fluorescence lifetime of level 2.

-P_{23} is the probability of spontaneous transition from S_1 to T_0.

-P_{31} is the probability of spontaneous transition from T_0 to S_0.

-N_i is the population per unit volume of level i.

In Ref. 30 it is assumed that $\sigma_a = \sigma_e = \sigma$. However, we will not make such assumption here. The pump beam propagates along the CLC helix axis, this is the z direction. See an scheme of lasing in Fig. 20.

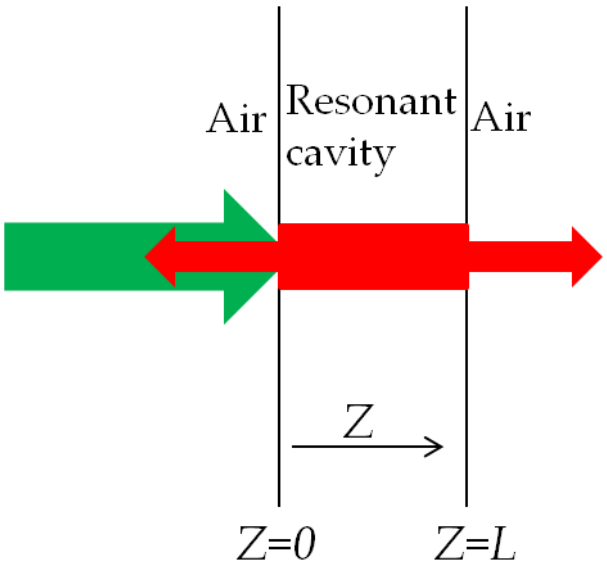

Fig. 20. Scheme of lasing in a CLC sample. The pumping beam is represented by the green arrow, it is along the z direction and enters at $z = 0$. The generated radiation is represented by the red arrows and it escapes from both sample boundaries.

Considering spatial inhomogeneity of the pump only in the pumping direction and, thus in the populations of the different levels, the system of kinetic equations is:

$$\frac{\partial N_2(z,t)}{\partial t} = \frac{\sigma_a I_a(z,t)}{h\nu_a} N_1(z,t) - \frac{\sigma_e I_e(t)}{h\nu_e} N_2(z,t) - \frac{N_2(z,t)}{\tau_{21}} - P_{23} N_2(z,t)\,,$$

$$\frac{\partial N_3(z,t)}{\partial t} = P_{23} N_2(z,t) - P_{31} N_3(z,t)\,,$$

$$\frac{dI_e(t)}{dt} = \frac{ch\nu_e S}{nV}\int_0^L \left(\frac{\sigma_e I_e(t)}{h\nu_e} N_2(z,t) + k\frac{N_2(z,t)}{\tau_{21}}\right) dz - \frac{I_e(t)}{\tau_c}, \qquad (2.51)$$

$$N_1(z,t) + N_2(z,t) + N_3(z,t) = N.$$

where c is the speed of light in vacuum, V is the volume of the pumped region, S is the section of the pumping beam, L is the CLC thickness, and N is the total number of dye molecules per unit volume. τ_c, is the radiation dwelling time of an emitted photon in the CLC layer. Finally, the k coefficient is the fraction of spontaneous radiation at the laser frequency that travels along the helix axis; it can be considered as the seed for lasing.

Note that the partial derivatives in the two first equations of system (2.51) denote spatial inhomogeneity of the populations in the z direction. The first of Eqs. (2.51) describes the evolution of the population of the excited singlet level. This level is the responsible of lasing. In such evolution, there is a competition between induced absorption, induced and spontaneous emission to the ground state, and the transition of the dye molecules from the excited singlet to the ground triplet. Transitions to the ground triplet are non radiative. The accumulation of excited molecules in this level is taken into account by the second of Eqs. (2.51). This accumulation is due to a competition between P_{23} and P_{31}. In the third equation, the term inside the integral, describes the number of photons generated inside the cavity per unit of volume and unit of time, traveling along the helix direction. These photons are due to induced and spontaneous emission. The last term of this equation takes into account the decrease of radiation within the cavity due to the photons dwelling time inside the cavity, τ_c that is given by Eq. (2.50). Finally, the last of Eqs. (2.51) describes the law of conservation of dye molecules.

We will now operate with Eqs. (2.51) in order to have them in a simpler form.

Let's define the average population of level i along the sample thickness as:

$$n_i(t) = \left(\int_0^L N_i(z,t)dz \right) \frac{1}{L}. \tag{2.52}$$

Combining Eqs. (2.51) and (2.52) and integrating respect to z, one arrives to:

$$\frac{dn_2(t)}{dt} = \frac{\sigma_a N}{h\nu_a L}\left[\int_0^L I_a(z,t)dz - \frac{1}{N}\int_0^L I_a(z,t)\, N_2(z,t)dz - \frac{1}{N}\int_0^L I_a(z,t)\, N_3(z,t)dz \right] - n_2(t)\left(\frac{\sigma_e I_e(t)}{h\nu_e} + \frac{1}{\tau_{21}} + P_{23} \right),$$

$$\frac{dn_3(t)}{dt} = P_{23}n_2(t) - P_{31}n_3(t)\,, \tag{2.53}$$

$$\frac{dI_e(t)}{dt} = \frac{c}{n}\left(\sigma_e I_e(t) + k\frac{h\nu_e}{\tau_{21}} \right) n_2(t) - \frac{I_e(t)}{\tau_c},$$

$$N = n_1(t) + n_2(t) + n_3(t)\,.$$

The pumping intensity as the beam travels through the sample is given by:

$$I_a(z,t) = I_{a0}(t)\exp[-\sigma_a n_1(t)z]. \tag{2.54}$$

Note that Eq. (2.54) is an approximation since, strictly speaking, $N_1(z,t)$ should be used instead of $n_1(t)$.

Now, let's define the average population of level i in the interval $(0,z)$ as

$$\bar{n}_i(z,t) = \left(\int_0^z N_i(x,t)dz \right) \frac{1}{z}\,, \tag{2.55}$$

which coincides with the averages $n_i(t)$ in the limit of $z = L$. Assuming the approximation $\bar{n}_i(z,t)z = n_i(t)L/2$, which is the average of this product at the

boundaries of the sample, and introducing Eqs. (2.54) and (2.55) in system (2.53) we arrive to

$$\frac{dn_2(t)}{dt} = -\left(\frac{\sigma_e P_e(t)}{h\nu_e S} + \frac{1}{\tau_{21}} + \frac{\sigma_a P_{a0}(1+\exp[-\sigma_a n_1(t)L])}{2h\nu_a S} + P_{23}\right) n_2(t)$$
$$- \frac{\sigma_a P_{a0}(1+\exp[-\sigma_a n_1(t)L])}{2h\nu_a S}\ n_3(t) + \frac{NP_{a0}(1-\exp[-\sigma_a n_1(t)L])}{h\nu_a SLn_1(t)},$$

$$\frac{dn_3(t)}{dt} = P_{23}n_2(t) - P_{31}n_3(t)\,, \tag{2.56}$$

$$\frac{dP_e(t)}{dt} = \frac{c}{n}\left(\sigma_e P_e(t) + k\frac{h\nu_e S}{\tau_{21}}\right) n_2(t) - \frac{P_e(t)}{\tau_c},$$

where ligth intensity has been replaced by power, i.e. $P_e = I_e S$.

So, under a standard laser scheme for physics of ordinary laser, Shytkov et al. arrive to a system of kinetic equations for laser generation in CLCs. The only peculiarity of the CLC cavity is introduced through τ_c.

[1] F. Reinitzer, *Monatsh. Chem*. **9**, 421 (1888).

[2] V. I. Kopp, Z. Q. Zang and A. Z. Genack, *Opt. Lett*. **23**, 1707 (1998).

[3] W. Cao, A. Muñoz, P. Palffy-Muhoray and B. Taheri, *Nat. Mater*. **1**, 111 (2002).

[4] S. Yokoyama, S. Mashiko, H. Kikuchi, K. Uchida and T. Nagamura, *Adv. Mater.* **18,** 48 (2006).

[5] S. M. Morris, A. D. Ford, C. Gillespie, M. N. Pivnenko, O. Hadeler and H. J. Coles, *J. SID*, **14**, 565 (2006).

[6] M. Humar and I. Musevic, *Opt. Express,* **18**, 26995 (2010).

[7] P. J. W. Hands, D. J. Gardiner, S. M. Morris, C. Mowatt, T. D. Wilkinson and H. J. Coles, *Appl. Phys. Lett.* **98**, 141102 (2011).

[8] D. J. Gardiner, S. M. Morris, P. J. W. Hands, C. Mowatt, R. Rutledge, T. D. Wilkinson and H. J. Coles, *Opt. Express*, **19**, 2432 (2011).

[9] G. Cipparrone, A. Mazzulla, A. Pane, R. J. Hernandez and R. Bartolino, *Adv. Mater*. **23**, 5773 (2011).

[10] P. J. W. Hands, D. J. Gardiner, S. M. Morris, C. Mowatt, T. D. Wilkinson and H. J. Coles, *Appl. Phys. Lett.* **98**, 141102 (2011).

[11] K. Funamoto, M. Ozaki and K. Yoshino, *Jpn. J. Appl. Phys.* **42**, L1523 (2003).

[12] Y. Huang, Y. Zhou, C. Doyle and S. T. Wu, *Opt. Express*, **14**, 1236 (2006).

[13] H. Yu, B. Y. Tang, J. Li and L. Li, *Opt. Express*, **13**, 7243 (2005).

[14] B. Park, M. Kim, S. W. Kim, W. Jang, H. Takezoe, Y. Kim, E. H. Choi, Y. H. Seo, G. S. Cho and S. O. Kang, *Adv. Mater.* **21**, 771 (2009).

[15] J. Schmidtke, G. Jünnemann, S. Keuker-Baumann and H. S. Kitzerow, *Appl. Phys. Lett.* **101**, 051117 (2012).

[16] H. Finkelmann, S. T. Kim, A. Muñoz, P. Palffy-Muhoray, and B. Taheri, *Adv. Mater.* **13**, 1069 (2001).

[17] L. J. Chen, J. D. Lin, and C. R. Lee, *J. Mater. Chem. C*, **2**, 4388 (2014).

[18] T. V. Mykytiuk, I. P. Ilchishin, O. V. Yaroshchuk, R. M. Kravchuk, Y. Li, and Q. Li, *Opt. Lett.* **39**, 6490 (2014).

[19] G. S. Chilaya, *Crystallogr. Rep.* **51**, S108 (2006).

[20] P. G. de Gennes and J. Prost, "*The Physics of Liquid Crystals"*, Clarendon Press (1993).

[21] W. Cao, *"Fluorescence and lasing in liquid crystalline bandgap materials"*, PhD Thesis, Kent State University, (2005).

[22] V. A. Belyakov and S. V. Semenov, *J. Exp. Theor. Phys*. **109**, 687 (2009).

[23] A. Yariv, *"Optical Waves in Crystals"*, Wiley (1984).

[24] Frank L. Pedrotti, S. J. Leno S. Pedrotti, *"Introduction to optics"*, Prentice Hall (1993).

[25] J. M. Bendickson, J. P. Dowling, and M. Scalora, *Phys. Rev. E*, **53**, 4107 (1996).

[26] L. M. Blinov, *JETP Lett.* **90**, 166 (2009).

[27] A. Muñoz, P. Palffy-Muhoray and B. Taheri, *Opt. Lett.* **26**, 804 (2001).

[28] J. Lub, W. P. M. Nijssen, R. T. Wegh, I. De Francisco, M. P. Ezquerro and B. Malo, *Liq. Cryst.* **32**, 1031 (2005).

[29] V. A. Belyakov and S. V. Semenov, *J. Exp. Theor. Phys*. **109**, 687 (2009).

[30] N. M. Shtykov and S. P. Palto, *J. Exp. Theor. Phys.* **118**, 822 (2014).

[31] A. Yariv, *"Quantum electronics"*, Wiley (1989).

CHAPTER III

CHOLESTERIC LIQUID CRYSTAL LASERS PERFORMANCE: ROLE OF THE SAMPLE THICKNESS

3.1 Introduction

One of the main targets in the development of CLC lasers is the improvement of their efficiency. A good performance of the laser devices would allow us to use simpler and more economic pumping sources. In addition, one of the main drawbacks of these devices is their relatively quick deterioration and, therefore, the utilization of low-power excitation sources would result in more durable CLC lasers, which is an essential requirement for commercial applications.

The energy conversion in lasers is characterized by the so-called slope efficiency η, defined as the slope of the curve obtained by representing the laser output power versus the input pumping power. Another important parameter characterizing laser performance is the threshold energy E_{th} that is the minimum pumping energy per pulse required for laser generation. Both quantities are connected to each other and depend on the features of the laser cavity. In the case of CLC lasers, the main parameters to be considered are the thickness of the sample, the local birefringence of the material, the dye concentration, the coefficient of distributed losses for the laser radiation, and the cross sections of absorption and induced emission of the pumping and laser lights, respectively. A detailed knowledge of the dependences of E_{th} and η on the cavity parameters as, for example the thickness, will allow optimizing the fabrication of CLC lasers. Fig. 1 shows an example of laser emission energy *vs.* the pumping energy in a CLC laser. Below threshold (blue dots), the energy emission is null since there is no lasing but fluorescence. Above threshold (red dots) a linear dependence is observed whose slope is the slope efficiency η. The point at which this line intercepts the abscissa can be used for determining the lasing threshold energy.

The aim of this chapter is to characterize the performance of CLC lasers paying especial attention to the role of the sample thickness. The main target is to

deduce reliable expressions for E_{th} and η as a function of the most important physical parameters of the CLC layer in order to provide us with an important tool to design CLC lasers efficiently. To start we will make a brief description of the state of art in this respect.

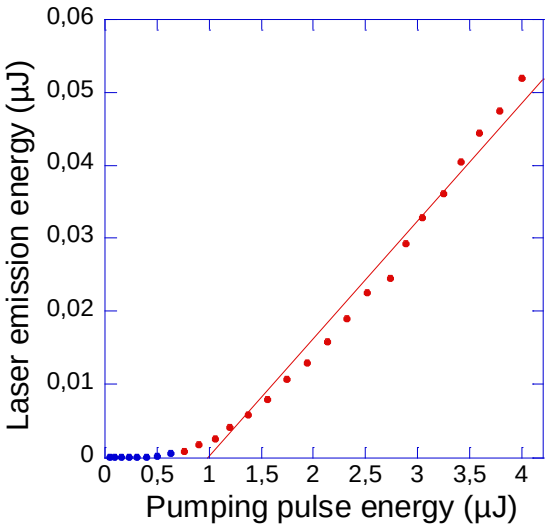

Fig. 1. Laser emission as a function of the incident pump energy for a sample thickness of 14 μm.

The general belief when studying the performance of lasers is that the optimum efficiency is achieved when the threshold power is minimum. In order to better understand previous approaches to deduce expressions for E_{th}, we will explain some related concepts and we will apply them to the case of standard lasers based on Fabry-Perot (F-P) cavities.

Let's first consider a scheme of two atomic energy levels 1 and 2 with populations N_1 and N_2 respectively, being level 2 the high energy level. The probability distribution of the transition frequency between both levels is described by a Lorentzian function[1]:

$$g(\nu) = \frac{(2/\pi\Delta\nu)}{1 + [2(\nu - \nu_0)/\Delta\nu]^2}\,, \tag{3.1}$$

where ν_0 is the frequency center of transition and $\Delta\nu$ is the FWHM of the transition spectrum.

When atoms are excited to level 2, they can stay at this level for a certain period of time before decaying to level 1. If the rate at which atoms are excited to level 2 is higher than the decay rate, it occurs that $N_2 > N_1$. This is the so-called population inversion, which is one of the basic requisites for lasing.

If a monochromatic wave with frequency ν and intensity I travels through our collection of atoms, it can be absorbed or amplified. After travelling a small distance dz, the intensity change of the wave will be:

$$dI = \left[N_2 B_{21} g(\nu)\frac{I}{c} - N_1 B_{12} g(\nu)\frac{I}{c}\right] dz\,, \tag{3.2}$$

where B_{21} is the Einstein coefficient for stimulated emission and B_{12} is the Einstein coefficient for stimulated absorption. Using the relation[1]

$$B_{21} = B_{12} = c^3 \frac{A_{21}}{8\pi h\nu^3}\,, \tag{3.3}$$

where A_{21} is the Einstein coefficient for spontaneous emission. We arrive to

$$\frac{dI}{dz} = (N_2 - N_1)\frac{c^2 A_{21}}{8\pi\nu^2} g(\nu) I\,. \tag{3.4}$$

Integrating:

$$I = I(0)\exp[\gamma(\nu)z]\,, \tag{3.5}$$

where

$$\gamma(\nu) = (N_2 - N_1)\frac{c^2 A_{21}}{8\pi\nu^2} g(\nu) \tag{3.6}$$

is the optical gain constant. Notice that under population inversion $\gamma(\nu) > 0$ and the wave is amplified while propagating through the medium. On the other hand, if $N_2 < N_1$ $\gamma(\nu)$ is negative and the wave is absorbed.

The so-called amplitude condition for laser generation implies that the optical gain of the laser medium must compensate the losses suffered by laser light in one round trip in the laser cavity. In classical lasers, as those based in F-P cavities, losses can be localized (caused by the optical mirrors) or distributed. Distributed losses are due to photon absorption and/or scattering while travelling through the resonator and are very difficult to control. A sketch of a photon propagating inside a F-P cavity is shown in Fig. 2, where β represents the distributed losses and r_1, r_2 are the reflectance of the mirrors. At the starting point the field is E_n. After a round trip the field is E_{n+1}. So, at the threshold, in order to compensate all losses, it must occur that

$$\frac{E_{n+1}}{E_n} = 1 = r_1 r_2 \exp[L(\gamma - \beta)] \exp[i2kL] \tag{3.7}$$

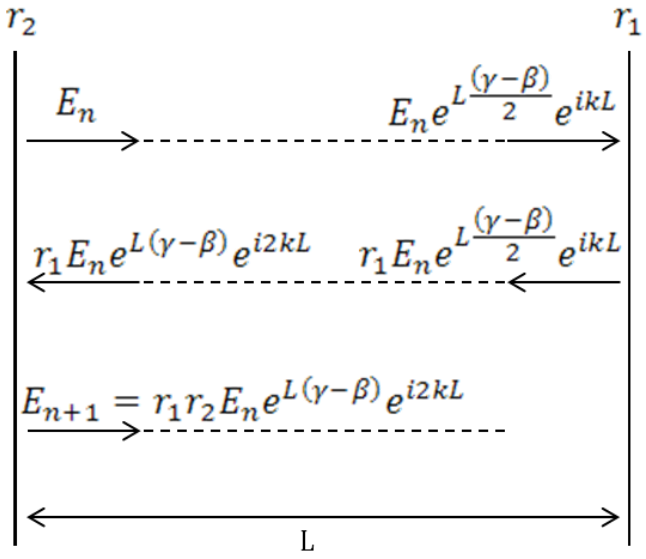

Fig. 2. Field configurations of a wave inside a F-P cavity with amplifying medium. γ is the optical gain constant (see Eq. (3.6)), β is the coefficient of distributed losses, L is the cavity length and r_1 and r_2 are the reflection coefficients of the mirrors.

Eq. (3.7) implies that

$$\exp[i2kL] = 1 \tag{3.8}$$

and

$$r_1 r_2 \exp[L(\gamma - \beta)] = 1\,. \tag{3.9}$$

Eq. (3.8) is the phase condition. The cavity modes can be derived from Eq. (3.8). The so-called amplitude condition is derived from Eq. (3.9):

$$\gamma_{th} = \beta - \frac{1}{L}\ln(r_1 r_2)\,, \tag{3.10}$$

where γ_{th} is the threshold gain coefficient, β is the coefficient of distributed losses, L is the cavity length and $\ln(r_1 r_2)$ takes into account the localized cavity losses due to the reflectance of the mirrors (r_i).

In classic F-P resonators, considering that $r_1 = r_2 \approx r$ and at the maximum of the optical density of states we obtain, from expression (2.48), $r^2 = \frac{\rho_M - 1}{\rho_M + 1}$, being $\rho_M = \frac{c}{n} DOS_M$. Thus, it results

$$\gamma_{th}^{F-P} = \beta - \frac{1}{L}\ln(r^2) = \beta - \frac{1}{L}\ln\left(\frac{\rho_M - 1}{\rho_M + 1}\right) \approx \beta + \frac{2}{\rho_M L}\,, \tag{3.11}$$

where the subscript M denotes that we are at a peak of the density of optical states.

Usually, under laser generation conditions $N_2 \gg N_1$. In addition the population inversion must be maintained. Therefore, assuming that below the threshold the main mechanism for de-excitation is the spontaneous emission, the condition for lasing is given by:

$$\frac{dN_2}{dt} = K_{pump} - A_{21} N_2 = 0\,, \tag{3.12}$$

where K_{pump} is the rate at which dye molecules are being excited to level 2. Evidently $E_{th} \propto K_{pump}$. From Eqs (3.6) and (3.12) we can deduce the following dependence for E_{th}[1]:

$$E_{th}^{F-P} = A\gamma_{th}^{F-P} L = A\left(\beta + \frac{2}{\rho_M L}\right) L = A\beta L + \frac{2A}{\rho_M}, \tag{3.13}$$

where A is a constant.

As an expression for γ_{th} is not available for CLC lasers, some authors[2, 3, 4] have adopted expression (3.13), making an analogy with the case of F-P cavities. In this case, ρ_M must be replaced by the expression corresponding to the CLC layer. For L values corresponding to practical situations $\rho_M \approx L^2\alpha^2/2P^2$ [3]. Therefore:

$$E_{th}^{CLC} = A\beta L + \frac{2A'}{L^2\alpha^2}. \tag{3.14}$$

Based on this idea, Blinov[3] carried out quantitative predictions for E_{th} that were compared with the previous experimental results[2, 5, 6, 7] reaching a reasonable agreement in some cases. However, the extrapolation of the threshold gain for a F-P cavity to CLC lasers is not fully justified and a precise expression connecting E_{th} to L is not available up to now.

An alternative to this approach was presented by Shtykov *et al*[8]. The theory is based on the rate equations for the populations of the excited states and laser generation. The model is a simplified version of the system of equations shown in section (2.7) of the introduction. In this case, the key parameter to account for the characteristics of the CLC laser is the radiation lifetime for the lasing photons in the CLC sample[9], τ_c. For solving such equations, the authors assumed a stationary case. Furthermore, they assumed a system of two levels, neglecting the transitions to the triplet level of the dye. Using such

approximations, the dependence of E_{th} on the sample thickness was found to be similar to those of the above-mentioned approaches. The results were also compared with the measurements carried out by other authors[2, 4], and the optimum sample thickness to minimize E_{th} was reasonably calculated. However, the quantitative predictions for E_{th} were poor and only the order of magnitude was correctly calculated. This is not surprising taking into account the roughness of the considered approximations. For example, the assumption of an almost constant pumping source, implies stationary solutions. However, this is not the case in real experiments. In addition, as it will be shown in this chapter, the triplet level has fundamental implications in CLC lasers and cannot be ignored. Inter alia, it prevents laser emission by using continuous pumping (CW).

Concerning the slope efficiency, it was assumed in all the referred works that the maximum η is achieved when the threshold intensity is minimum. This idea is based in the assumption that $\eta \propto 1/E_{th}$. However, this point has never been confirmed in CLC lasers neither theoretically nor experimentally. In this regard, Morris et al.[7] proposed an analytical expression for $\eta(L)$. However, the approach was based on the assumption that the dye is a two level system, thus disregarding transitions to the triplet level. Likewise, $\eta(L)$ was obtained from the stationary solution of the rate equations, assuming a homogeneous pumping. All these approximations are very unrealistic to obtain accurate results since, as we have already said, the triplet level cannot be disregarded due to its important implications in these devices.

From the experimental point of view, only a few reports can be found in the literature with measurements of both E_{th} and η versus L[4, 7]. In all these works, the results for η are fitted to a phenomenological expression obtained under the assumption $\eta \propto 1/E_{th}$.

Very recently, a new work by Shtykov and Palto[10] has been published. It makes use of improved kinetic rate equations for the excited states and laser generation (see section (2.7) of the introduction). This new model improves their previous one[8] by considering transitions to the triplet level of the dye and taking into account the time dependence of the pump. In the study, predictions for E_{th} are compared with other works in the literature[2, 4]. The experimental values are in general higher than those calculated. However, the authors reach an excellent agreement with experimental results carried out by themselves in CLC samples with Coumarin 6 dye. Nevertheless, no analytical expression is given for E_{th}.

In this chapter, we will focus on the analysis of the CLC laser performance as a function of the sample thickness. The study will be carried out both from experimental and theoretical points of view. For the theoretical approach we will use the model proposed by Shtykov and Palto[10] incorporating an additional step to calculate the emitted power outside the cavity. By means of such model, the profiles of $E_{th}(L)$ and $\eta(L)$ will be obtained numerically. Finally, approximate analytical expressions for $E_{th}(L)$ and $\eta(L)$ will be deduced and compared with the numerical and experimental results.

3.2 Experimental procedure and results

The materials used to built the CLC laser were obtained by mixing the classical nematic LC E7 (Synthon) with a right handed chiral twisting agent (compound 2 in reference[11]) and the dye 4-(dicyanomethylene)-2-methyl-6-(p-dimethylaminostyryl)-4H-pyran (DCM), (Aldrich) in the proportions 93.9:5.2:0.9 (wt.-%) respectively.

A wedge cell with angle of $2x10^{-3}$ rad was made with thickness range from 3.7 to 53.7 μm. The inner surfaces of the sample were pre-treated with parallel-rubbed polyimide. The material was introduced in the cell in the isotropic phase and subsequently cooled down to the CLC mesophase to obtain the Cano geometry.

Then, we checked the photonic properties of the material following the same procedure as that of section (2.5.1) of this dissertation. We obtained similar results, i.e., lasing consisted on circularly polarized light with the same handedness as that of the CLC helix (right handed). However, in this case the band gap was shifted because of the difference in the concentration of the chiral dopant. The reflection band appeared between 533 nm and 605 nm; thus the helical pitch was of 350 nm (see Eq. (2.39)). Lasing occurred at the long edge (see Fig. 3).

The pump source was a Nd:YAG laser operating at the second-harmonic frequency (wavelength 532 nm). Pulses of 14 ns and with a repetition rate of 5 Hz were used. The pump source was focused on the sample using a lens of 20 cm of focal length; this resulted in a spot size of 40 μm of diameter at the sample. We depict in Fig. 4 a sketch of the experimental setup.

The incidence of the pumping beam was normal to the sample and the light was circularly polarized with the handedness opposite to that of the CLC helix in order to prevent selective reflection. The cell was placed on a translational stage to control the sample thickness. The output laser signal was focused by means of a lens of 5 cm of diameter onto a power meter. A 532 nm notch filter was placed just behind the sample to remove the pumping light (see Fig.4). For some experiments, the power meter was substituted by an optical-fiber spectrometer to analyze the spectrum of the emitted light.

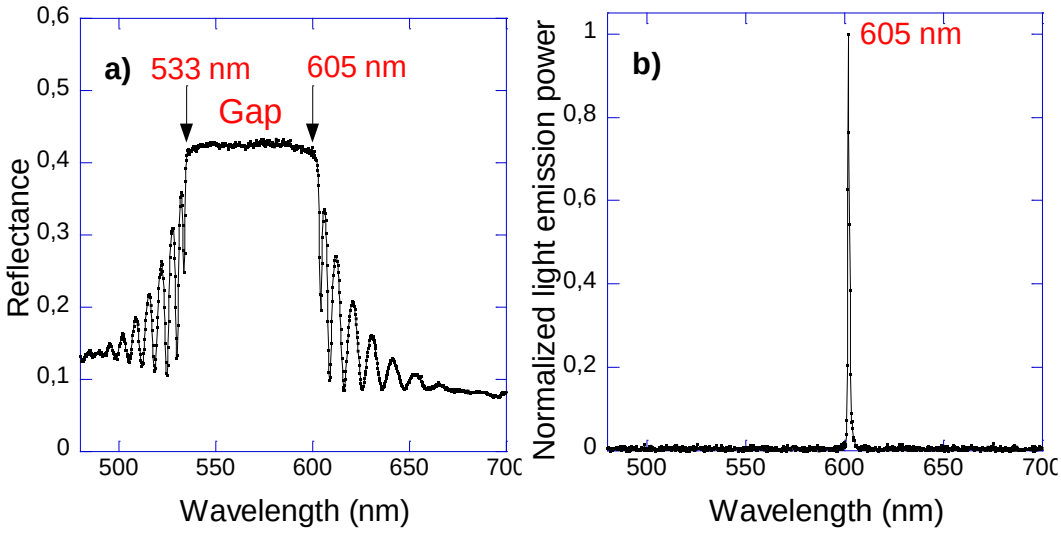

Fig. 3. Reflectance spectrum for unpolarized light of the CLC material. The background of the reflectance is due to the reflectivity of the external faces of the glasses and ITO (a). Normalized laser spectrum. The peak wavelength is 605 nm (b). Both measurements correspond to a commercial cell of 10 μm thickness.

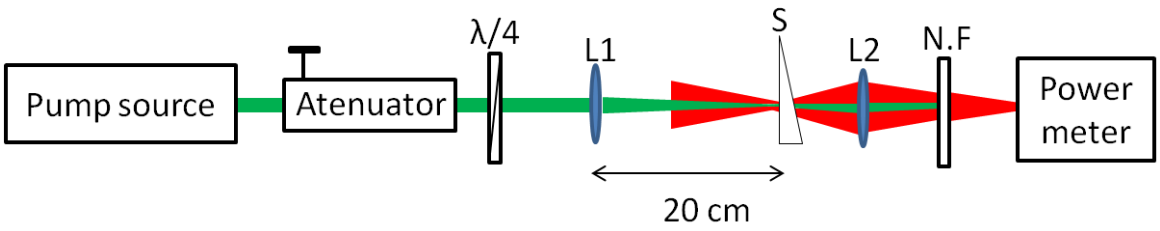

Fig. 4. Experimental setup for measuring the lasing performance as a function of the CLC sample thickness. L1 and L2 are lenses, S is the sample, and N.F is the notch filter to eliminate the pumping light.

As a next step we measured the laser emission power *vs.* the pump energy in order to determine the lasing thresholds and slope efficiencies. At low excitation energies, lasing is not observed, and the detected light is due to the fluorescence radiation collected by the lens behind the sample. Its intensity shows a linear behavior with the pumping energy. In order to separate the pure laser emission, the fluorescence contribution was subtracted from the total

signal using linear extrapolation. An example of this procedure is shown in Fig. 5.

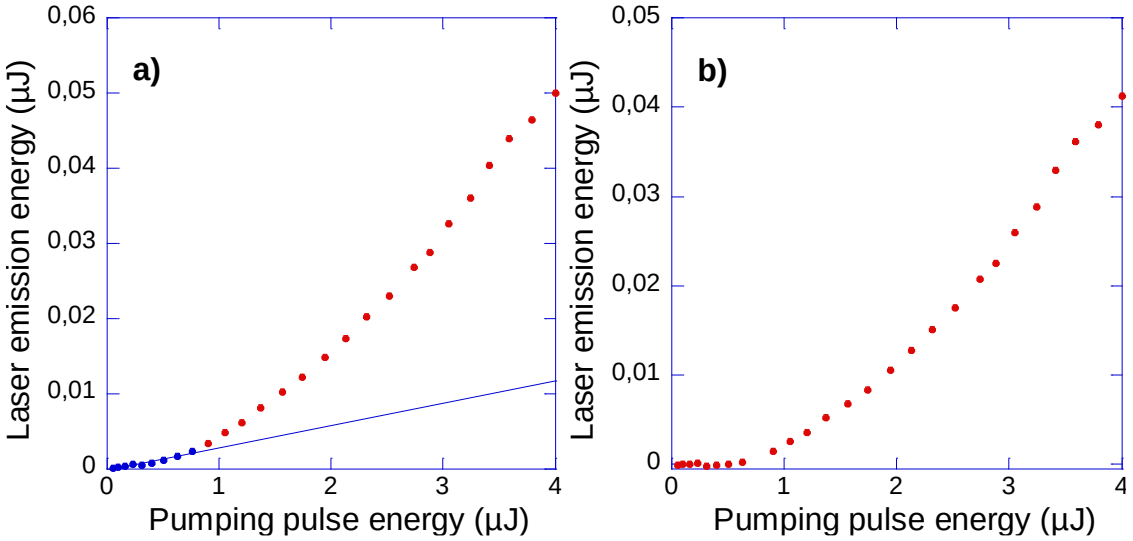

Fig. 5. Energy emission at 605 nm as a function of the incident pump energy, the blue line indicates the linear extrapolation (from the blue dots) due to the fluorescence contribution (a). Laser emission after subtraction of the fluorescence (b). Both graphs were obtained for a thickness of 12.8 µm.

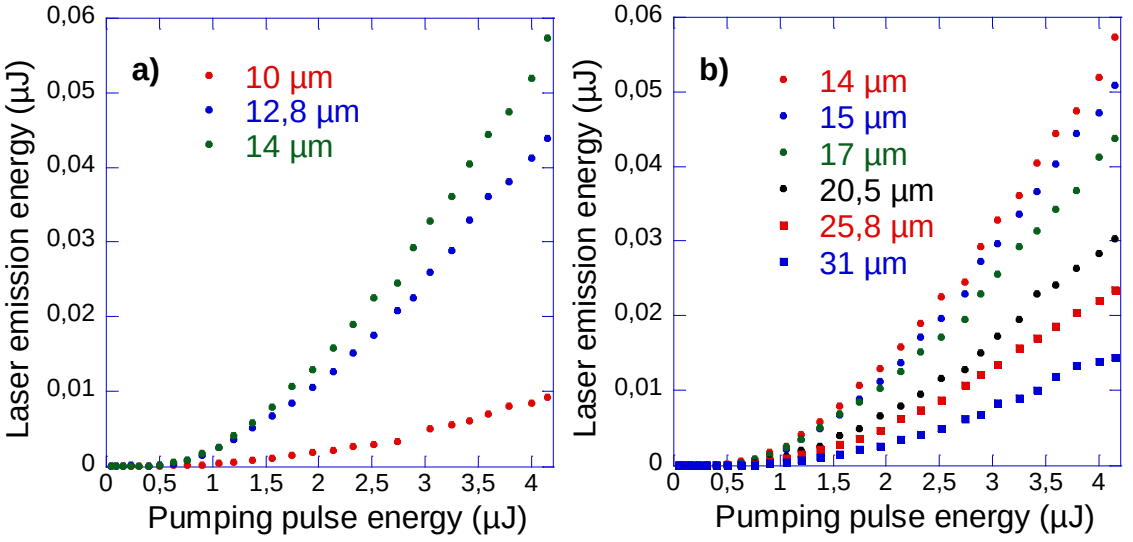

Fig. 6. Laser emission at 605 nm as a function of the incident pump energy for different sample thicknesses below (a) and above (b) the optimum thickness of 14 µm.

In Fig. 5(a), the blue dots are due only to fluorescence. These dots are fitted by linear extrapolation. The resulting line is the fluorescent contribution, which is subtracted to all the measured points; the result is shown in Fig. 5(b). Using this procedure we performed the measurements for different sample thicknesses. Results are shown in Fig. 6. For thicknesses below 8 μm, the fluorescence is dominant and the separation of fluorescence from laser emission is problematic. Furthermore, under 7 μm thickness no laser was observed.

From Fig. 6 we directly measured the slope efficiencies corresponding to each thickness. The slopes were doubled to take into account the laser emission from both sample faces. As can be seen, the maximum slope is achieved at 14 μm. The threshold energies were determined by inspection of the fluorescence spectrum of the CLC sample. For this task, the optical-fiber spectrometer was used instead of the power meter in Fig. 4. The E_{th} values correspond to the energy to which the intensity peak at the laser wavelength, as that of Fig. 3 (b), appears. This method allows for the determination of the E_{th} values with higher accuracy than that of the standard method based on the extrapolation of the linear fitting of the laser power to the pumping power[2]. In Fig. 7 we present a compilation of the measured slope efficiencies and threshold energies for the different thicknesses. From the figures, it is easily deduced that the previously proposed relation $\eta \propto 1/E_{th}$ does not hold. In addition, it is observed that the maximum of η is very sharp, contrary to what happens to the minimum of the threshold energy. In the latter case, the thickness corresponding to the lower threshold energy is not well defined within the experimental error. The experiment clearly indicates that the slope efficiency value determines by itself the whole performance of the laser, with E_{th} having much smaller influence.

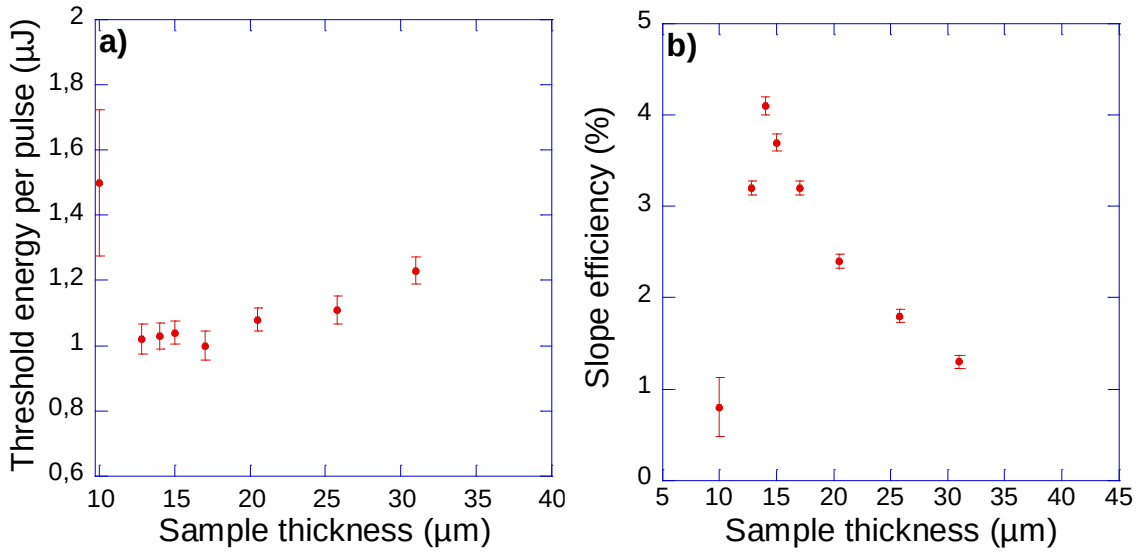

Fig. 7. Threshold energy per pulse of the pumping source (a) and slope efficiency of the laser emission *vs*. sample thickness.

In order to interpret our results, we will use the already mentioned model[10] based on the rate equations for the populations of the excited states and laser generation in CLCs. In the following section, the typical trends of the different variables will be analyzed.

3.3 A kinetic model for laser generation in CLCs

The recently proposed model for laser generation in CLCs makes use of kinetic equations for the excited states populations and generated light[10]. The approach is standard in ordinary laser physics and only incorporates the peculiarity of the CLCs through the radiation dwelling time in the CLC layer τ_c. We have already introduced this parameter in chapter 2, τ_c is given by Eq. (2.50):

$$\frac{1}{\tau_c} = \frac{c}{n}\left(\beta + \frac{4P^2}{\alpha^2 L^3}\right), \tag{3.15}$$

where L is the is the length of the resonant cavity, P is the pitch of the helix, β is the coefficient of distributed losses, which accounts for the absorption and

scattering in the CLC sample, $n = \sqrt{\frac{n_o^2+n_e^2}{2}}$ is the mean refractive index and $\alpha = \frac{(n_o^2-n_e^2)}{(n_o^2+n_e^2)}$ is the optical anisotropy parameter.

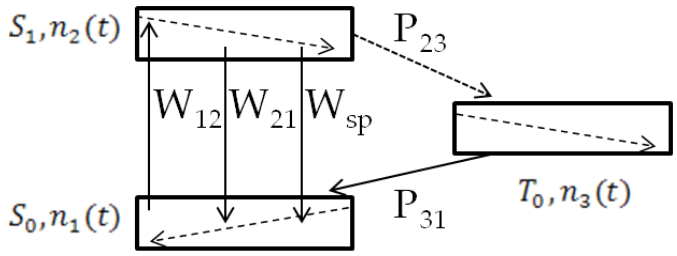

Fig. 8. Diagram of energy levels in a typical dye molecule. Solid arrows indicate radiative transitions, dashed arrows indicate thermal processes within an energy band and the dotted arrow indicates intercombination transitions from an excited singlet to a triplet level. W_{ij} are the probabilities of induced transition from level i to level j upon emission or absorption of a photon, W_{sp} is the probability of spontaneous transition from S_1 to S_0 upon emission of a photon and P_{ij} are the probabilities of transition from level i to level j.

A detailed deduction of the mentioned rate equations is found section (2.7). Here, directly, we will present such equations, as they appear in their final form in Ref. 10:

$$\frac{dn_2(t)}{dt} = -\left(\frac{\sigma_e P_e(t)}{h\nu_e S} + \frac{1}{\tau_{21}} + \frac{\sigma_a P_{a0}(1+\exp[-\sigma_a n_1(t)L])}{2h\nu_a S} + P_{23}\right) n_2(t)$$
$$- \frac{\sigma_a P_{a0}(1+\exp[-\sigma_a n_1(t)L])}{2h\nu_a S}\ n_3(t) + \frac{NP_{a0}(1-\exp[-\sigma_a n_1(t)L])}{h\nu_a S L n_1(t)},$$

$$\frac{dn_3(t)}{dt} = P_{23}n_2(t) - P_{31}n_3(t)\,, \tag{3.16}$$

$$\frac{dP_e(t)}{dt} = \frac{c}{n}\left(\sigma_e P_e(t) + k\frac{h\nu_e S}{\tau_{21}}\right) n_2(t) - \frac{P_e(t)}{\tau_c},$$

where $n_1(t)$, $n_2(t)$ and $n_3(t)$ are the ground singlet, first excited singlet and ground triplet levels respectively (see Fig. 8), P_{a0} is the pumping power, S the illumination area, L the thickness of the sample, τ_{21} the fluorescence lifetime of

level 2, and σ_a and σ_e the cross section of absorption and induced emission respectively. The k coefficient is the fraction of spontaneous radiation at the laser frequency that travels along the helix axis; it can be considered as the seed for lasing. $h\nu_a$ and $h\nu_e$ are the energies of absorbed and emitted photons respectively. The density of dye molecules N is given by $N = n_1(t) + n_2(t) + n_3(t)$. Finally $P_e(t)$ is the power of emitted light inside the CLC layer and P_{ij} is the probability of transition from level i to level j.

Two comments are in order regarding the above system of equations: First, if we look at the third equation of system (3.16), we can see that the terms between brackets represent the power x m² generated inside the resonant cavity. Nevertheless, in the second of those terms the fluorescence lifetime of level 2, τ_{21} is used. But the decay of level 2 involves radiative and nonradiative phenomena. Because we are interested in radiative deexcitation, τ_{21} must be replaced by the lifetime of radiative spontaneous emission τ_r in such equation. Secondly, in these equations, $P_e(t)$ represents the generated power inside the cavity. However, in real experiments, only photons that escape outside the cavity are measured. The light power outside the laser cavity can be obtained in the following way: If Φ is the number of photons inside the cavity, the rate at which the number of photons inside the CLC layer decreases is $1/\tau_c$. However, only the photons that are not absorbed or scattered give rise to the laser output. As a consequence, we can consider that the output rate of laser photons is $1/\tau_c^0$, where τ_c^0 is obtained from Eq. (3.15) with $\beta = 0$. Therefore, the output power of the laser emission P_{out} is given by

$$P_{out} = h\nu_e \frac{\Phi}{\tau_c^0}\,. \tag{3.17}$$

Φ and the power of emitted light inside the cavity, P_e, are related by

$$P_e = h\nu_e \frac{\Phi}{SL}\frac{c}{n}S\,, \tag{3.18}$$

Then

$$P_{out} = \frac{L}{\left(\frac{c}{n}\right)} \frac{P_e(t)}{\tau_c^0} . \tag{3.19}$$

So, the light power outside the cavity P_{out} is a fraction of the light power inside the cavity P_e. This fraction is simply the number of times that the photons cover the sample length L before escaping from the cavity.

3.3.1 A typical example

In order to get a better understanding of Eqs. (3.16), we present here a typical case for the level population behavior under fluorescence and laser generation regimes. For this task, we will numerically solve Eqs. (3.16) and study the evolution of $n_1(t)$, $n_2(t)$, $n_3(t)$ and $P_e(t)$ as the pumping energy is increased. The values of the used parameters appear in detail in Table 1, where τ_f (fluorescence lifetime) replaces τ_{21} in the first of Eqs. (3.16) and τ_r (radiative lifetime) plays the same role in the third one. Data were obtained from the literature and from our experimental parameters.

Parameter	Value
P (μm)	0.352
n	1.6
α	0.125
P_{31} (s^{-1}), P_{23} (s^{-1})	10^4, $5x10^7$
τ_f (ns), τ_r (ns)	1.2, 2.4
K	10^{-7}
σ_e (cm^2), σ_a (cm^2)	$0.8x10^{-16}$, $0.35x10^{-16}$
β (cm^{-1})	350
S (μm^2)	$1.26x10^3$
L(μm)	12
N (cm^{-3})	$1.8x10^{19}$

Table 1. Parameters used for the simulations. The pumping and laser emission wavelengths were 532 and 605 nm, respectively.

Here we study different pumping regimes, below the threshold, at the threshold and above the threshold. For the simulations we have represented the pumping source as a typical Gaussian pulse of 14 ns (FWHM) (see Fig. 9).

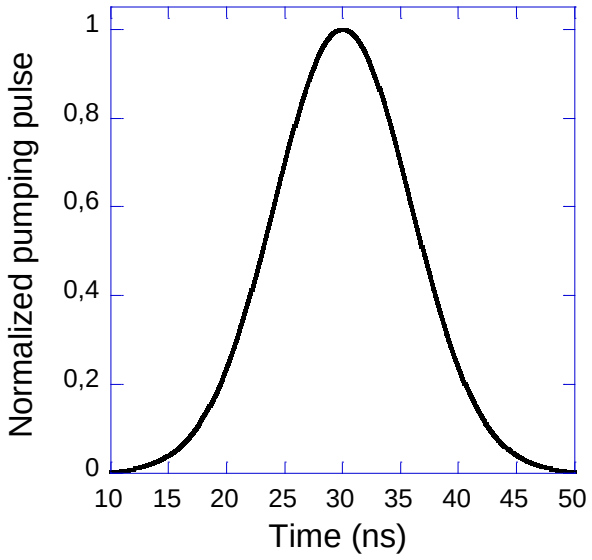

Fig. 9. Normalized temporal profile of a simulated typical pumping pulse.

Well below the threshold, the emitted power per pulse is very low and the profiles of the pulses are similar to that of the pump (see Fig. 10). As the pumping power is increased, the emitted profiles barely change and their power increases linearly with the pump; under this regime there is no lasing but fluorescence. Near the threshold, the emitted pulses show an abrupt change: emitted power increases in several orders of magnitude and their temporal profiles become very sharp. At the threshold, a minimum width is reached at the same time as the power increases several orders of magnitude. Above the threshold, lasing occurs showing spiking. We have used the point of minimum width, just before spiking starts, for determining the thresholds (see Fig. 10).

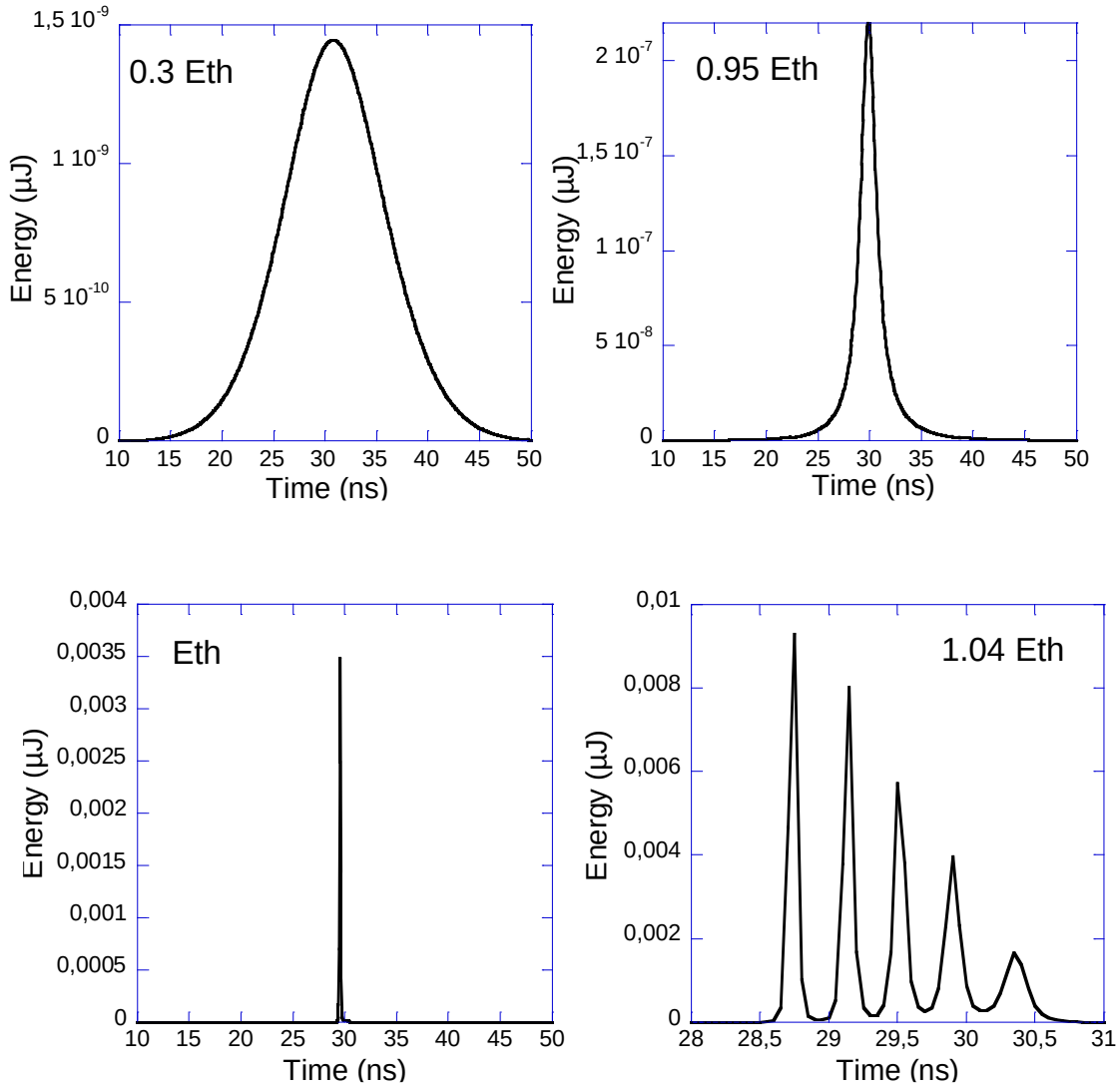

Fig. 10. Simulated temporal profiles of laser emission pulses for different pumping energies per pulse up to the threshold, and just above the threshold. Notice that a minimum width is reached at the threshold.

The excited singlet is the responsible for lasing, thus $n_2(t)$ is the population responsible for laser generation. In Fig. 11 we can see that under low pumping regime less than a 20% of the dye molecules are in level 2, furthermore, it shows a gaussian profile similar to that of the pump. As pumping power is increased, at the threshold, a maximum of ~40 % of the dye molecules are excited to level 2. Interestingly, above the threshold, even under high pumping regime, population inversion does not exceed 40% of the dye molecules. This behavior

is due to stimulated emission. Once the required population inversion is achieved (n_2^{th}), the expected increase of the population in level 2 is compensated by de-excitation by stimulated emission. An increase in the pumping power, results in a temporal plateau in the population of n_2 that is enlarged in duration as the energy increases. Strictly speaking, above the threshold $n_2(t)$ is not constant but describes damped oscillations around n_2^{th}. On the other hand, excited molecules in level 2 can also undergo nonradiative transitions to the triplet level. These transitions are governed by the lifetime P_{23}. Furthermore, since P_{23} is much larger than P_{31}, the population $n_3(t)$ increases monotonously, as shown in Fig.12. Therefore, this dye population is excluded for laser generation.

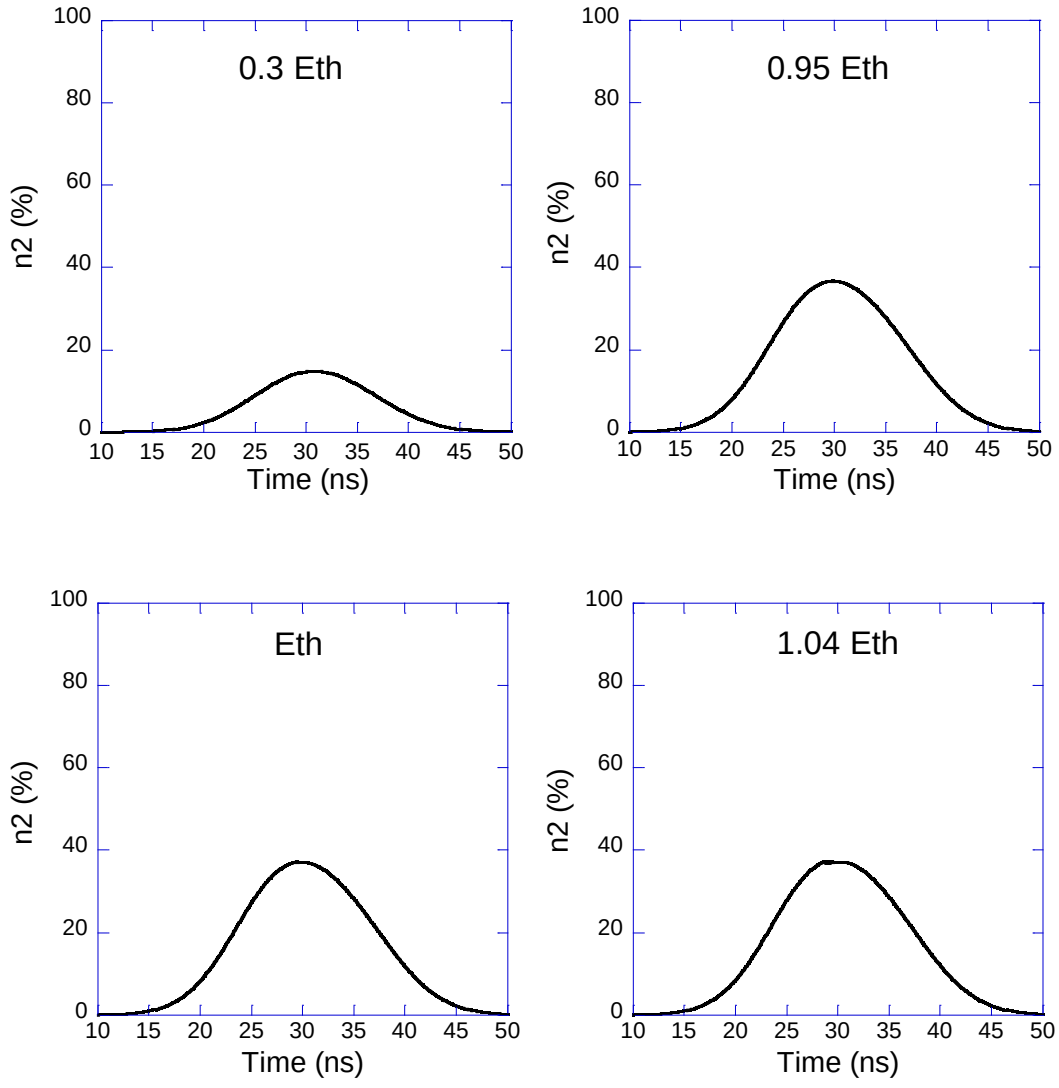

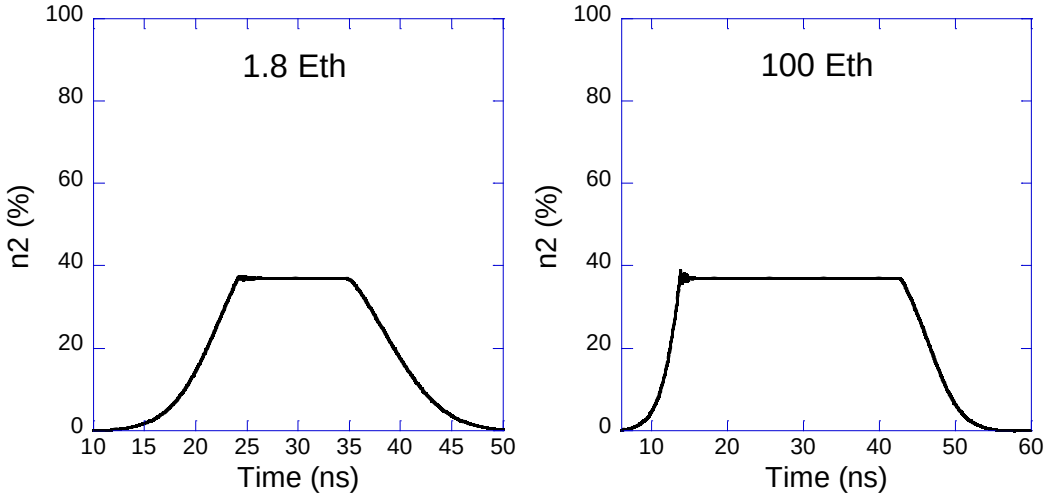

Fig. 11. Simulated temporal profiles of $n_2(t)$ for different pumping regimes. Notice that at the threshold a maximum population n_2^{th} is reached. For higher pumping energies the $n_2(t)$ value remains constant at the maximum (n_2^{th}) during a certain time. The higher the pumping energy the longer the time.

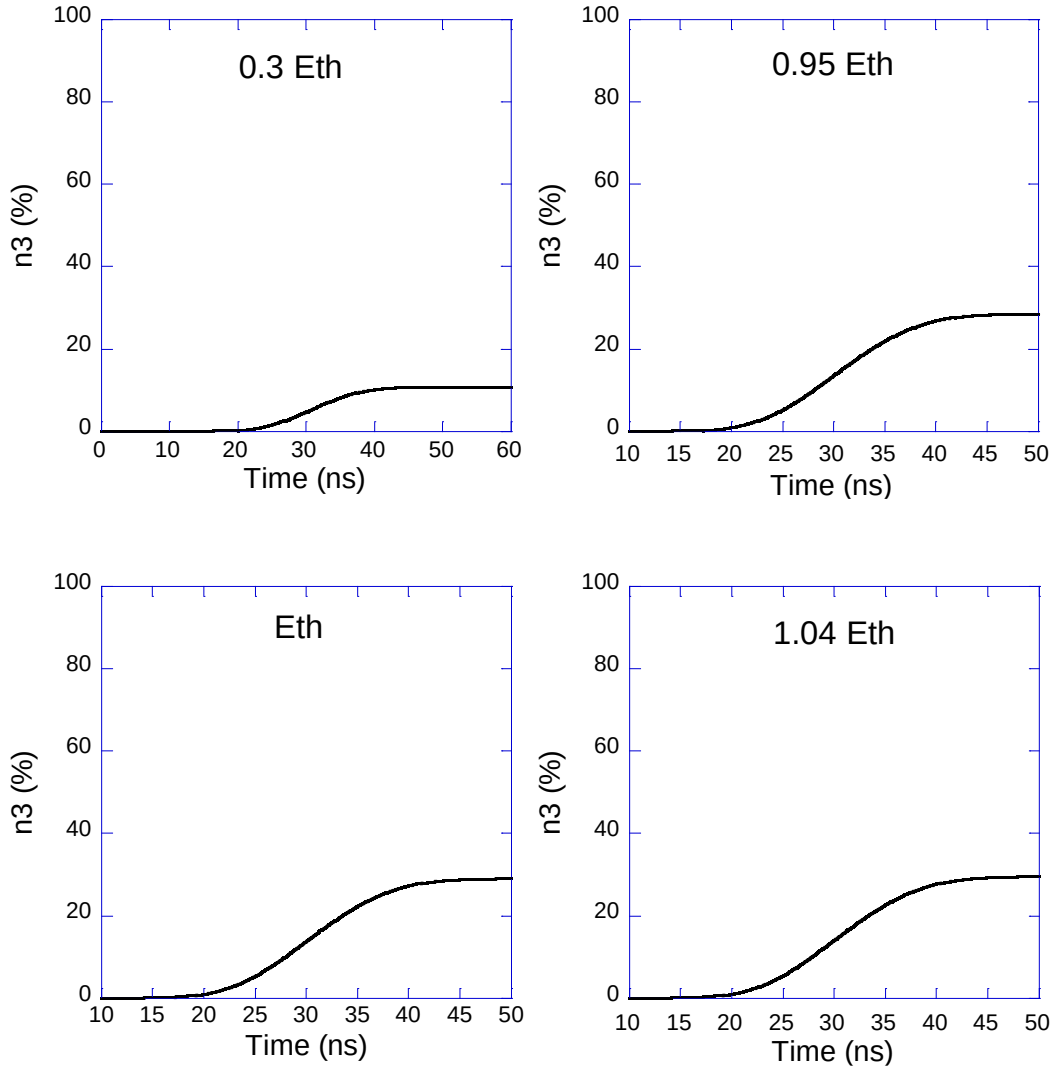

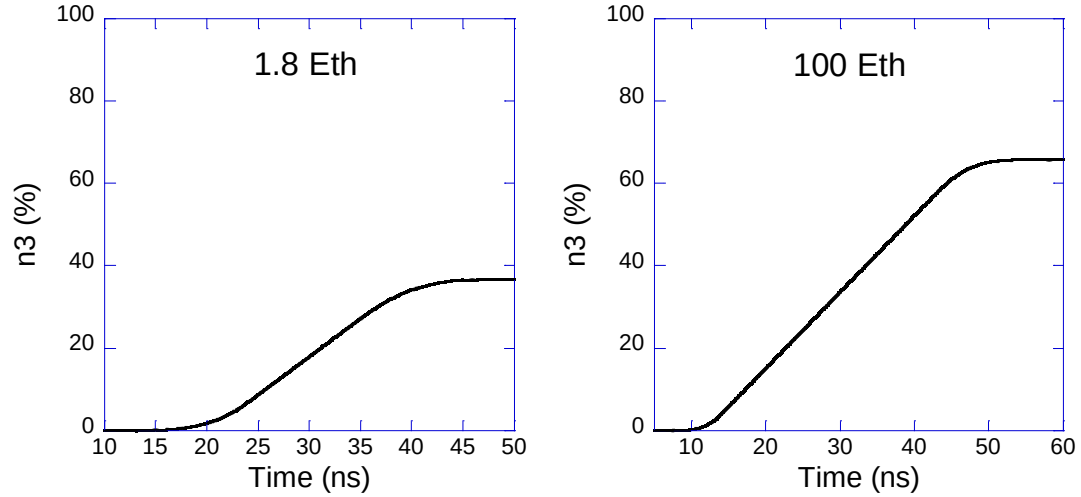

Fig. 12. Simulated temporal profiles of $n_3(t)$ for different pumping regimes. Notice that the maximum of n_3 increases monotonously as the pumping energy increases. Due to the low rate of de-excitation to the fundamental level (P_{31}) the maximum n_3 value is maintained for a relatively long time; in our case for about 200 μs.

Thus, for very intense pulses, the time for which the level 3 is being excited is very long and therefore, lasing cannot be maintained. This behavior is shown in detail in Fig. 13.

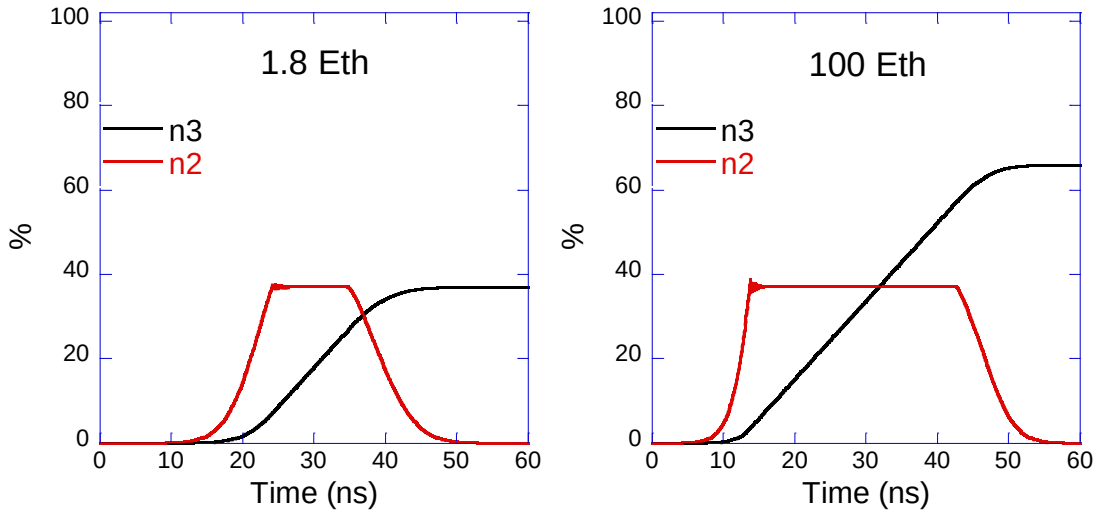

Fig. 13. Temporal profiles of $n_2(t)$ and $n_3(t)$ for different pumping regimes. In the case of 1.8 E_{th}, the duration of laser pulse is not limited for the value of the population n_3, on the contrary for 100 E_{th} it is, since the proportion of dye molecules excited in the level 3 is too high .

Fig. 13 shows the temporal profiles of $n_2(t)$ and $n_3(t)$ for two different pumping regimes. For a pumping energy of 1.8 E_{th} the duration of the laser

pulse is not limited by the dye population excited to level 3, i.e. $n_3 \leq N - n_2^{th}$. On the contrary, in the case of 100 E_{th} the laser emission decays once the previous condition is not fulfilled. This fact carries with serious limitations for the construction of CLC continuous lasers.

For the sake of completeness it is also interesting to have a look to the evolution of $n_1(t) = N - n_2(t) - n_3(t)$, see Fig. 14. The same information as that of Figs. 11-13 can be deduced, i.e. under low pumping regime, the population of the ground state decreases, as molecules are excited to level 2 and from level 2 to 3. Molecules in level 3 are excluded for laser generation during a relatively long period of time respect to the duration of the pump. When $n_3 \geq N - n_2^{th}$ occurs, population inversion is prevented.

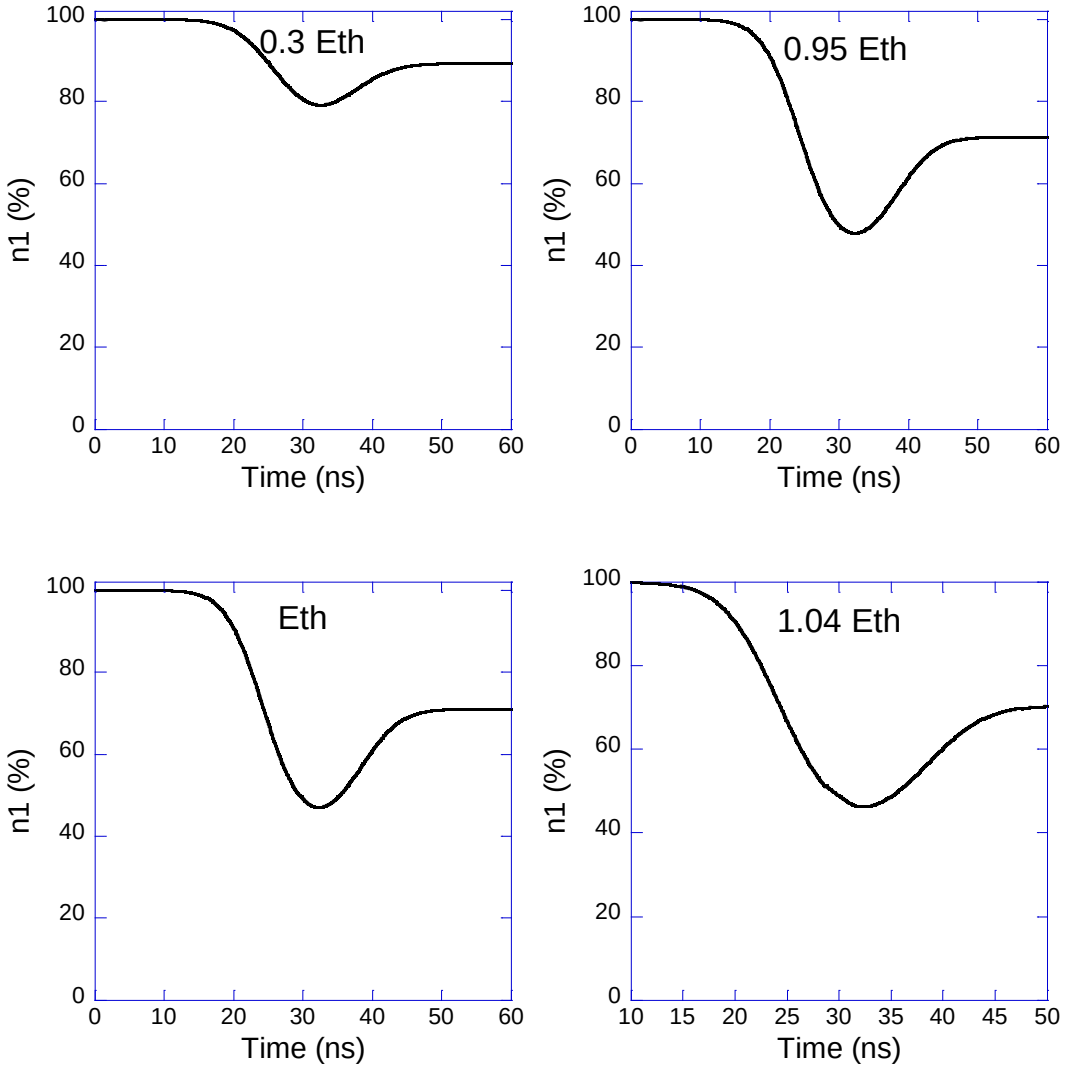

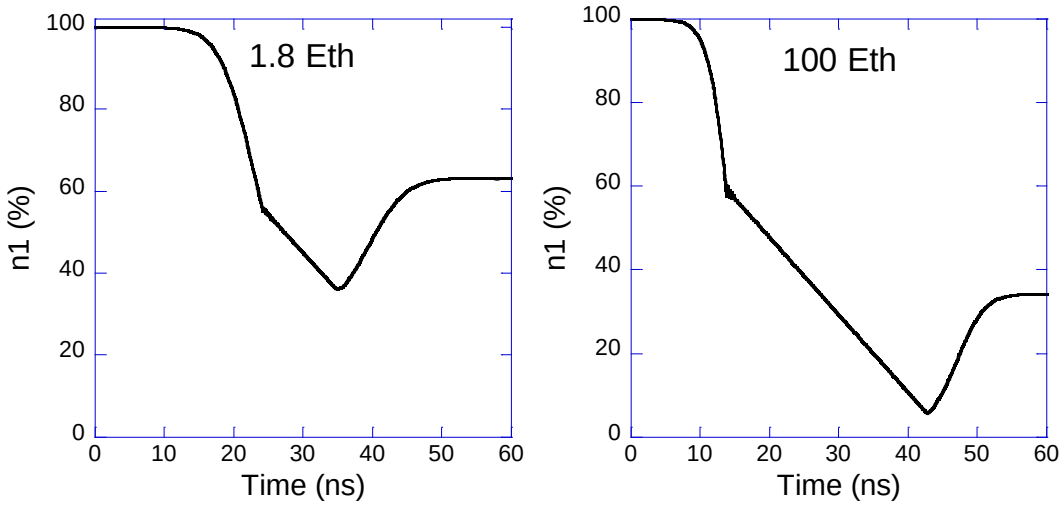

Fig. 14. Simulated temporal profiles of $n_1(t)$ for different pumping regimes.

3.4 Dependence of E_{th} and η on the sample thickness. Numerical simulations and discussion

By means of Eqs. (3.16) and (3.19) we calculated numerically E_{th} and η corresponding to different values of the sample thickness and we compared them to our experimental results (section 3.2). The used parameters are shown in Table 1.

We first obtained the coefficient of distributed losses β of our sample from the experimental values of E_{th}. With $\beta = 350$ cm^{-1}, the calculated threshold energies are in reasonable agreement with the observed E_{th} for all the sample thicknesses (see Fig. 15). Such coefficient affects greatly to the pumping threshold and the slope efficiency.

On the other hand, in Fig. 16 we show the calculated η values together with our experimental results. Red points in Fig. 16 are the simulated slope efficiencies and black dots are the experimental results. A very good accordance is obtained with the observations, in particular, the existence of an optimum L is well

reproduced. Remarkably, the optimum thickness is rather insensitive to the β value, showing changes smaller than 1 μm for β variations in the range 100–400 cm^{-1}. Something similar happens with the dependence on the dye concentration: the position of the maximum only decreases slightly as N is raised within reasonable ranges.

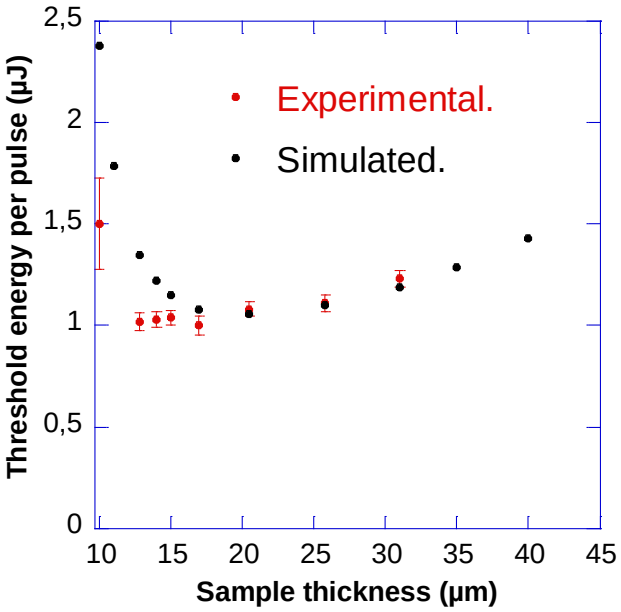

Fig. 15. Threshold energy per pulse of the pumping source *vs.* sample thickness. Red circles represent the experimental results and black circles the values calculated numerically.

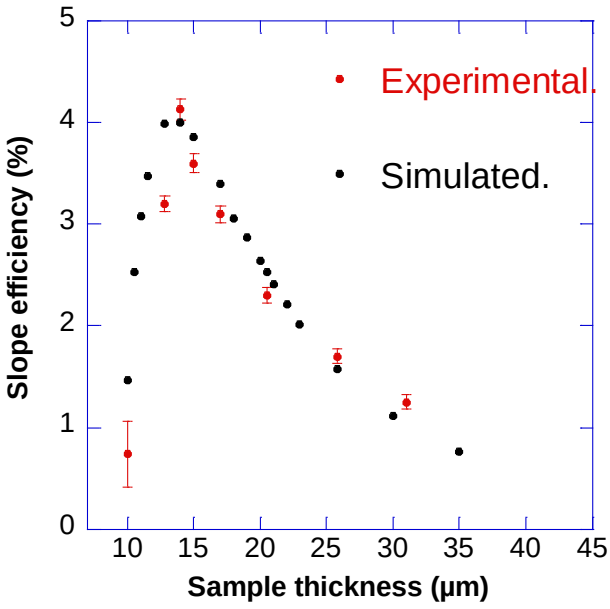

Fig. 16. Slope efficiency of the laser emission *vs.* sample thickness. Black circles represent the experimental results and red circles the values calculated numerically. The theoretical values are normalized by a factor of 0.7 in order to get coincidence with the experimental values.

It is worth noting that though the shapes of the $\eta(L)$ curves are predicted accurately, the absolute values of the calculated efficiencies are always overestimated (typically a factor between 1 and 2 is found, see the caption of Fig. 16). This is easy to understand because, in practice, there are additional contributions to the laser radiation from modes that propagate away from the cell normal. These modes, in general, are activated at higher thresholds and present smaller η. Obviously, they are not considered in our 1D model. In particular, the so-called leaky modes[12], which propagate within the glasses at grazing angles, are known to provoke dramatic reductions of the Bragg-mode lasing efficiency if precautions are not taken[13].

It is worth noticing that, except for small thicknesses, E_{th} only shows a slight L dependence for $L > 12$ μm in contrast to what happens with the slope efficiency, that shows a much more pronounced dependence. Also, we observed that despite variations in β affect greatly to E_{th}, variations within a reasonable range (100-400 cm^{-1}) do not affect to the position of the minimum of E_{th}.

As a conclusion, we have seen that Shytkov and Palto's model can numerically account for most of our experimental results. In especial those related to the dependence of the slope efficiency and threshold energy on the sample thickness. Even more interesting would be the deduction of analytical expressions for these quantities as a function of the main parameters of CLC lasers. This is the objective of the next section.

3.5 Analytical approximations for the slope efficiency and threshold

Starting with η, let assume that we are under high pumping level conditions. Then, η is simply equal to the ratio between the emitted and input energies, since E_{th} is much smaller than the pumping energy. Firstly we will assume that the absorbed pumping energy is completely transformed into laser radiation. This assertion it is not strictly true since a small amount of the energy is emitted as fluorescence and also through non-radiative processes. However, these contributions will be disregarded.

The fraction of pumping energy that is absorbed after traversing the sample is:

$$\left[1 - \exp[-\sigma_a \langle n_1(t)\rangle L]\right], \tag{3.20}$$

where $\langle n_1(t)\rangle$ is the temporal average of the population density of the ground level during the lasing.

Then, taking into account the different energy between absorbed and emitted photons, the ratio of absorbed-emitted energy is

$$\frac{h\nu_e}{h\nu_a}\left[1 - \exp[-\sigma_a \langle n_1(t)\rangle L]\right]. \tag{3.21}$$

However, not all the emitted photons escape from the cavity. Some of them are lost due to the coefficient of distributed losses β. So, taking into account that the efficiency with which the absorbed pumping photons are transformed into laser photons outside the cavity is (τ_c/τ_c^0), the slope efficiency can be expressed as follows:

$$\eta = \frac{h\nu_e}{h\nu_a}[1 - \exp(-\sigma_a \langle n_1(t)\rangle L)]\frac{\tau_c}{\tau_c^0}. \tag{3.22}$$

Remember that in Eq. (3.22), $\langle n_1(t)\rangle$ is the time average population density of the ground state during the lasing, i.e., $\langle n_1(t)\rangle = N - \langle n_2(t)\rangle - \langle n_3(t)\rangle$. In order to calculate $\langle n_1(t)\rangle$, we first recall that our simulations show that $n_2(t)$ is approximately constant during lasing (see Figs. 11 and 13), with a value $n_2(t) \approx n_2^{th}$, where n_2^{th} is given by[14]

$$n_2^{th} = \frac{n}{c\sigma_e\tau_c}\,, \tag{3.23}$$

irrespective of the pumping power.

On the other hand, since $P_{31} < P_{23}$ (see Table 1), the second equation of system (3.16) results in

$$\frac{dn_3(t)}{dt} \approx P_{23}n_2(t)\,, \tag{3.24}$$

so the population density of the triplet level during lasing process is (see Fig. 12 for 100 E_{th})

$$n_3(t) \approx n_2^{th}P_{23}t\,. \tag{3.25}$$

Thus, under strong pumping regime, $n_1(t)$ has an approximate evolution (see Fig. 14 for 100 E_{th})

$$n_1(t) = N - n_2^{th} - n_2^{th}P_{23}t\,. \tag{3.26}$$

Therefore, taking an average in Eq. (3.26), we can write

$$\langle n_1\rangle = N - n_2^{th} - n_2^{th}P_{23}\frac{\Delta\tau_l}{2}\,, \tag{3.27}$$

where $\Delta\tau_l$ is the time interval during which the lasing takes place. That is, the time during which population inversion is maintained.

Introducing this last result in Eq. (3.22) we have an analytic expression for $\eta(L)$. Continuous line in Fig. 17 represents the analytical approximation for $\eta(L)$. We have taken $\Delta\tau_l \approx 3\Delta\tau_p$, where $\Delta\tau_p$ is the full mean width of the pumping pulse. Notice that for very intense pulses $\Delta\tau_l$ could be theoretically much higher than $\Delta\tau_p$ but, in practice, for moderate excitations, both times are of the same order of magnitude, and $\Delta\tau_l$ is a few times larger than $\Delta\tau_p$ at most. This possible difference barely affects to the shape of $\eta(L)$, and only contributes as a scale factor. The rest of the parameters are those in Table 1. A very good agreement is found with the numerical calculations obtained by solving Eqs. (3.16) (see Fig. 17). Nevertheless, as in the case of numerical data, we had to normalize $\eta(L)$ by a factor 0.7 in order to get coincidence with the experimental values.

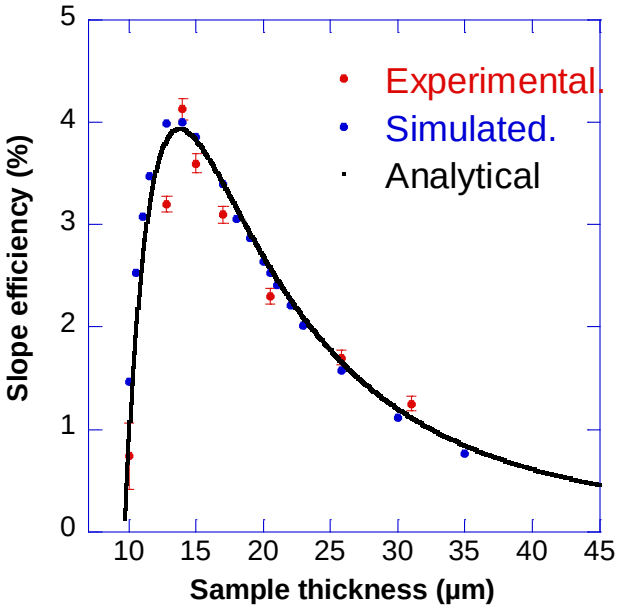

Fig. 17. Slope efficiency of the laser emission *vs.* sample thickness. Blue circles represent the experimental results, red circles the values calculated numerically and the continuous line correspond to the results calculated from the analytical expression (3.22). The theoretical values, i.e., blue circles and continuous line, are normalized by a factor of 0.7 in order to get coincidence with the experimental values.

Eqs. (3.22) and (3.27) clearly show the pernicious effect of the triplet state. It reduces the effective population of level 1 and thus contributes to reduce the

fraction of the pumping energy absorbed by the system. The effect is the worse the longer the pumping pulse as previously shown in the study of the temporal profile of n_3 (see Figs. 12 and 13). This is the main drawback for achieving CW lasers made of CLCs doped with organic dyes[15].

It is interesting to note the existence of a minimum thickness L_{min} below which lasing is impossible. This is easy to interpret and corresponds to the situation where all the dyes in the sample are needed to produce the required population inversion n_2^{th}, i.e., $N = n_2^{th}$. Using Eqs. (3.15) and (3.23), this condition implies

$$L_{min} = \left[\frac{4P^2}{(N\sigma_e - \beta)\alpha^2}\right]^{1/3} . \tag{3.28}$$

With the data of Table 1, we get $L_{min} = 6.6$ μm, which fits rather well with our experiment, in which laser emission was hard to be observed for thicknesses below 7 μm. The numerical value of L_{min} is relatively unaffected by variations of β within reasonable ranges. For example for $\beta = 100$ cm^{-1}, $L_{min} = 6.2$ μm and for $\beta = 500$ cm^{-1}, $L_{min} = 7$ μm. Eq. (3.28) also shows that raising β above a certain limit can kill completely the laser operation ($L_{min} = \infty$). This situation occurs for losses above $\beta_{lim} = N\sigma_e$. In our case, $\beta_{lim} \approx 1500$ cm^{-1}, which shows the importance of using a sample of good quality in practical devices.

We finally turn to deducing an analytical expression for $E_{th}(L)$. When the pumping level achieves the threshold value, the population density of level 2 must be n_2^{th}. The process of raising $n_2(t)$ up to the threshold value n_2^{th} is driven by the pumping pulse. Therefore $n_2(t)$ exhibits a temporal profile similar to that of the pumping pulse, at least up to its maximum.

Therefore, if the pumping pulse is Gaussian, we have:

$$n_2(t) = n_2^{th}\exp\left[-\left(\frac{t - t_0}{\Delta\tau_p/2}\right)^2 \ln(2)\right], \tag{3.29}$$

for $t \leq t_0$, where t_0 is the corresponding time the maximum of the pumping pulse. Under the assumption $P_{31} \ll P_{23}$, we can integrate Eq. (3.24) to obtain the population of level 3 at the threshold n_3^{th}. The result is

$$n_3^{th} = n_2^{th}\sqrt{\frac{\pi}{16ln2}}P_{23}\Delta\tau_p \approx 0.53 n_2^{th}P_{23}\Delta\tau_p \,. \tag{3.30}$$

On the other hand, the pumping energy at the threshold must satisfy the equation

$$\frac{1}{2}\frac{E_{th}}{h\nu_a SL}\left[1-\exp\left(-\sigma_a L n_1^{th}\right)\right] = n_2^{th} + n_3^{th} + \int_{-\infty}^{t_0}\frac{n_2(t)}{\tau_f}dt \,, \tag{3.31}$$

where $n_1^{th} = N - n_2^{th} - n_3^{th}$. The left-hand side of Eq. (3.31) is approximately the density of photons absorbed up to the maximum of the pumping pulse. The factor 1/2 indicates that only half the energy of the pulse is required for achieving the threshold. $(\frac{1}{2})\frac{E_{th}}{h\nu_a SL}$ is the density of photons in the cavity, per pulse, when the threshold energy is reached, and the term in brackets is the fraction of such photons that are absorbed. These photons raise the population of levels 2 and 3 up to their corresponding thresholds. The last term of the right-hand side of Eq. (3.31) stands for the drop of population of level 2 due to fluorescence. By integrating that term, we get

$$E_{th} = 2h\nu_a SL n_2^{th}\frac{\left(1+0.53\Delta\tau_p\left(P_{23}+1/\tau_f\right)\right)}{1-\exp\left(-\sigma_a n_1^{th}L\right)} \,. \tag{3.32}$$

Continuous line in Fig. 18 shows the threshold energy obtained by using Eq. (3.32) with the parameters of Table 1. As can be seen, the agreement with the numerical values deduced from Eqs. (3.16) (blue points) is excellent. For relatively large L or high dye concentrations, the dependence of the

denominator of (3.32) on L is small. In such case, by using Eq. (3.23), it is straightforward to deduce that $E_{th}(L)$ behaves approximately as L/τ_c, i.e., has a L dependence given by $\beta L + \frac{4P^2}{(\alpha L)^2}$ in accordance to reference 8. Differentiating respect to L and equaling to 0 we can see that the thickness for the smallest E_{th} scales then as $\beta^{-1/3}$.

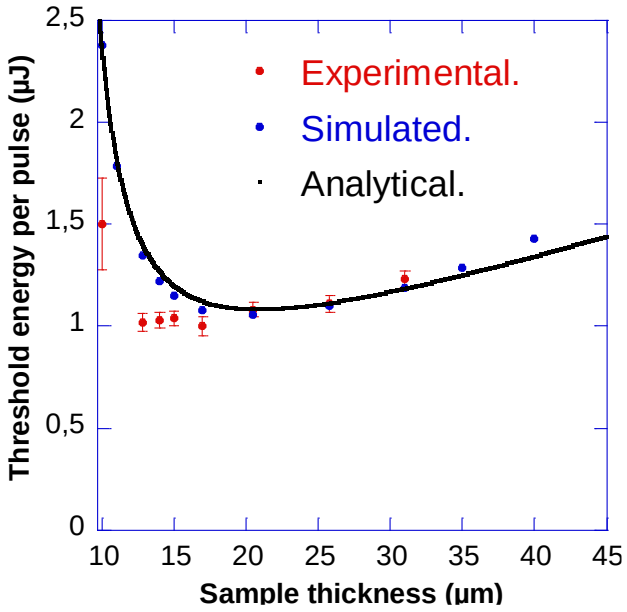

Fig. 18. Threshold energy per pulse of the pumping source *vs.* sample thickness. Red circles represent the experimental results, blue circles the values calculated numerically and the continuous line correspond to the results calculated from the analytical expression (3.32).

It is interesting to connect the L-dependences of η and E_{th}. Multiplying both analytical expressions, using Eq. (3.23) and in the thickness range in which the exponential terms in Eqs. (3.22), (3.32) can be disregarded we get:

$$E_{th}(L)\eta(L) \approx 2Sh\nu_e \frac{n}{c\sigma_e}\left(1 + 0.53\Delta\tau_p\left(P_{23} + 1/\tau_f\right)\right)\frac{L}{\tau_c^0} = A\frac{L}{\tau_c^0}, \qquad (3.33)$$

where A is independent of L. The dwelling time in the absence of losses scales as $\tau_c^0 \propto L^3$ (see Eq. (3.15)), and therefore

$$E_{th}(L)\eta(L) \propto \frac{1}{L^2}\,. \tag{3.34}$$

This behavior contrast with that found on a F-P cavity, where τ_c^0 is simply proportional to the cavity length, $\tau_c^0 \propto L$, and thus $E_{th}(L)\eta(L) \approx constant$. For large cavity thicknesses, the factor $1/L^2$ in (3.34) reduces the $\eta(L)$ values in CLC lasers with respect to those expected in normal lasers. This conclusion contrast with the general belief that the expression $\eta \approx 1/E_{th}$, valid for F-P cavities can be extrapolate to CLC lasers, as in fact was assumed in references 2, 3, 4 and 7.

3.6 Conclusions

In this chapter we have studied some general features of the laser generation in CLCs and we have clarified several aspects that affect the laser performance. In this respect, we have make clear several points that were misinterpreted up to now and we have obtained analytical expressions that will be useful tools to design efficient CLC lasers. Especial attention has been paid to the role played by the sample thickness in the performance of CLC lasers. We have found, both experimentally and theoretically, that there is a minimum for $E_{th}(L)$ and a maximum for $\eta(L)$ at somewhat different thicknesses. The assumption $\eta \propto 1/E_{th}$, previously assumed by most of the researchers in this field, does not hold but the maximum for $\eta(L)$ is more prominent than that of $1/E_{th}$ and, in practice, determines the best laser performance. Interestingly, the optimum thickness is almost a constant independently of variations of β or N within realistic ranges.

Analytical expressions for E_{th} and η have also been deduced. These expressions are in excellent agreement with the numerical calculations and permit to analyze easily the influence of the dye and CLC parameters on the performance of the laser. Considering the cavity thickness, both relations show that there is a

competition between two phenomena. On the one hand, the quality of the resonant cavity, which is characterized by τ_c, increases as L increases (see Eq. (3.15)). In analogy with conventional mirror lasers this is equivalent to an increase in the mirrors reflectivity. This is why in the low thickness range, laser performance improves as L increases. However, the proportion of laser light that escapes the CLC sample decreases as the thickness is enlarged as a consequence of the increase of τ_c^o, as shown in Eq. (3.19). This is why it is important to find the best commitment between both competing phenomena. Also, the analytical expressions deduced for E_{th} and η show that the quantum yield to the triplet level and the width of the pumping pulse has been found to have a similar effect in the laser operating mechanism. The increase of both is detrimental to the laser. This explains, partially, the difficulty in the realization of lasers pumped by CW light sources in these structures. Other factors such as the thermal stability of the cholesteric helix should also be solved to succeed in the fabrication of these kind of lasers.

[1] W. Koechner and M. Bass, *"Solid-State Lasers: A Graduate Text"*, Springer (2003).

[2] W. Cao, P. Palffy-Muhoray, B. Taheri, A. Marino and G. Abbate, *Mol. Cryst. Liq. Cryst.* **429**, 101 (2005).

[3] L. M. Blinov, *JETP Lett.* **90**, 166 (2009).

[4] S. M. Morris, A. D. Ford, C. Gillespie, M. N. Pivnenko, O. Hadeler and H. J. Coles, *J. SID*, **14**, 565 (2006).

[5] V. I. Kopp, Z. Q. Zang and A. Z. Genack, *Opt. Lett*. **23**, 1707 (1998).

[6] I. Il'chishin, E. Tikhonov, A. Tolmachev, A. Fedoryako and M. Shpak, *Mol. Cryst. Liq. Cryst.* **191**, 351 (1990).

[7] S. M. Morris, A. D. Ford, M. N. Pivnenko, O. Hadeler and H. J. Coles, *Phys. Rev. E*, **74**, 061709 (2006).

[8] N. M. Shtykov, S. P. Palto and B. A. Umanskii, *J. Exp. Theor. Phys*. **117**, 349 (2013).

[9] V. A. Belyakov and S. V. Semenov, *J. Exp. Theor. Phys.* **109**, 687 (2009).

[10] N. M. Shtykov and S. P. Palto, *J. Exp. Theor. Phys.* **118**, 822 (2014).

[11] J. Lub, W. P. M. Nijssen, R. T. Wegh, I. De Francisco, M. P. Ezquerro and B. Malo, *Liq. Cryst.* **32**, 1031 (2005).

[12] S. P. Palto, L. M. Blinov, M. I. Barnik, V. V. Lazarev, B. A. Umanskii and N. M. Shtykov, *Crystallogr. Rep.* **56,** 622 (2011).

[13] S. P. Palto, N. M. Shtykov, M. I. Barnik and B. A. Umanskii, *Crystallogr. Rep.* **55**, 283 (2010).

[14] A. Yariv, *"Quantum electronics"*, Wiley (1989).

[15] A. Muñoz, M. E. Mc. Conney, T. Kosa, P. Luchette, L. Sukhomlinova, T. J. White, T. J. Bunning and B. Taheri, *Opt. Lett.* **37**, 2904 (2012).

CHAPTER IV

KINETIC BEHAVIOR OF LIGHT EMISSION IN CHOLESTERIC LIQUID CRYSTALS

4.1 Introduction

In order to get further insight on the nature of CLC lasers, in this chapter we are going to deal with some dynamical aspects of fluorescence and lasing.

In chapter 2 we presented a recently proposed model by Shtykov and Palto[1] for laser generation in CLCs. Such rate equations are useful for studying a great variety of laser characteristics. For example, chapter 3 was focused on the influence of the cavity thickness in the laser performance. Inter alia, these equations can be useful for studying luminescence lifetimes in CLC light emission. Up to now, rather few experimental results have been published on luminescence lifetimes and, in general, about the kinetics of light emission in photonic materials[2, 3, 4, 5, 6]. In this chapter, we present some studies in this respect by examining the response of a CLC laser to nanosecond optical pumping. The temporal profiles of the output pulses have been found to depend greatly on the pumping power, thus giving information about the dynamics of the fluorescence and laser emission. We will interpret the obtained results by means of the mentioned rate equations[1].

A molecule in the excited singlet (see Fig. 8 of chapter 3) can decay to the ground level by means of radiative or nonradiative processes. The decay rate, k, of the excited singlet can be written as the sum of the decay rates of radiative and nonradiative processes:

$$k = k_{rad} + k_{nonrad} = \frac{1}{\tau_{rad}} + \frac{1}{\tau_{nonrad}}, \qquad (4.1)$$

where τ_{rad} and τ_{nonrad} are the radiative and non radiative decay times respectively. Thus, the fluorescence lifetime of the excited singlet has the following form:

$$\tau_f = \frac{1}{k} = \frac{1}{k_{rad} + k_{nonrad}} = \frac{\tau_{rad}\tau_{nonrad}}{\tau_{rad} + \tau_{nonrad}}, \tag{4.2}$$

As we showed in detail in chapter 2, the emission intensities of a dye are substantially modified if the dye is dissolved in a CLC compared to the case of an isotropic solvent. This can be understood by means of Fermi's golden rule (see Eq. (2.49)). Such rule shows how the rate of fluorescence emission is directly proportional to the DOS. Therefore a modification in the DOS results in a change in the fluorescence emission spectrum. In principle, it could be thought that this alteration may also affect to the fluorescence lifetime of the dye. However, some authors have observed that fluorescence lifetimes do not suffer appreciable alteration[6]. This lack of modification occurs regardless of the light polarization, sample thickness and wavelength, all of which affect the DOS and, in principle, should have a counterpart in the lifetimes. The mentioned authors could not explain why fluorescence times remain unaltered and to the best of our knowledge this controversial point remains unsolved. At the end of this chapter, we will also go back to this point.

4.2 Experimental procedure and results

The materials used for the experiments in this chapter were the same as those of point (2.5.1) of this dissertation. The proportions in the mixture were also the same. The sample cell was made of two glass plates separated a distance $L =$ 10 μm. The material was in the Cano geometry, i.e. with the helix axis perpendicular to the substrates in the CLC phase.

The photonic properties of the material were studied in section (2.5.1). The band gap appears in the range 559-634 nm of wavelength. The fluorescence spectra and lasing emission (at a wavelength of 634 nm) are shown in Figs. 12, 14, 15,

and 16 of chapter 2. As expected, lasing consisted on circularly polarized light with the same handedness as the CLC helix (right handed).

The pumping source was a Nd:YAG laser operating at the second-harmonic frequency (wavelength 532 nm). Pulses of 14 ns and with a repetition rate of 5 Hz were used. The pumping light was focused on the sample using a lens of 20 cm of focal length; this resulted in a spot size of 40 μm of diameter at the sample. The experimental setup is depicted in Fig. 1.

The angle of incidence of the pumping light was of 45^0, and the light was circularly polarized with the handedness opposite to the CLC helix. All the measurements were made at room temperature. For the dynamical measurements the light emitted around the cell normal was collected using a lens of 50 mm of diameter that focused the light on a fast photodiode (rise and fall times of 1 ns). A filter centered at 633 nm with a narrow band pass (FWHM 4 nm) was used to avoid the averaging effect of the lifetime in a wider wavelength range. As in section (2.5.1), it was checked that the emitted light was circularly polarized with the same handedness as that of the helix. The photodiode was connected to an oscilloscope. To eliminate artificial pulse broadening during pulse averaging (due to jitter effects) single shot data were taken.

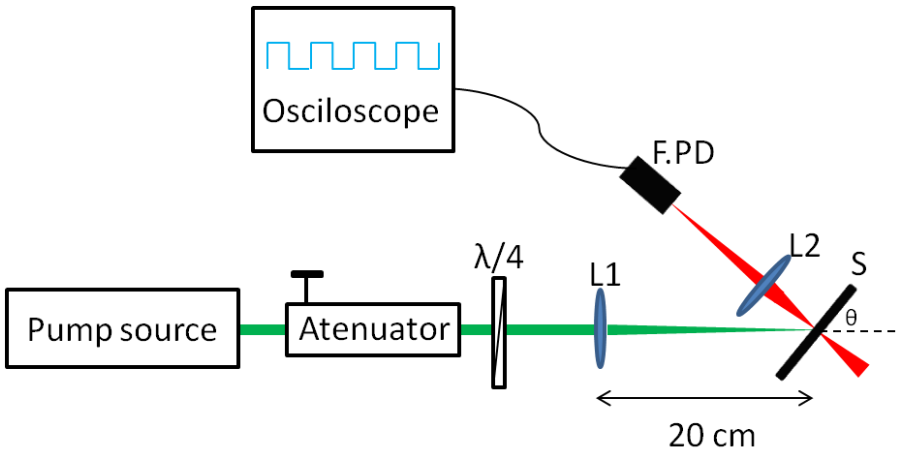

Fig. 1. Experimental setup: L1 and L2 are lens, S is the sample, θ is the angle of incidence, F.PD is the abbreviation for fast photodiode.

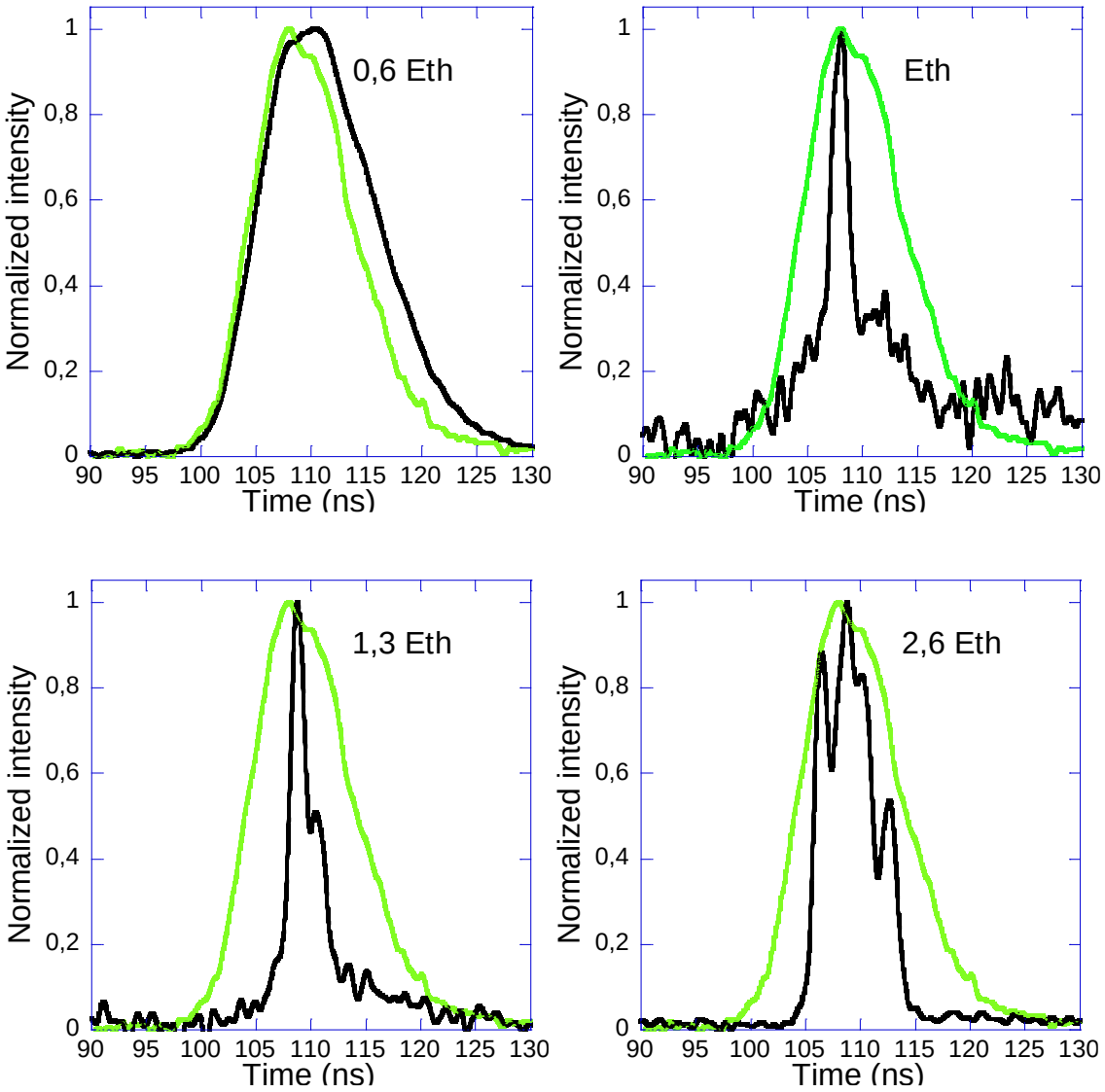

Fig. 2. Normalized temporal profiles of laser emission pulses for different pumping energies. To facilitate a comparison we present the profile corresponding to pump in all graphs (green line).

Fig. 2 shows some representative pulses for different pumping powers. Well below the threshold intensity, the laser pulse shows a temporal profile similar to that of the pumping laser. At the threshold, the narrowing of the pulse is limited by the detector time resolution (2 ns). When lasing starts, the pulse shape becomes more irregular, and the output consists of individual bursts of about 2 ns with a fluctuating pattern formation. As a consequence the width of the emitted pulses shows again a slight increasing trend. Figure 3 shows the pulse duration as a function of the pumping pulse energy.

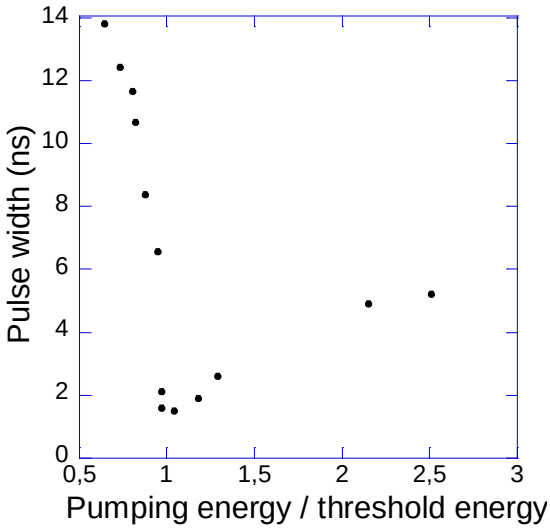

Fig. 3. Experimental duration of the light emission pulses as a function of the pumping pulse energy. The pumping energy is given in units of the laser threshold energy. The experimental threshold was 1.9 μJ per pulse.

4.3 Numerical simulations and discussion

Parameter	Value
P (μm)	0.367
n	1.6
α	0.125
P_{31} (s^{-1}), P_{23} (s^{-1})	10^4, $5x10^7$
τ_f (ns), τ_r (ns)	1.2, 2.4
K	10^{-7}
σ_e (cm^2), σ_a (cm^2)	$0.4x10^{-16}$, $0.4x10^{-16}$
β (cm^{-1})	10^2
S (μm^2)	$1.26x10^3$
L(μm)	10
N (cm^{-3})	$2x10^{19}$

Table 1. Parameters used for the simulations. The pumping and laser emission wavelengths were 532 and 634 nm respectively.

In order to interpret our results we will come back to Shytkov and Palto's model[1]. Remember that such equations were presented in chapter 2 and used in

chapter 3 (see Eqs. (2.56) or (3.16)). The parameters used in the simulation are given in Table 1, where it is kept the same notation for τ_f and τ_r as that of the chapter 3. Fig. 4 shows the pulse behavior of emitted light under different pumping regimes. Pulses in Fig. 4 are normalized. At low pumping, luminescence duration is close to that of the excitation source. As pumping increases the width of the fluorescence pulses decreases. At the threshold, the emission is extremely narrow, clearly below 1 ns. For powers above the threshold, relaxation oscillations (spiking) take place (Fig. 4), with an increasing number of spikes as the pumping level is raised.

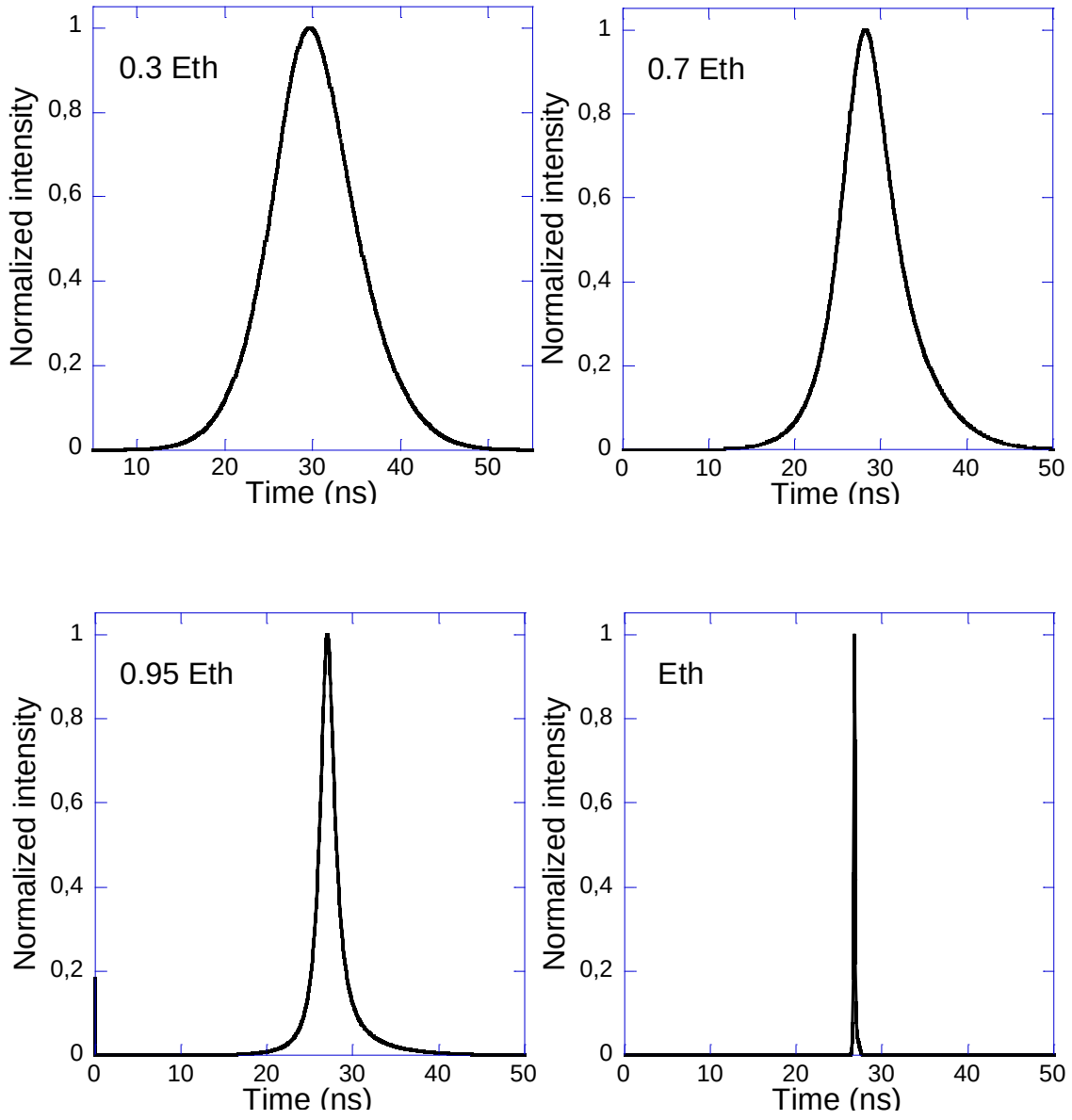

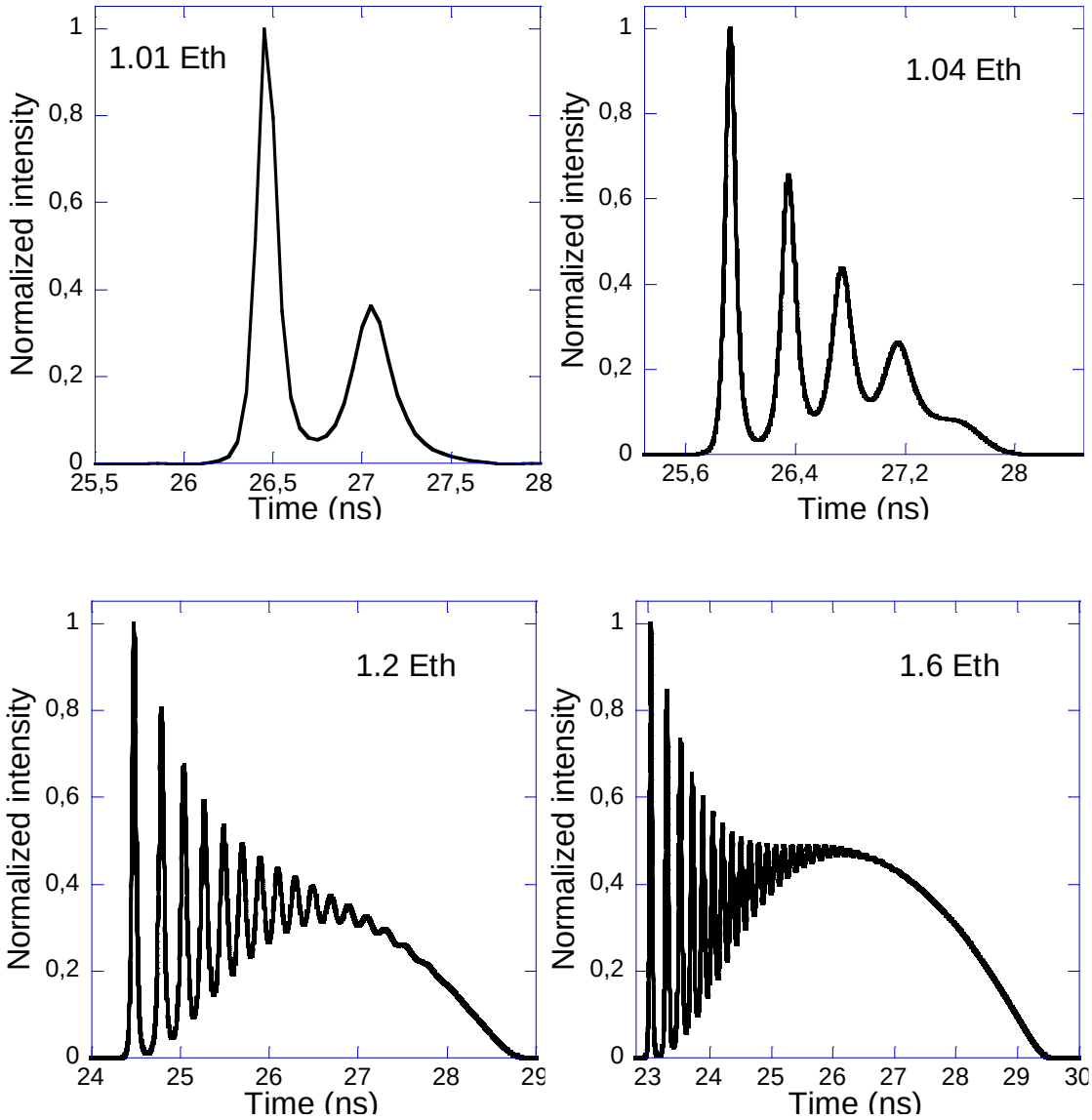

Fig. 4. Calculated temporal profiles of laser emission pulses for different pumping energies. The intensities have been normalized.

In chapter 3 it was shown that above the threshold, the inversion population, n_2^{th}, is kept constant, even under high pumping regime. Strictly speaking this is not true. A large-scale plot of $n_2(t)$ (see Fig. 5 (a)) shows that the excited singlet population describes a series of damped oscillations around n_2^{th}. Simulations show that the higher the pumping energy, the greater the number of damped oscillations but also the longer the time during which n_2^{th} is maintained.

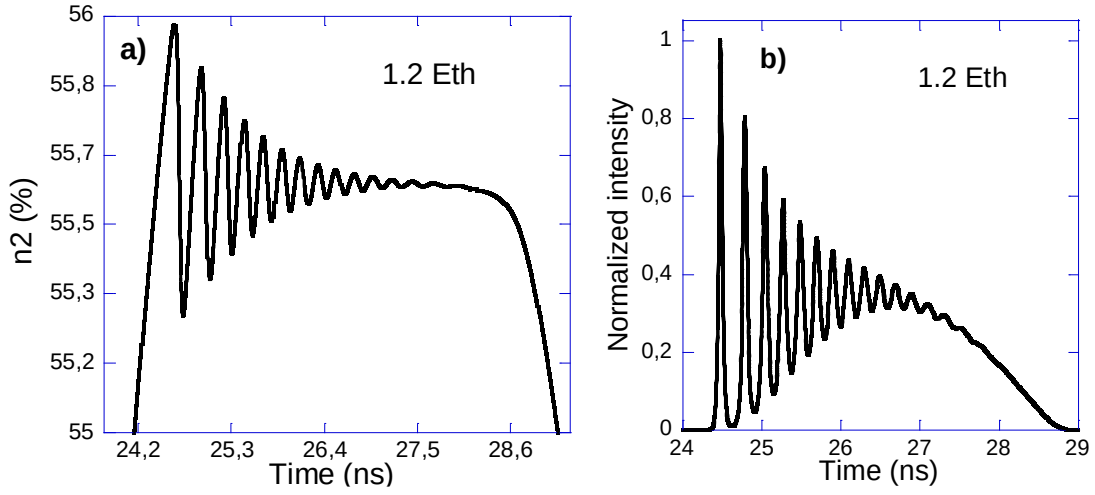

Fig. 5. (a) Simulated temporal profile of n_2 and (b) laser emission. The oscillations in $n_2(t)$ are on the origin of the lasing spikes.

Pulse profiles are related to the population of the excited singlet. Well under the threshold, $n_2(t)$ is far away from its threshold value. Besides, $n_2(t)$ exhibits a temporal profile similar to that of the pumping pulse since fluorescence time is clearly shorter than the pulse duration. Under such pumping regime, spontaneous emission is more important than stimulated emission. Due to this fact there is only fluorescence and this fluorescence exhibits a temporal profile similar to that of the pumping pulse. As the pumping power is raised, the stimulated emission increases importance and thus $n_2(t)$ is de-excited quicker. This fact results in a narrowing of the emitted fluorescence pulses (see Fig. 4). At the threshold, n_2^{th} value is achieved (see Fig. 11 of chapter 3). At such point lasing occurs, thus the excited singlet is quickly de-excited through stimulated emission. Due to this fact, a minimum of less than 1 ns width is reached at the threshold.

The spiking phenomenon above the threshold is well known in solid-state lasers[7] and is related to the described temporal profile of $n_2(t)$. Once n_2^{th} is reached, there is a short period of time characteristic of the stimulated emission ($\frac{h\nu_e}{\sigma_e I_e}$, see section (2.7) of this dissertation), before any laser emission occurs, and

$n_2(t)$ continues growing. However, when lasing begins the emitted photons grow very quickly and as a consequence $n_2(t)$ decreases even slightly below the threshold value. Therefore, stimulated emission is strongly decreased and the process starts again. This is the origin of the damped oscillations of $n_2(t)$ and consequently of the intensity of laser emission known as spike. Despite that solutions of laser rate equations predict a train of spikes as those shown in Figs. 4 and 5 (b), in practice, mechanical and thermal disturbances act to continually re-excite the spiking behavior, which often occurs in an unpredictable-fashion. In our experimental results, when the pumping energy is well above the threshold, we observe this phenomenon which gives rise to output fluctuations (see Fig. 2).

In general, theoretical predictions are in good agreement with the experimental results, at least qualitatively (Fig. 2 and Fig. 3). In Fig. 6 we present the widths of the emitted pulses for both experimental and simulated results.

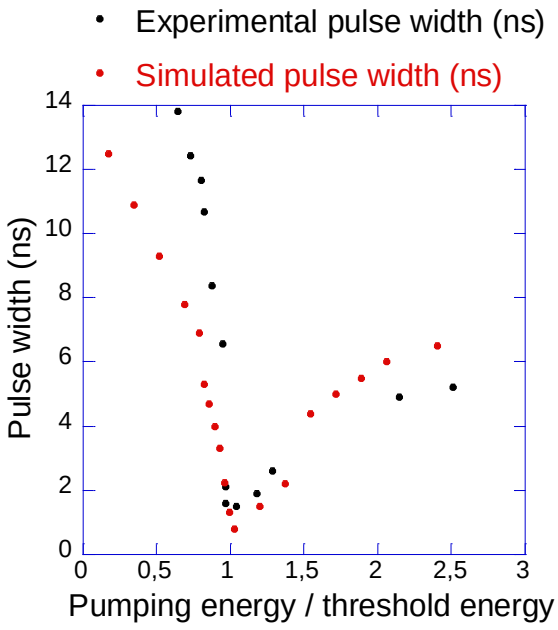

Fig. 6. Experimental (black dots) and simulated (red dots) duration of the light emission pulses as a function of the pumping pulse energy. The pumping energy is given in units of the laser threshold energy (1.9 μJ per pulse).

4.4 Fluorescence lifetimes

Now it is interesting to examine the issue of the fluoresce lifetime of a dye dissolved in a CLC. As we showed in chapter 2, the fluorescence spectrum of a dye inside a CLC is deeply modified with respect to the case of an isotropic solvent. However, as has been mentioned above, it has been experimentally shown[6] that the fluorescence lifetime of the dye is essentially unaltered by the CLC photonic structure. The question that now arises is whether the theoretical frame of Eqs. (2.56) can properly account for these phenomena.

First of all, let's consider the first equation of system (2.53) where $N_1 = N - N_2 - N_3$

$$\frac{dn_2(t)}{dt} = \frac{\sigma_a}{h\nu_a L}\left[\int_0^L N_1(z,t) I_a(z,t) dz\right] - n_2(t)\left(\frac{\sigma_e I_e(t)}{h\nu_e} + \frac{1}{\tau_f} + P_{23}\right). \quad (4.3)$$

Let us assume that the sample is illuminated with short pulses of low energy. Under these conditions, a small population n_{20} is generated in the sample. Because we are interested in the decay process, we must focus on the negative part of Eq. (4.3). So

$$\frac{dn_2(t)}{dt} = -n_2(t)\left(\frac{\sigma_e I_e(t)}{h\nu_e} + \frac{1}{\tau_f} + P_{23}\right). \quad (4.4)$$

The first term in the right side of Eq. (4.4) can be neglected because in the case of fluorescence $I_e(t)$ is very small, and P_{23} can also be neglected with respect to $1/\tau_f$ (see Table 1). So, Eq. (4.4) can be rewritten as

$$\frac{dn_2(t)}{dt} = \frac{-n_2(t)}{\tau_f}\ , \quad (4.5)$$

which results in a decay expression:

$$n_2(t) = n_{20}\exp\left[\frac{-t}{\tau_f}\right]. \tag{4.6}$$

This de-excitation gives rise to light emission. For calculating its power we introduce this result in the third of Eqs. (2.56). Then

$$\frac{dP_e(t)}{dt} = \frac{c}{n}\left(k\frac{h\nu_e S}{\tau_r}\right)n_{20}\exp\left[\frac{-t}{\tau_f}\right] - \frac{P_e(t)}{\tau_c}. \tag{4.7}$$

Notice that for this result we have eliminated $P_e(t)$, inside the brackets (third equation of system (2.56)), because in the case of fluorescence, emission is very low. If for the initial time we take $P_e(0) = 0$, Eq. (4.7) has an analytical solution given by:

$$P_e(t) = \frac{h\nu_e Skc}{n}n_{20}\frac{\tau_c}{\tau_f - \tau_c}\frac{\tau_f}{\tau_r}\left(\exp\left[\frac{-t}{\tau_f}\right] - \exp\left[\frac{-t}{\tau_c}\right]\right). \tag{4.8}$$

Besides, if $\tau_f \gg \tau_c$, as is the case in practical situations, Eq. (4.8) simplifies to

$$P_e(t) = \frac{h\nu_e Skc}{n}n_{20}\frac{\tau_c}{\tau_r}\exp\left[\frac{-t}{\tau_f}\right]. \tag{4.9}$$

Finally, using Eq. (3.19), the light power outside the cavity is

$$P_{out}(t) = h\nu_e SkLn_{20}\frac{\exp\left[\frac{-t}{\tau_f}\right]}{\tau_r}. \tag{4.10}$$

Thus, as expected, the fluorescence spectrum of the doped dye is significantly modified in the CLC sample because P_{out} is proportional to $1/\tau_r$, i.e. according to Fermi's golden rule, to the DOS, which is highly modified in the photonic structure of the CLC. However, the time evolution of the detected light must be a simple exponential with characteristic fluorescence time τ_f. Experimentally it

is found that τ_f is not substantially influenced by the CLC[6]. Therefore the sum of the radiative and nonradiative de-excitation rates (see Eqs. (4.1) and (4.2)) must remain unaltered. This is, according to Eq. (4.1):

$$k_{rad} + k_{nonrad} = constant\ . \tag{4.11}$$

In other words, if an excited molecule in a photonic material has an enhanced radiative de-excitation rate, it must show a reduced nonradiative de-excitation probability and vice versa.

It must be commented that although the photonic material can, in principle, influence the emission kinetics through τ_c, (see Eq. (4.8)), deviations from the simple exponential law (Eq. (4.9)) are unlikely. This would require cavity lifetimes τ_c comparable to fluorescence lifetimes τ_f. If we suppose $\tau_f = 1$ ns, this condition implies a coefficient of distributed losses as small as $\beta \approx 0.05$ cm^{-1} even if the CLC samples are extremely thick (see Eq. (2.50)). The light-scattering coefficient of a nematic is already orders of magnitude higher than this value[8, 9, 10].

4.5 Conclusions

In summary, we have studied some kinetic aspects of light emission in dye-doped CLC's by measuring the shape of the emitted pulses as a function of the pump energy. Well below the threshold the pulse's width is similar to that of the pump source (14 ns). As the pumping level increases, the emitted pulses become narrower until a minimum is reached at the lasing threshold. In our case the minimum's width was limited by ours photodiode time resolution. Above the threshold the temporal profiles suggest the appearance of relaxation oscillations as in the case of solid state lasers. The results can be accounted for

within the model of coupled rate equations shown in chapters 2 and 3, which incorporates the CLC peculiarities simply through the radiation dwelling time of the cavity τ_c. Within this model, an alteration of the fluorescence spectrum of the dye is predicted if it is dissolved in a CLC structure. On the other hand, the fluorescence lifetime is still τ_f because usually $\tau_f \gg \tau_c$. According to the experiments of other authors, τ_f is not substantially altered by the CLC cavity, which implies that the corresponding modifications of the radiative and nonradiative de-excitation rates must be opposite to each other.

[1] N. M. Shtykov and S. P. Palto, *J. Exp. Theor. Phys.* **118**, 822 (2014).

[2] W. Cao, P. Palffy-Muhoray, B. Taheri, A. Marino and G. Abbate, *Mol. Cryst. Liq. Cryst.* **429**, 101 (2005).

[3] E. P. Petrov, V. N. Bogomolov, I. I. Kalosha and S. V. Gaponenko, *Phys. Rev. Lett.* **81**, 77 (1998).

[4] Y. Zhong, Z. Yue, G. K. L. Wong, Y. Y. Xi, Y. F. Hsu, A. B. Djurišić, J. Dong, W. Chen and K. S. Wong, *Appl. Phys. Lett.* **97**, 191102 (2010).

[5] J. Zhou, Y. Zhou, S. Buddhudu, S. L. Ng, Y. L. Lam and C. H. Kam, *Appl. Phys. Lett.* **76**, 3513 (2000).

[6] W. Cao, *"Fluorescence and lasing in liquid crystalline bandgap materials"*, PhD Thesis, Kent State University, (2005).

[7] W. Koechner, *"Solid-state laser engineering"*, Springer (1988).

[8] L. M. Blinov, *JETP Lett*. **88**, 160 (2008).

[9] S. T. Wu and K. C. Lim, *Appl. Opt.* **26**, 1722 (1987).

[10] J. Etxebarria, J. Ortega, C. L. Folcia, G. Sanz-Enguita and I. Aramburu, *Opt. Lett.* **40**, 1262 (2015).

CHAPTER V

CHOLESTERIC LIQUID CRYSTAL LASERS DEGRADATION

5.1 Introduction

Part of the recent interest in CLC lasers originates from different promising technological features. For example, wavelength tunability, low threshold lasing, high efficiency of energy conversion and ease of construction.

However, one of the technical problems with this type of lasers is that they degrade and stop lasing in relatively short periods of time. This fact seriously limits possible practical and commercial applications of CLC lasers. The main reason of this problem is the gradual degradation of the dye molecules and the structure deterioration, caused by a powerful optical pumping. On the one hand, such deterioration implies an effective reduction of the dye population. On the other hand, it increases the coefficient of distributed losses.

The process by which the above mentioned deterioration occurs has given rise to various discussions; it has been attributed to dye bleaching, thermal or density effects[1] and, to the director reorientation of the LC molecules due to a light-induced torque[2]. However, up to now, there is no consensus about what mechanism is responsible for this deterioration.

In chapter 3 we studied the performance of the CLC lasers depending on different parameters. This is very interesting since a good performance of the CLC laser would allow us to optimize the fabrication of these devices. Inter alia, this would allow using simpler and less powerful pumping sources. However, it is clear that a detailed understanding of the origins of the CLC laser degradation is completely necessary to obtain commercially acceptable devices. This is why in this last section we will focus in this problem. In this sense, we will present some results about the dynamics of CLC laser deterioration with the aim of throwing some light on the mechanisms that produce such degradation.

5.2 Materials

The materials used for the experiments in this chapter were the same as those of section (2.5.1). The proportions in the mixture were also the same. The sample cell was made of two glass plates separated a distance $L = 9.9$ μm. The material was in the Cano geometry with the helix axis perpendicular to the substrates in the CLC phase and the band gap was between 559-634 nm.

The pumping source and the experimental setup were also the same as those of section (2.5.1), see Fig. 1. In this case the pumping repetition rate was varied between 5 and 100 Hz.

All the measurements were carried out at the temperature of 22 ºC.

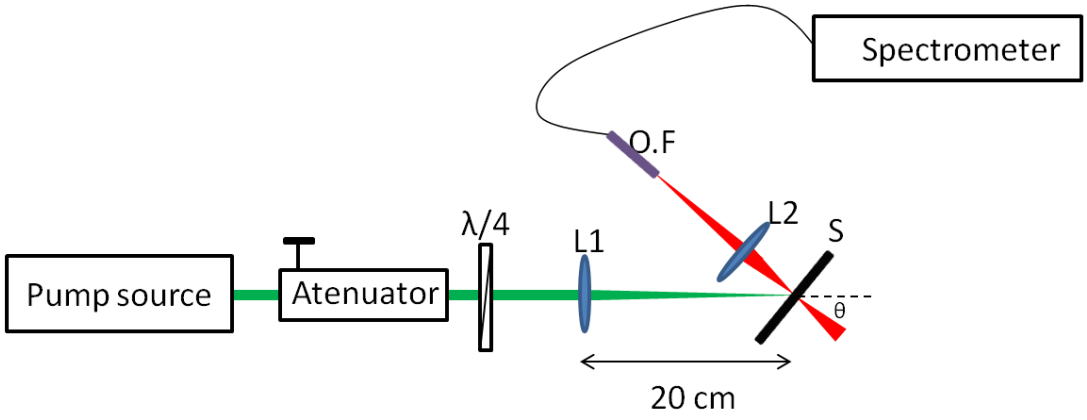

Fig. 1. Experimental setup. L1 and L2 are lens 1 and 2 respectively, S is the sample, θ is the angle of incidence, and O.F is the abbreviation for optical fiber.

5.3 Laser degradation

Fig. 2 shows the laser emission power versus pumping energy per pulse. For this measurement, L2 in Fig. 1 was removed so that most of the fluorescence was not detected. The data were obtained for a repetition rate of 5 Hz. Similar results took place for smaller repetition rates, but larger rates produce gradual

laser deterioration. The degradation was evident for frequencies above 25 Hz for pumping powers about twice that of the threshold. Neither appreciable spectral broadening of the laser line nor significant shift of the laser wavelength was observed during the whole process. As a representative example, Fig. 3 shows the laser output power for pumping pulses of 9.5 μJ and a repetition rate of 100 Hz. The laser intensity decreases monotonically with time, and no equilibrium is reached until a complete disappearance of the laser light. This figure fits to a simple exponential, with a characteristic time of 2 minutes. Using higher pumping powers, analogue results were obtained, the only difference was the degradation time: the higher the pumping the quicker the degradation.

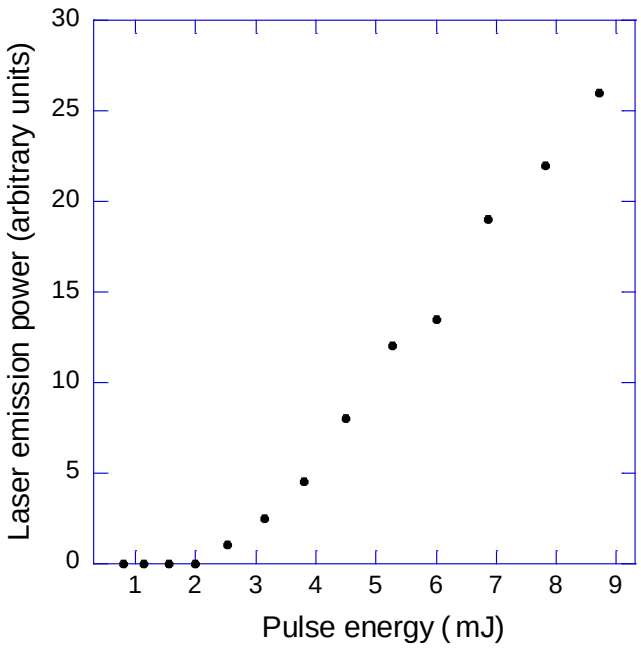

Fig. 2. Laser output power as a function of the incident pumping energy per pulse for a repetition rate of 5 Hz.

Interestingly, the damage is reversible if the pumping energy is not too high. However, in most cases, the time for recovery is relatively long. For example, after the decay process shown in Fig. 3, the material takes about 30 minutes in the darkness to recover its previous performance. Even longer times are needed if the CLC continues being excited for still longer periods after the lasing disappearance. The order of magnitude of these times excludes the optical

torque on the CLC molecules as a factor responsible for the reduction of the emission efficiency. In that case, much shorter recovery times would be expected[2]. If even larger pumping energies are used, irreversible degradation of the material is produced, and the recovery is only partial even waiting for days. In extreme cases, an obvious burning can be provoked at the position of the light spot.

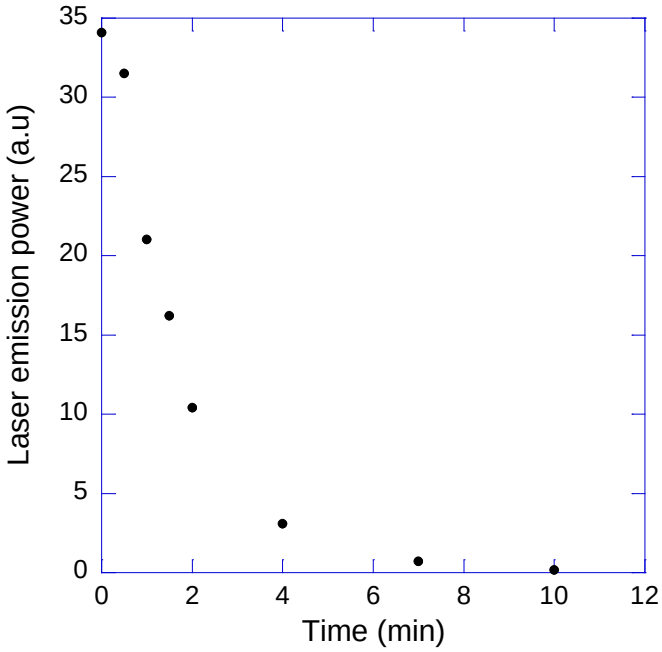

Fig.3. Time evolution of the laser output power for incident pumping pulses of 9.5 μJ and a repetition rate of 100 Hz.

Fig. 4 (a) shows the evolution of the emission spectrum while the material is subjected to pulses of 9.5 μJ of energy at 100 Hz. The emitted light was collected using the lens L2 (see Fig. 1). In this way, the fluorescence spectrum is clearly visible simultaneously with lasing. The line at 532 nm corresponds to the pumping laser. Fluorescence light inside the gap is essentially circularly polarized, with a handedness opposite to that of the laser light. On the contrary, fringes at the edges outside the gap ($\lambda < 559$ or $\lambda > 634$ nm) are due to the additional contribution of fluorescence light with the same polarization as the laser emission; this has been previously justified in section (2.5.1) (see Figs. (14-18). Together with the laser decay, a general decrease of the fluorescence

intensity is observed with time. The rate of decline is the same for both polarizations and for all wavelengths (with the exception of the laser light, which decays much faster). Fig. 4 (b) shows that the time dependence of the fluorescence intensity can be modeled by a simple exponential plus a constant, with a characteristic time that depends on the pumping intensity and pulse repetition rate; in this case the characteristic time is of 5.7 minutes. This decrease is due to the dye-bleaching phenomenon, which is well known in organic dyes, and can be reversible or irreversible depending on the magnitude and rate of the excitation. In last instance, bleaching is due to the so-called intersystem crossing between the excited singlet and ground triplet state of the molecule. This process removes molecules from the laser channel and transforms them into heat sources, which convert most of the absorbed light into thermal energy. Consequently, there is a high increase of the proportion of non-radiative de-excitation processes in the material and, in some cases; the molecules can even suffer an irreversible breakdown.

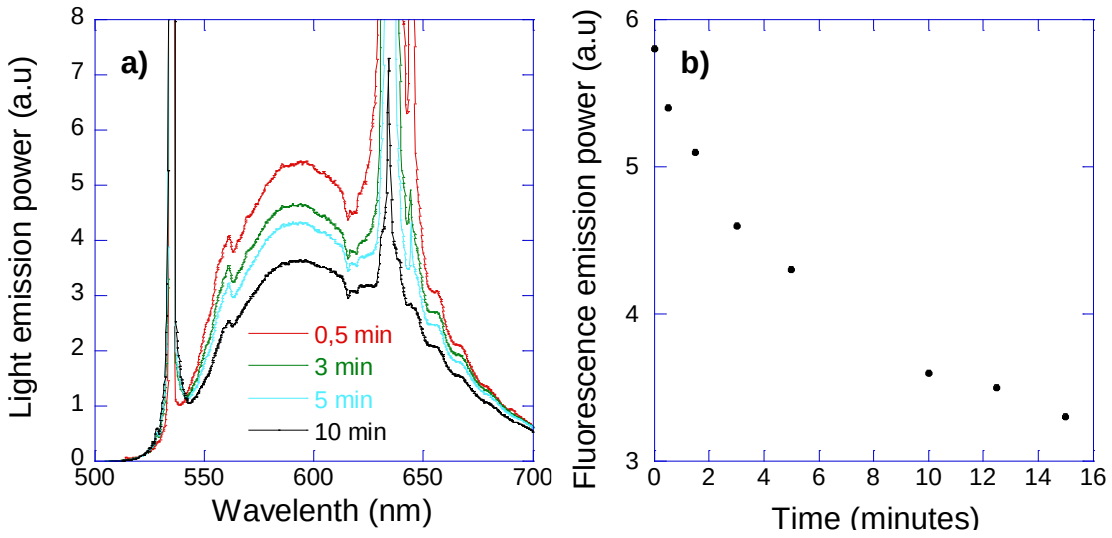

Fig. 4. Time evolution of the emission spectrum (a) and of the fluorescence output power (b). Pumping pulses of 9.5 μJ and 100 Hz were used in both cases.

A possible local temperature rise of the material, caused by the optical pumping, is not enough to explain the observations either, because temperature variations would imply a shift in the laser wavelength during the degradation

(due to the temperature dependence of the helical pitch) and much shorter recovery times. However, according to Fig. 4 (a), it is clear that neither appreciable spectral broadening of the laser line nor significant shift of the laser wavelength was observed during the whole process.

A consequence of dye bleaching is that the effective dye concentration on the pumped volume decreases with time during laser operation. In optimized CLC lasers, a relatively small decrease of the dye concentration would affect in a limited extent to the laser performance. Therefore, the laser emission should only show a small reduction (similar to that displayed by the fluorescence) as a function of time. For not very thick samples, as is our case, the importance of this effect depends approximately on the value of the product $N\sigma_e$, being N the number of dye molecules per unit volume and σ_e the cross section of stimulated emission per dye molecule. Such dependence can be seen by taking the first order expansion in the exponential term of the denominator of Eq. (3.32):

$$E_{th} = 2h\nu_a SL\left(1 + 0.53\Delta\tau_p\left(P_{23} + 1/\tau_f\right)\right)\frac{n}{c\tau_c\sigma_a L}\frac{1}{\sigma_e n_1^{th}}, \qquad (5.1)$$

where $n_1^{th} = N - n_2^{th} - n_3^{th}$, $n_2^{th} = \frac{n}{c\sigma_e\tau_c}$, $n_3^{th} \approx 0.53\frac{n}{c\sigma_e\tau_c}P_{23}\Delta\tau_p$ and none of the other parameters depend on N.

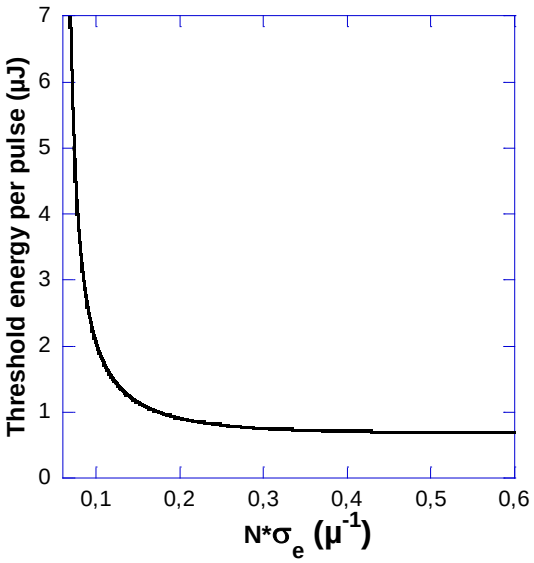

Fig. 5. Threshold energy per pulse of the pumping source *vs.* $N\sigma_e$.

Fig. 5 represents the threshold energy per pulse as a function of $N\sigma_e$. The results have been obtained by using Eq. (5.1). As can be seen, for high dye concentrations or high σ_e values, a moderate decrease of N hardly affects the laser performance. However, for $N\sigma_e$ below $\approx 0.15\ \mu^{-1}$ a small diminution in this quantity affects dramatically to the laser performance. In our cases $N\sigma_e \approx 0.1\ \mu^{-1}$ and therefore our laser is very sensitive to a small reduction of N. In fact, the fall of the laser power, experimentally observed, can be compared to the values calculated by using the rate equations (3.16). Fig. 6 gathers the obtained results. As can be seen a good agreement for both experimental and calculated values of the laser power has been found.

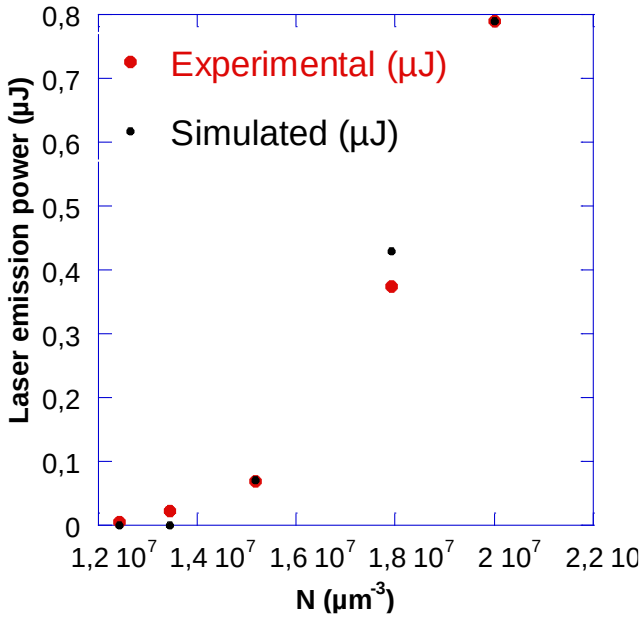

Fig. 6. Laser output power *vs*. N.

Interestingly, we also observed a strong correlation between lasing emission decay and sample light scattering. So, here we point to light scattering as another potential cause of laser degradation. As a next step we will also focus on this phenomenon, and we will show some results about the relation between light scattering and laser degradation. To characterize the correlation between laser degradation and light scattering we removed the lens L2 in our setup (see

Fig. 1). The measurements were carried out by collecting the light emitted by the sample along the substrate normal with an optical fiber placed at about 6 cm from the sample. The light spectrum consists of two wavelengths, one at 634 nm (the CLC laser line) and a second one at 532 nm, which corresponds to the light scattered at the pumping wavelength. Starting from a fresh, previously unexposed area of the sample, an efficient laser emission is initially found together with a small amount of scattered light. Subsequently a prominent increase of the light at 532 nm occurs while the lasing decays (see Fig. 7). Typically, the increase in the amount of scattered radiation is about one order of magnitude during the time that the laser takes to wipe out completely. Qualitatively the same behavior is always repeated on moving the sample to a new previously unexposed area.

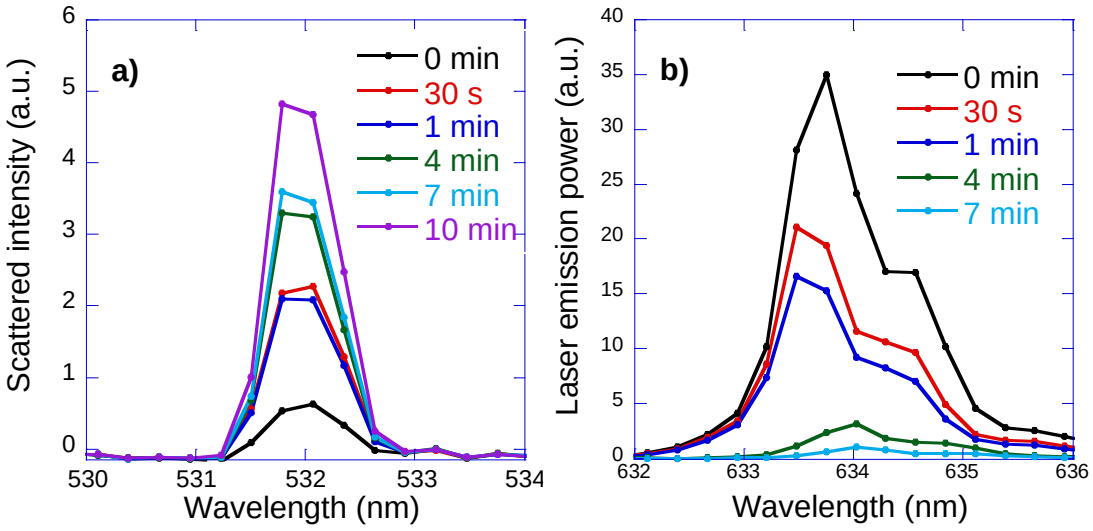

Fig. 7. Time evolution of the light intensity scattered by the sample (a) and laser emission power (b) as the sample is subjected to 532 nm pump pulses of 9.5 μJ at 100 Hz. In Fig. 7 (b), the curve corresponding to 10 minutes of exposure has been omitted due to the fact that after 10 minutes the signal was not appreciable.

Scattering effects represent an increase of losses, which must contribute to enlarge the threshold power of the laser. In this regard, according to Refs. 3 and 4, the threshold gain coefficient can be expressed as:

$$\gamma_{th} = \frac{n}{c\tau_c} = \beta + \frac{4P^2}{\alpha^2 L^3}\,, \tag{5.2}$$

where c is the speed of light in vacuum, n is the mean refractive index and τ_c is the radiation dwelling time of an emitted photon in the CLC layer. β is the coefficient of distributed losses, which takes into account all losses of absorption and scattering of light by the CLC, L is the thickness of the sample, P is the helical pitch and α is the anisotropy parameter.

The smallest value for the threshold gain coefficient results

$$\gamma_{th}^{min} \approx \frac{4P^2}{\alpha^2 L^3}\,, \tag{5.3}$$

which is obtained by taking $\beta = 0$ in Eq. (5.2). In the present sample, $L = 9.9$ μm, $P = 0.367$ μm and $\alpha = 0.125$, so we get $\gamma_{th}^{min} \approx 350$ cm^{-1}. On the other hand, the threshold power is proportional to the threshold gain coefficient[3] (see Eq (3.13)). Therefore, in order to have a rise of the threshold power of the order of magnitude of the threshold power itself in a fresh sample, we should increase the distributed losses in an amount of the same order of magnitude, i.e., $\beta \approx 100$ cm^{-1}.

We speculate that the scattering could also contribute to the laser deterioration due to small imperfections generated in the sample as a result of thermal processes mentioned above. Heating by the pump beam can decompose the dye molecules or induce changes in the structure of the CLC at the neighborhood of the dye molecules at the illuminated spot. The local heating could make the CLC reach the clearing point, produce its chemical decomposition or even destroy the dye molecule itself. Every dye molecule could give rise potentially to a scattering center. If the size of the scatterers is small compared to the wavelength of the scattered light, the Rayleigh approximation can be used. In this case the scattering cross section can be written as[5]

$$\sigma = \frac{8\pi}{3}\left(\frac{2\pi n}{\lambda}\right)^4 a^6 \left(\frac{m^2-1}{m^2+2}\right)^2, \tag{5.4}$$

where a is the scatterer radius, and m the ratio between the refractive index of the scatterer and the surrounding medium. The β coefficient is simply $\beta = N_s\sigma$, where N_s is the number of scattering centers per unit volume. Taking $m = 1.5/1.7 = 0.88$ (the ratio between the ordinary and extraordinary refractive indices of the CLC), we obtain $\sigma = 3.5\ 10^{-17}$ cm^2 for $a = 10$ nm. We assume N_s equal to the density of dye molecules, which are bleached by the pump beam. In the present case, due to the decay in fluorescence shown in Fig. 4, N_s is about 20% of the total number of dye molecules when the laser stops working. So, we obtain $N_s \approx 4\ 10^{18}$ cm^{-3} and $\beta \approx 140$ cm^{-1}. So, using the Rayleigh approximation and making some reasonable assumptions we see that a bleaching of about 20% of the molecules could result in a hypothetical increase in the laser threshold of about one order of magnitude. Therefore, an increase in β due to light scattering should be taken into account since could also be in the origin of the deterioration of the laser performance.

We finish this chapter with some words about the mechanisms for laser recovery when the sample is kept in the darkness. Depending on the optical damage received by the CLC, the laser recovery can be total or partial. In the best case, when the LC molecules affected by the local heating have just undergone a transition to the isotropic phase and there is no chemical decomposition, the thermal degradation is reversible, and the time for recovery should be fast. Evidently, if there are dye molecules (or LC molecules) that have decomposed, a total recuperation can only be reached through much slower processes involving molecular diffusion that replace the deteriorated molecules by new ones at the spot position. The larger the optical damage the more incomplete and the slower the laser recovery. If the pumping energies are even

higher, the degradation can be irreversible. All these regimes are experimentally observed.

5.4 Conclusion

CLC lasers suffer an important drawback that limits in a serious manner their operation; this is laser degradation. The consequences of such degradation are on the one hand, that the effective dye concentration decreases. On the other hand, a clear increase of the scattered light by the CLC sample has been found. The scattering represents a growth of the coefficient of distributed losses. In our particular case we have shown that laser degradation is explained by a decrease in N. Nevertheless, for optimized lasers, a relatively high reduction of operative dye molecules, by itself, is still far from justifying an important laser decay. Since the origin of the problem of laser stability is the heating of the dye molecules, the performance of CLC lasers should highly improve with dyes showing low quantum yields to triplet states. In this respect, special fluorescent molecules with small triplet populations have recently permitted to achieve CW lasing with CLCs[6, 7].

Nevertheless, it is remarkable to say that at low pumping frequencies, for example about 5 Hz, and energies per pumping pulse of the same order of magnitude as the threshold, thermal degradation of the dye molecules is negligible. Actually, some of the samples used in this dissertation have lasted for months without showing a performance decrease.

[1] A. Varanytsia and P. Palffy-Muhoray, *Proc. SPIE*, **8828**, 88281F (2013).

[2] S. M. Morris, A. D. Ford, M. N. Pivnenko and H. J. Coles, *J. Opt. A*, **7**, 215 (2005).

[3] L. M. Blinov, *JETP Lett.* **90**, 166 (2009).

[4] V. A. Belyakov and S. V. Semenov, *J. Exp. Theor. Phys*. **109**, 687 (2009).

[5] A. J. Cox, A. J. De Weerd and J. Linden, *Am. J. Phys*. **70**, 620 (2002).

[6] H. A. Montejano, F. Amat-Guerti, A. Costela, I. García-Moreno, M. Liras and R. Sastre, *J. Photochem. Photobiol. A,* **181**, 142 (2006).

[7] A. Muñoz, M. E. McConney, T. Kosa, P. Luchette, L.Sukhomlinova, T. J. White, T. J. Bunning and B. Taheri, *Opt. Lett*. **37**, 2904 (2012).

CHAPTER VI

NONLINEAR OPTICS IN LCs

6.1 Introduction

Nonlinear optical (NLO) effects, mainly those of second and third-order, have found a wide range of applications in electro-optics, optoelectronics, photonics, and biomedical technologies as well. Today's benchmark NLO materials are actually, inorganic crystals (e.g. Li Nb O_3). However, organic NLO materials offer greater opportunities for developing potentially low-cost and high performance electronic and photonic devices because of their attractive features such as large and ultrafast responses, low drive voltages, facile fabrication and processability, and wide range of operating frequencies[1, 2, 3, 4, 5, 6, 7, 8, 9].

FLCs[10], as a special type of organic NLO materials, will become a compelling alternative to inorganic crystals and electrically poled organic glasses if large NLO strength is achieved[11, 12]. Since FLCs possess thermodynamically stable polar order, they are suitable for second harmonic generation (SHG). In addition the polar direction can be electrically controlled by switching between two ferroelectric states, enabling fabrication of more complex NLO devices.

In this chapter we are going to study ferroelectric LC compounds with interest for NLO applications. More specifically, we will focus on the characterization of the NLO properties of an azo-bridged trimer through second and third harmonic generation measurements (SHG and THG).

Firstly, we will introduce some concepts about NLO properties in general and next we will focus on the SHG.

Optical properties of materials are characterized by their dielectric susceptibility. When input-light intensities are low, the material response is dominated by linear effects and there exists a linear relation between the polarization (**P**) and the electric field (**E**). Nevertheless when impinging with intensities of the order of the fields binding electrons to nuclei (about

10^8-10^{10} V m^{-1}) the response of the material is nonlinear. These intensities are typically achieved by laser beams[13]. Due to this fact, second order optical effects were not experimentally demonstrated until the development of lasers in the decade of the 60's[14]. Under this high intensity condition, the polarization response can be expanded as follows:

$$P_i = \varepsilon_0 \chi_{i\,j} E_j + 2 d_{i\,j\,k} E_j E_k + 4 \chi_{i\,j\,k\,l} E_j E_k E_l + \cdots, \tag{6.1}$$

where P_i and E_i denote the polarization and electric field components respectively. ε_0 is the electric permittivity of vacuum and $\chi_{i\,j}$, $d_{i\,j\,k}$, $\chi_{i\,j\,k\,l}$ are the susceptibility tensors of first, second and third order respectively. Higher order terms have been suppressed in Eq. (6.1). Subscripts i, j, k and l denote the Cartesian coordinates and summation over repeated indices is assumed (Einstein's notation).

Susceptibility tensor	Nonlinear phenomena
$d^{(2)}(\omega_1 \pm \omega_2;\ \omega_1, \pm\omega_2)$	Frequency sum or difference.
$d^{(2)}(2\omega;\ \omega, \omega)$	Second harmonic generation (SHG).
$d^{(2)}(0;\ \omega, -\omega)$	Optical rectification.
$d^{(2)}(\omega;\ 0, \omega)$	Pockels effect.
$\chi^{(3)}(\omega_1 \pm \omega_2 \pm \omega_3;\ \omega_1, \pm\omega_2, \pm\omega_3)$	Frequency mixing.
$\chi^{(3)}(3\omega;\ \omega, \omega, \omega)$	Third harmonic generation (THG).
$\chi^{(3)}(\omega;\ \omega, \omega, -\omega)$	Optical Kerr effect.
$\chi^{(3)}(\omega;\ 0, 0, \omega)$	Electrooptical Kerr effect.
$\chi^{(3)}(2\omega;\ 0, \omega, \omega)$	SHG induced by an electric field.

Table1. Several nonlinear optical effects. Order is indicated by susceptibilities superscripts. In the susceptibilities, the first frequency (separated by ;) corresponds to the output field and the other frequencies denote the incident fields.

The second and third terms of the right side of the Eq. (6.1) describe different nonlinear optical phenomena. These phenomena depend on the involved frequencies of the input and output electric fields[15]. Table 1[15] shows some examples of different second and third order optical effects and how their respective susceptibilities depend on the involved frequencies. Nevertheless, in this dissertation, we will be mainly concerned with SHG.

Second order effects are driven by the third rank tensor $d_{i\,j\,k}$. Therefore, lack of inversion symmetry is a prerequisite for these phenomena to appear[16]. Evidently, polar structures fulfill this requirement. On the other hand, since third order effects are driven by the fourth rank tensor $\chi_{i\,j\,k\,l}$. Therefore, no symmetry prerequisites are required (see Eq. (6.1)).

6.2 Second harmonic generation (SHG)

Among second order nonlinear effects we will focus on SHG. This effect appears when the material combines two incident photons of frequency ω to give rise to one photon of frequency 2ω (see Fig. 1). This phenomenon is completely characterized by the second order susceptibility tensor $d_{i\,j\,k}$ corresponding to the frequencies involved in the process, i.e., ω and 2ω ($\mathbf{d}\,(2\omega;\omega,\omega)$).

By using Eq. (6.1) (see Appendix), the time independent part of the second order polarization term can be written as follows[16]:

$$P_i^{2\omega} = d_{ijk} E_j^{\omega} E_k^{\omega}\,, \tag{6.2}$$

where the term 2ω indicates the SH component, ω indicates the fundamental frequency and E_j^{ω} is the amplitude in the j direction of the fundamental beam and is time independent.

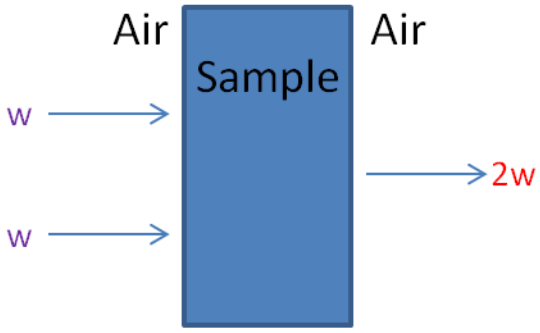

Fig. 1. Scheme of the SHG process.

The point group of the material determines the symmetry restrictions of the tensor **d**[16]. In the case of SHG no physical significance can be attached to the interchange of the subscripts j and k. Therefore, the **d** tensor can be expressed in contracted notation by replacing the two last subscripts by the following indices:

$$11 = 1, \qquad 22 = 2, \qquad 33 = 3,$$

$$23 = 32 = 4, \qquad 13 = 31 = 5 \text{ and } 12 = 21 = 6.$$

So Eq. (6.2) can be rewritten as

$$\begin{pmatrix} P_x^{2\omega} \\ P_y^{2\omega} \\ P_z^{2\omega} \end{pmatrix} = \begin{pmatrix} d_{11} & d_{12} & d_{13} & d_{14} & d_{15} & d_{16} \\ d_{21} & d_{22} & d_{23} & d_{24} & d_{25} & d_{26} \\ d_{31} & d_{32} & d_{33} & d_{34} & d_{35} & d_{36} \end{pmatrix} \begin{pmatrix} E_X^2 \\ E_Y^2 \\ E_Z^2 \\ 2E_Z E_Y \\ 2E_Z E_X \\ 2E_X E_Y \end{pmatrix}. \qquad (6.3)$$

It is worth mentioning that in the case of non-absorbing materials the susceptibility coefficients are also invariant under any permutation of their subscripts, the so-called Kleinman conditions[17].

Let now focus our attention on a form of Maxwell's equations which includes polarization, **P**, explicitly (we will assume no magnetization and no free charge):

$$\mathbf{D} = \varepsilon_o \mathbf{E} + \mathbf{P}\,, \tag{6.4}$$

$$\mathbf{B} = \mu_o \mathbf{H}\,, \tag{6.5}$$

$$\boldsymbol{\nabla} \mathrm{X} \mathbf{H} = \mathbf{J} + \frac{\partial \mathbf{D}}{\partial t}\,, \tag{6.6}$$

$$\boldsymbol{\nabla} \mathrm{X} \mathbf{E} = -\frac{\partial \mathbf{B}}{\partial t}\,, \tag{6.7}$$

$$\boldsymbol{\nabla}.\mathbf{D} = 0\,, \tag{6.8}$$

$$\boldsymbol{\nabla}.\mathbf{B} = 0\,, \tag{6.9}$$

where μ_o is the magnetic permeability of vacuum.

As we are interested in nonlinear optics, polarization will be explicitly expressed in terms of-linear (L) and nonlinear (NL) components, thus

$$\mathbf{P} = \mathbf{P}_L + \mathbf{P}_{NL} = \chi_L \varepsilon_o \mathbf{E} + \mathbf{P}_{\mathrm{NL}}\,, \tag{6.10}$$

where χ_L is the linear susceptibility tensor.

Introducing Eqs. (6.4) and (6.5) in Eqs. (6.6) and (6.7) and taking into account Eq. (6.10) we arrive to the following expression:

$$\nabla^2 \mathbf{E} = \mu_o \sigma \frac{\partial \mathbf{E}}{\partial t} + \mu_o \varepsilon \frac{\partial^2 \mathbf{E}}{\partial t^2} + \mu_o \frac{\partial^2 \mathbf{P}_{NL}}{\partial t^2}\,, \tag{6.11}$$

where $\varepsilon = \varepsilon_0(1 + \chi_L)$ is the electric permittivity and σ is the conductivity.

In order to solve Eq. (6.11) we will consider the particular case of three plane waves of frequencies $\omega 1$, $\omega 2$ and $\omega 3$ respectively, propagating along the z axis, given by

$$E_i^{\omega 1}(z,t) = \frac{1}{2}[E_{1i}(z)\exp[i(\omega 1t - K_1 z)] + c.c]\,, \tag{6.12}$$

$$E_k^{\omega 2}(z,t) = \frac{1}{2}[E_{2k}(z)\exp[i(\omega 2t - K_2 z)] + c.c]\,, \tag{6.13}$$

$$E_j^{\omega 3}(z,t) = \frac{1}{2}\left[E_{3j}(z)\exp[i(\omega 3t - K_3 z)] + c.c\right], \tag{6.14}$$

where the subscripts i, j and k denote the Cartesian coordinates and the subscripts 1, 2 and 3 refer to the frequency of the respective waves ($\omega 1$, $\omega 2$ or $\omega 3$). K_i denotes the wave vector corresponding to each frequency, t is the time and $c.c$ refers to the complex conjugate. In order to be the wave vectors well defined, Eqs. (6.12-14) must represent polarization eigenstates of the material.

If we introduce such expressions in Eq. (6.11) and assume that the field amplitude variation in z is small ($\frac{dE(z)}{dz}k_1 \gg \frac{d^2E(z)}{dz^2}$) and that $\partial/\partial x = \partial/\partial y = 0$, we arrive to the following set of differential equations:

$$\frac{dE_{1i}(z)}{dz} = -\frac{\sigma_1}{2}\sqrt{\frac{\mu_0}{\varepsilon_1}}E_{1i}(z) - \frac{\partial^2(P_{NL}^{\omega 1})_i}{\partial t^2}\mu_0\exp[-i(\omega 1t - K_1 z)]\frac{1}{iK_1}\,, \tag{6.15}$$

$$\frac{dE_{2k}(z)}{dz} = -\frac{\sigma_2}{2}\sqrt{\frac{\mu_0}{\varepsilon_2}}E_{2k}(z) - \frac{\partial^2(P_{NL}^{\omega 2})_k}{\partial t^2}\mu_0\exp[-i(\omega 2t - K_2 z)]\frac{1}{iK_2}\,, \tag{6.16}$$

$$\frac{dE_{3j}(z)}{dz} = -\frac{\sigma_3}{2}\sqrt{\frac{\mu_0}{\varepsilon_3}}E_{3j}(z) - \frac{\partial^2(P_{NL}^{\omega 3})_j}{\partial t^2}\mu_0\exp[-i(\omega 3t - K_3 z)]\frac{1}{iK_3}\,. \tag{6.17}$$

Assuming that the medium is lossless at $\omega 3$ ($\sigma_3 = 0$), under the non depleted approximation (this means that the fundamental intensity keeps constant within the material) and recalling Eq. (6.2), we obtain that

$$\frac{dE_{3j}(z)}{dz} = -i\omega\sqrt{\frac{\mu_0}{\varepsilon_3}}d_{jik}E_{1i}E_{1k}\exp[i\Delta Kz]\,, \tag{6.18}$$

where $\Delta K = K_3^j - K_1^i - K_1^k$ and the superscripts i, j and k indicate the polarization state of the beam.

Integrating along the materials thickness (L) and considering the boundary condition $E_{3j}(0) = 0$ we arrive to

$$E_{3j}^{2\omega} = -\omega \sqrt{\frac{\mu_0}{\varepsilon_3}} d_{jik} E_{1i}^{\omega} E_{1k}^{\omega} \left(\frac{\exp[i\Delta KL] - 1}{\Delta K} \right). \tag{6.19}$$

We are interested in measuring the output power of that wave. Therefore,[16] we arrive to the next result:

$$P_j^{2\omega} = 8 \left(\frac{\mu_0}{\varepsilon_0} \right)^{\frac{3}{2}} \frac{\omega^2 \left(d_{jik} \right)^2 L^2}{n^3} (P_{1i}^{\omega})(P_{1k}^{\omega}) \frac{\sin^2 \left(\frac{\Delta KL}{2} \right)}{\left(\frac{\Delta KL}{2} \right)^2} A\,, \tag{6.20}$$

where n is the mean refractive index of the material, A is the impinging area and $P_j^{2\omega}$ is the SH output power polarized along the j direction.

6.3 LCs for SHG

SHG in FLCs is driven at a microscopic level by the molecular second order polarizability, known as hyperpolarizability tensor (**β**). The second-order susceptibility tensor directly depends on the molecular hyperpolarizability. Second-order nonlinear effects occur when the electromagnetic field of the light, gives rise to asymmetric charge transference between the different regions of the molecules. To obtain an important response, the best solution is to insert electron donor (D, high q^+) and acceptor (A, high q^-) groups interconnected by a conjugated electronic bridges and aromatic rings (π orbitals) to facilitate the charge transference. In addition, the donor and acceptor groups ($D - A$) must be placed in such a way that the symmetry of the mesophase allows the SHG to

appear[4]. Frequency doubling mechanism is sketched in Fig. 2 where the asymmetric induced polarization by the electric field of the light is depicted. Some of the Fourier components of the polarization wave are represented. The more asymmetric the polarization response, the larger the second harmonic term responsible of the SHG.

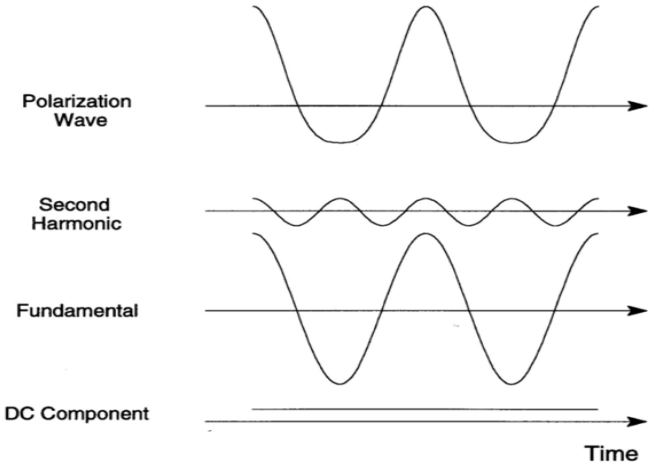

Fig. 2. Asymmetric polarization response to a sinusoidal intense electric field of frequency ω. In the figure different Fourier contributions are depicted. As the polarization response becomes more asymmetric, the 2ω Fourier component becomes more important (i.e more SHG component)[13].

In FLCs the electronic asymmetric response can only give rise to SHG light polarized along the C_2 direction, i.e. the polar axis. Therefore, FLCs for NLO applications must incorporate strong chromophores with a large hyperpolarizability ($\boldsymbol{\beta}$) along the polar axis. However, realizing such a goal without killing the required mesogenic character is really challenging. In the case of a calamitic LC, the chromophore must be placed as depicted in Fig. 3 and therefore the molecular aspect ratio is seriously altered, losing the elongated shape of the molecule required for LC phases. This drawback has resulted in very poor SHG efficiencies in standard calamitic LCs (see Table 2).

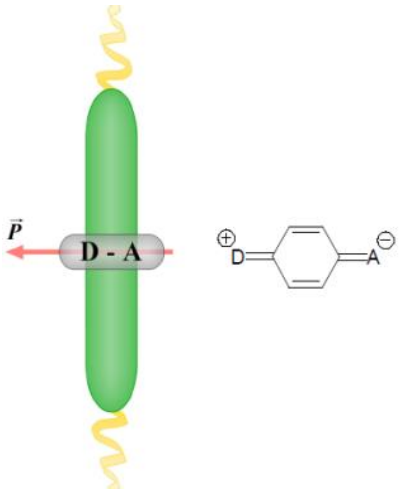

Fig. 3. Left: Calamitic molecule with a $D-A$ group perpendicular to its long axis. The length of this $D-A$ group enters in conflict with the compound mesogenicity. Right: Example of a $D-A$ group.

Compound	SHG coefficients (pmV^{-1})	Main drawbacks
The most efficient bent-core.	$d = 12.75$[18]	Difficult alignment. No LC in pure state.
Typical bent-core.	$d \approx 4.5$[19]	Difficult alignment.
SmC^* rod-like LC.	$d = 0.3$[20]	Small coefficients.
KDP	$d = 0.5$	
$LiNBO_3$	$d = 30$	
Solid organic NLO materials.	$d = 290$[21]	
Poled polymers.	$d \approx 60$[22]	Thermodynamically unstable phase.
Dimer.	$d = 4.5$[23]	
Trimer.	$d = 6.8$	

Table 2. Most efficient SHG coefficients of different NLO materials.

A different approach uses bent-core LCs. In bent-core mesophases, the molecules are packed as depicted in Fig. 4 (a). The bent shape of the molecular

cores hinders the free rotation of the molecules along the main director, which gives rise to the appearance of polarization along the **P** direction. As a consequence, the molecular geometry allows the incorporation of chromophores along the lateral wings preserving the mesogenic character of the material[24] and resulting in a strong **β** along the molecular C_2 axis (see Fig. 4 (b)). Remarkable SHG efficiencies have been obtained in this kind of LCs. Table 2 presents some of the measured values in different liquid crystals. As can be seen bent-core compounds present the best results obtained up to now.

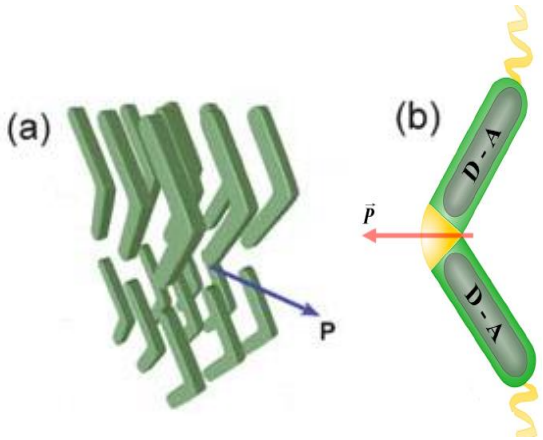

Fig. 4. (a) Molecular packing in a typical bent-core Sm mesophase. (b). In bent-shape molecules (bananas), the $D-A$ groups can be much larger, increasing the contribution of the SH signal along the polarization direction.

A new approach based on FLCs with potentially large NLO coefficients was pioneered by the Walba group based on a novel laterally azo-bridged H-shaped molecule. The structure includes a disperse red 1 (DR-1) chromophore[25, 26, 27]. The molecule consists of two rod-shaped mesogens connected by the chromophore. This molecular geometry allows the incorporation of long $D-A$ groups without losing the mesogenic character of the material. Unfortunately, the material only presented a monotropic mesophase of limited stability and in this work no SHG measurements were carried out. Based on the same idea, Yang et al synthesized a new H-shaped dimer using also the NLO disperse red

DR-1 chromophore $(D-A)$[24] as shown in Fig. 5(a). This new compound presents a stable enantiomeric SmC* phase. In this work SHG measurements were carried out and a maximum d coefficient of 4.5 pm V^{-1} was reported[24]. This value was the highest ever reported for a calamitic LC hitherto and is comparable to those obtained in banana compounds. See Fig. 5.

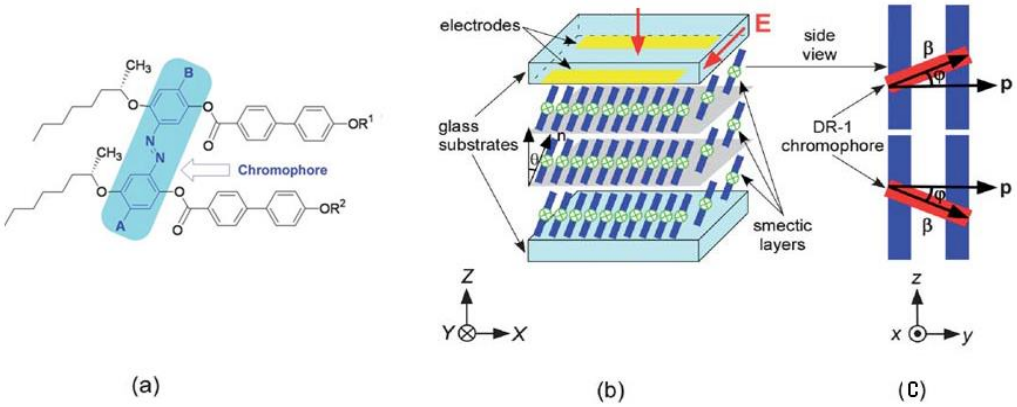

Fig 5. (a) Sketch of the H-shaped molecule of Ref. 25. (b) Molecular arrangement in the mesophase under electric field (**E**). The molecular director (**n**) is tilted an angle θ with respect to the layer normal (i. e the Z axis). (c) Two possible molecular orientations due to the head to tail invariance. φ is the angle between the long axis of the chromophore (**β**) and the polar **p** axis (i.e., currently the y axis) in the local molecular xyz reference frame.

6.4 SHG in the trimer

The promising results in the dimer compound pave the way for a new molecular shape approach; an azo-bridged trimer. Following the same idea as in the H-shaped molecules, the trimer studied in this work allows the incorporation of a longer chromophore (DNDPDA) along the FLCs polar axis. Fig. 6 shows the chemical composition of this new compound and its molecular sketch. It is particularly noteworthy that the trimer, incorporating three rod-shaped units into such a big molecule, exhibits a thermodynamically stable enantiotropic ferroelectric phase (SmC*). The mesomorphic behavior and the

phase transition temperatures are also indicated in Fig. 6. It is rather remarkable the wide temperature range of the SmC* phase (103ºC) that is even larger than the one of the dimer.

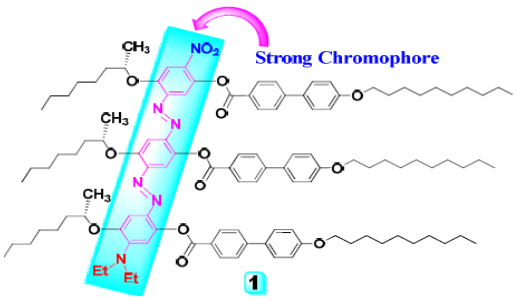

Fig. 6. The trimer FLC molecule. The mesomorphic behavior of the compound is as follows: Heating: Cr1 84 Cr2 123 SmC* 135 N* 146 Iso. Cooling: Iso 145 N* 134 SmC* 31 gSmC*.
Iso = the isotropic liquid; gSmC* = the glassy state of the SmC* phase; Cr = the crystalline state.

A complete characterization of this compound is beyond the scope of this work and can be found elsewhere[28]. In Fig. 7 we reproduce the absorption spectrum of the chromophore[29]. Due to the strong absorption at 572 nm a Nd:YAG laser is unsuitable for SHG measurements. Previous to this work, our group performed SHG measurements using a fundamental beam of 1369 nm[29, 30] where absorption of the SHG is lower. Results were outstanding since the so-called helicoidal phase matching (HPM)[31, 32, 33] was observed. Under this condition, a novel approach for SHG data analysis, involving both absorption and HPM, was developed[31]. This procedure gave a remarkable d_{22} coefficient of 28 pm V^{-1}. Nevertheless the result was resonantly enhanced due to the material absorption. Thus the actual SHG efficiency of the trimer for SHG applications was overestimated.

The indubitable interest of our compound for NLO applications led us to characterize the **d** tensor under no absorption conditions. This information is interesting to account for the transparency-efficiency trade-off in order to determine the most suitable wavelength for applications. For this purpose SHG

measurements under no absorption were carried out using light of 1560 nm. So, the wavelength of the second harmonic light (780 nm) is clearly above the region the absorption region (see Fig. 7).

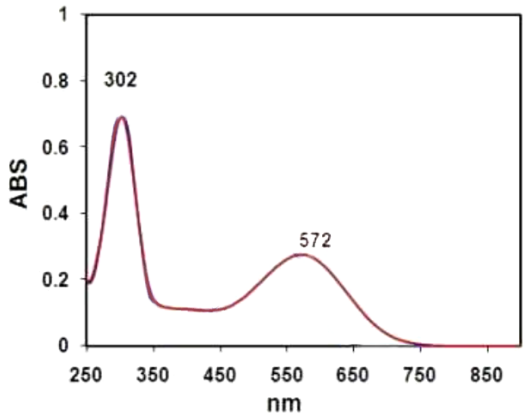

Fig. 7. Absorption spectrum of the chromophore[30].

6.4.1 Experimental setup

Fig. 8 shows the schematic representation of the used samples. The fundamental beam impinges perpendicularly to the substrate. The material is sandwiched between two glass plates one of them coated with ITO electrodes separated by a gap of 100 μm. This geometry allows applying in-plane electric fields, which aligns the sample in homeotropic arrangement (smectic layers parallel to the substrate). Thus monodomain can be easily induced within the gap. The quality of the alignment was confirmed by polarization microscopy, see Fig. 9. The sample was placed in a heating stage set on a rotating platform that allows us to control the incident angle of the fundamental beam and the temperature of the sample. The experimental setup is sketched in Fig. 10.

The fundamental beam is a Ti:sapphire oscillator-regenerative amplifier laser system that can provide a tunable output signal in the 300–2600 nm range. Measurements were carried out at 1560 nm wavelength. In order to account for laser fluctuations a reference branch is used after splitting the fundamental

beam. In this branch the SH signal generated by a BBO crystal plate is registered in a photodiode, as sketched in Fig. 10.

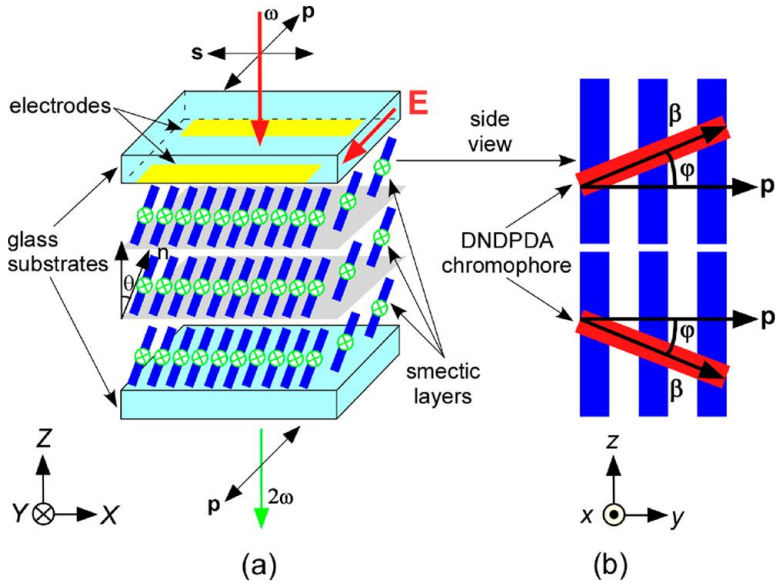

Fig. 8. Schemes showing (a) the molecular arrangement of the molecules in FLC phase. θ is the tilt angle between the director (**n**) and the layer normal (i.e. the Z axis) in the aligned zone in the XYZ reference frame, and (b) Schematic representation of the trimer molecule with two possible orientations due to the head to tail invariance. φ is the angle between the chromophore long axis **β** and the polar **p** axis (i.e. currently the y axis) in the local molecular xyz reference frame. The angle φ is about 28°.

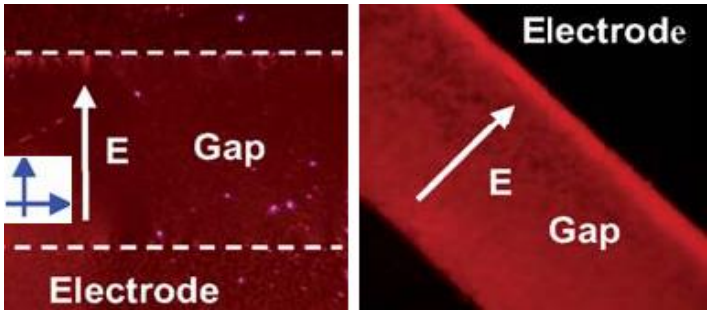

Fig. 9. Texture of the aligned sample (3.75 μm thickness, 166 °C, DC voltage of 1000 V across the gap of 100μm). Left: Polarizers along the indicatrix axes, the gap is between two dashed lines and cannot be distinguished from other regions. Right: the cell rotated 45° showing a uniform single domain in the gap. The electric field E is sketched in both pictures.

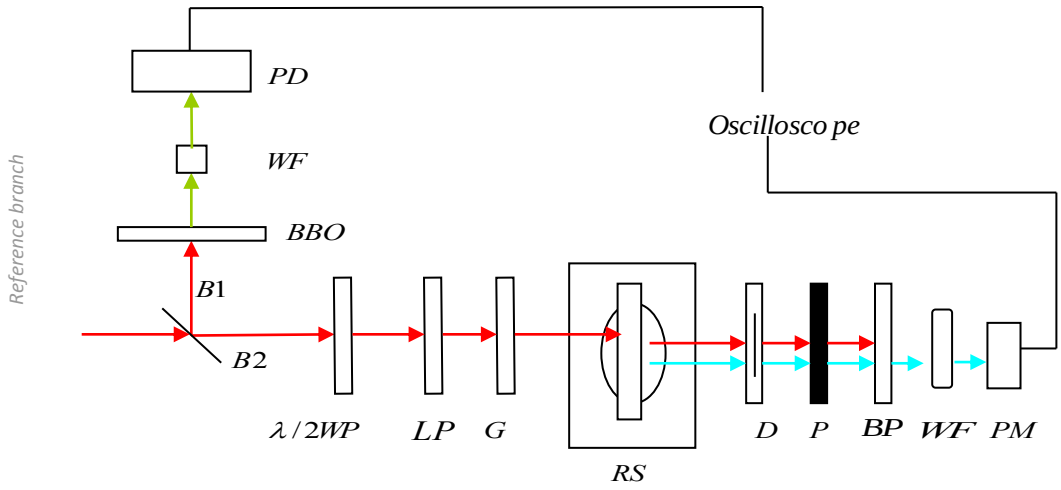

Fig. 10.Experimental setup: PD: photodiode, WF: water filter, BBO crystal plate, $\lambda/2$ WP: $\lambda/2$ wave plate, LP: longpass filter, G: slit, RS: rotating stage, D: diaphragm, P: Polarizer, BP: Bandpass filter, PM: photomultiplier. The sample is placed in the rotating stage.

6.4.2 Experiments and results

As previously mentioned, the SHG efficiency of a material is determined by the second order susceptibility tensor **d**. To obtain the corresponding components, Eq. (6.20) must be used. However, some of the parameters, as for example the fundamental beam power, are not easily accessible in the experiment. This drawback can be overcome by using a reference sample to calibrate the experimental setup. For this purpose we use a *Y*-cut quartz sample (d_{11} = 0.4 pm V^{-1}). Considering the transmittance Fresnel coefficients that appear as a consequence of the air-sample interfaces, and replacing light powers by their corresponding intensities, from Eq. (6.20) we arrive to

$$I_j^{2\omega} = 8\left(\frac{\mu_0}{\varepsilon_0}\right)^{\frac{3}{2}} \frac{\omega^2 \left(d_{ijk}\right)^2 L^2}{n^3} \left(I_{1i}^{\omega}\right)\left(I_{1k}^{\omega}\right) \frac{\sin^2\left(\frac{\Delta KL}{2}\right)}{\left(\frac{\Delta KL}{2}\right)^2} TA\,, \qquad (6.21)$$

where $I_j^{2\omega}$ denotes the SHG intensity collected for light polarized along the direction j, A the illuminated sample area and T is the total Fresnel coefficient that must be considered. In our case, two fundamental photons enter the

material to give rise to one SH photon that exits the material. Thus, T is given by:

$$T = (t^{\omega})^2 t^{2\omega} \,, \tag{6.22}$$

Our measurements are always carried out at normal incidence and, therefore,

$$t^{\omega} = \frac{4n_i^{\omega} n_t^{\omega}}{(n_i^{\omega} + n_t^{\omega})^2} \,, \tag{6.23}$$

$$t^{2\omega} = \frac{4n_t^{2\omega} n_i^{2\omega}}{(n_t^{2\omega} + n_i^{2\omega})^2} \,, \tag{6.24}$$

where n_i and n_t are the mean refractive indices of the air and the material respectively and ω and 2ω denote the frequencies of the considered waves. Neglecting dispersion, these indexes are considered as 1 and 1.5 for air and for the material respectively for ω and 2ω. Then we have

$$t = \frac{4n_i n_t}{(n_i + n_t)^2} = 0.96 \,, \tag{6.25}$$

$$T = (t)^3 = 0.88 \,, \tag{6.26}$$

Observing Eq. (6.21) we can see that the dependence of $I_j^{2\omega}$ versus phase mismatch ΔK, gives rise to the so-called maker fringes[34].

Dividing the SH intensity of the sample by that of the reference quartz at the maximum of a maker fringe ($\sin^2\left(\frac{\Delta K_C L_C}{2}\right) = 1$), we arrive to

$$\frac{I_M^{2\omega}}{I_C^{2\omega}} = \frac{d_M^2 \dfrac{\sin^2\left(\dfrac{\Delta K_M L_M}{2}\right)}{\Delta K_M^2} T_M A_M}{d_C^2 \dfrac{1}{\Delta K_C^2} T_C A_C} \,, \tag{6.27}$$

where the subscripts C and M refer to the quartz and the sample respectively.

From Eq. (6.27) it is straightforward to obtain:

$$d_M = \sqrt{\frac{I_M^{2\omega} A_C (\Delta K_M)^2 T_C d_C^2}{I_C^{2\omega} A_M (\Delta K_C)^2 T_M \sin^2\left(\frac{\Delta K_M L_M}{2}\right)}}. \tag{6.28}$$

Under electric field, our material presents a $C2$ symmetry axis along the polar direction Y (Fig. 11). Therefore, the only nonzero components of the contracted susceptibility **d** tensor in the XYZ reference system of Fig. 11 are

$$\begin{pmatrix} 0 & 0 & 0 & d_{14} & 0 & d_{16} \\ d_{21} & d_{22} & d_{23} & 0 & d_{25} & 0 \\ 0 & 0 & 0 & d_{34} & 0 & d_{36} \end{pmatrix}. \tag{6.29}$$

Thus we can rewrite Eq. (6.3) as

$$\begin{pmatrix} P_X^{2\omega} \\ P_Y^{2\omega} \\ P_Z^{2\omega} \end{pmatrix} = \begin{pmatrix} 0 & 0 & 0 & d_{14} & 0 & d_{16} \\ d_{21} & d_{22} & d_{23} & 0 & d_{25} & 0 \\ 0 & 0 & 0 & d_{34} & 0 & d_{36} \end{pmatrix} \begin{pmatrix} E_X^2 \\ E_Y^2 \\ E_Z^2 \\ 2E_Z E_Y \\ 2E_Z E_X \\ 2E_X E_Y \end{pmatrix}. \tag{6.30}$$

In our compound the donor-acceptor moiety is set roughly along the y-axis in Fig. 8 (b). Therefore the highest hyperpolarizability component is expected to be β_{yyy}, in the xyz reference frame of Fig. 8 (b). As a consequence, from a macroscopic point of view, the most important **d** coefficient must be d_{22} (d_{YY}, in the XYZ reference frame of Figs. 8 (a) and 11).

For the sake of completeness, we carried out SHG measurements with different polarization configurations for the fundamental and SH beams. We use four polarization combinations: $p-p$ (to obtain d_{22}), $s-p$ (d_{21}), $p-s$ ($d_{12}=0$) and $s-s$ (d_{11} =0); where p and s denote parallel and perpendicular to the applied field direction. The last two components must be zero by symmetry and were

measured to check the reliability of the experiment. Fig. 11 shows these possible combinations.

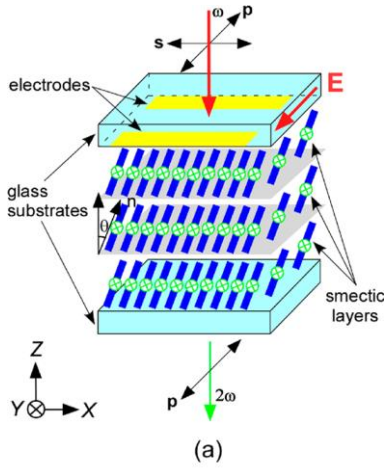

Fig 11. Scheme showing the geometry of FLC molecules of the trimer in the aligned zone and polarization of the input and output beams (i.e., $p-p$, $p-s$, $s-s$ and $s-p$) used in SHG experiments. XYZ is the reference frame.

6.4.3 p-p polarization

In order to determine the second order susceptibility coefficients, Eq. (6.27) must be used. However, ΔK_M is also unknown. Both parameters can be obtained by measuring several samples with different thickness (2 μm, 3.75 μm, 7 μm and 11 μm). Thus, by fitting $\frac{I_M^{2\omega}}{I_C^{2\omega}}$ to the sample thickness using Eq. (6.27) we find ΔK_M and d_{22}. See Fig. 12.

Taking into account the quartz reference values: $\Delta K_C = 0.089\ \mu m^{-1}$, $d_C = 0.4\ pm\ V^{-1}$ and $\frac{A_M}{A_C} = 4.4$, we fit the experimental points in Fig. 12 to Eq. (6.27) and we obtain d_{22} and ΔK_M:

$$\Delta K_M = 0.46\ \mu m^{-1}$$

and

$$d_{22} = 6.8 \text{ pm V}^{-1}.$$

Therefore, $\Delta n = \Delta K_M \frac{c}{2\omega} = 0.058$.

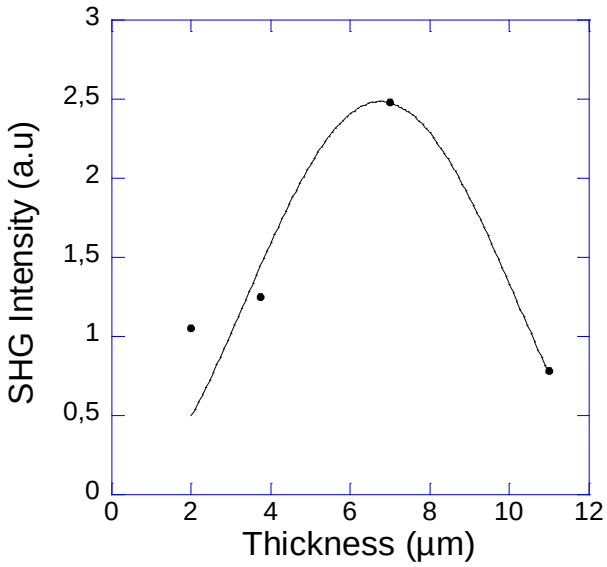

Fig 12. $\frac{I_M^{2\omega}}{I_C^{2\omega}}$ *vs*. the samples thickness.

This remarkable result is the largest non-enhanced d coefficient found for a FLC so far. Other reported values are shown in Table 2. Another important features are the broad temperature range of the SmC* phase, almost down to room temperature, and the good alignment easily achievable under the application of an electric field. All these features make of this material a very promising candidate for NLO applications.

6.4.4 s-p polarization

In this case, the plot of SHG intensity *vs*. sample thickness is shown in Fig. 13. Following the same procedure as in the $p - p$ configuration we arrive to:

$$\Delta K_M = 0.097 \text{ µm}^{-1}$$

and

$$d_{21} = 1.8 \text{ pm V}^{-1},$$

Therefore, $\Delta n = \Delta K_M \frac{c}{2\omega} = 0.012$.

As expected, taking into account the molecular geometry, this coefficient is not as large as d_{22} but is remarkable for the FCLs standards.

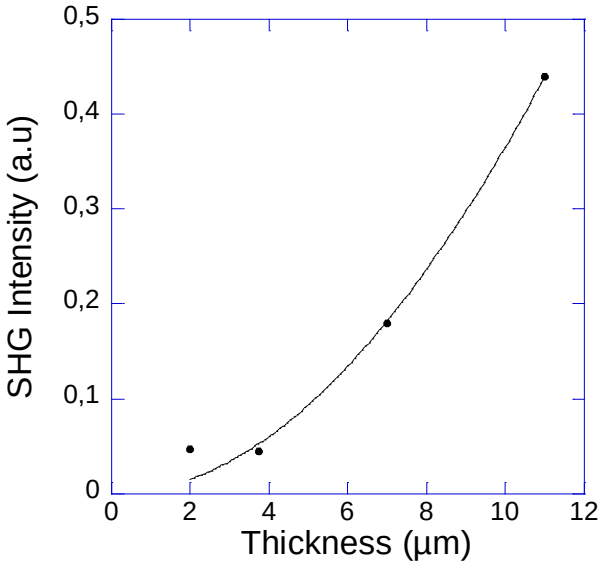

Fig 13. $\frac{I_M^{2\omega}}{I_C^{2\omega}}$ *vs.* the samples thickness.

6.4.5 p-s and s-s polarizations

Under these experimental configurations no SHG signal was detected. Therefore $d_{12} = d_{11} = 0$ as expected.

6.4.6 Evaluation of macroscopic NLO data at a microscopic level

In this section we are going to compare our experimental results with theoretical calculations obtained from molecular and structural parameters. It is well known that the second-order optical strength of a bulk organic material originates primarily from the hyperpolarizability of its molecular chromophore. Therefore, to link macroscopic and microscopic parameters we will use the

oriented gas model and assume that **β** of the trimer is equal to that of its molecular chromophore. We will also assume that the chromophore hyperpolarizability has only one longitudinal component along the chormophore long axis; (β_{uuu} , being **u** the unit vector along the long axis of the chromophore).

Usually to obtain **β** values the EFISH technique is used together with the Guggenheim method, which permits determining the dipolar moment μ_g of the molecule. Unfortunately no EFISH data have been reported for DNDPDA. Nevertheless, there exists one work that gives $\mu_g\beta_{uuu}$ values for the DNDPDA from the solvatochromic shift[35] of the absorption spectra of the chromophore in different solvents. In order to obtain the corresponding values at the wavelength used in our experiment (1560 nm.) we assumed a two level model [36]

$$\beta_{uuu}\mu_g = \frac{3e^2\hbar^2}{2m}\left(f\Delta\mu\mu_g\right)\frac{W}{[W^2-(2\hbar\omega)^2][W^2-(\hbar\omega)^2]},$$

where e is the elementary charge,$\hbar$ is Plank´s constant, m is the electron mass, W is the transition energy, f is the oscillator strength, $\Delta\mu$ is the difference between the dipole moment at the excited and ground states and μ_g is the dipole moment at the ground state of the chromophore. The values of W, f and $\Delta\mu\mu_g$ are taken from the literature[36]. Using such model, and assuming a value of μ_g for DNDPDA similar to that of the well known DR-1 (7 D), it was found that $\beta_{uuu} = 147\ 10^{-30}$ esu (1 pm/V = 2.387 x 10^{-9} esu).

Next we turn to discuss some structural aspects of the molecules in the mesophase. In our compound, the chromophore adopts a configuration with an angle $\varphi = 28^{o}$ with respect to the FLC's polar axis. This means that the β_{uuu} component also makes the same angle φ with the polar axis (see Fig. 14). On the other hand, due to head-tail invariance, smectic layers consist in a 50:50 mixture of two possible molecular orientations ($\pm\varphi$). Hence, the only non-null **β** tensor

components of the `averaged molecule' in the xyz reference frame (see Fig. 14) are

$$\beta_{yyy} = \beta_{uuu}\cos^3(\varphi) \tag{6.31}$$

and

$$\beta_{yzz} = \beta_{uuu}\cos(\varphi)\sin^2(\varphi)\,. \tag{6.32}$$

To make our model more realistic we permit some disorder of the molecules in the material, with the possibility of molecular rotation around the z axis (see Fig. 14). In an elementary approach, the disorder is simply characterized by a deviation of the molecular plane from its average position, with an angle Ψ between the y and Y axes (see Figs. 8 and 14). Then, in the xyz reference frame, the tensor components of the `average molecule´ are

$$\beta^d_{yyy} = \beta_{yyy}\langle\cos^3(\Psi)\rangle\,, \tag{6.33}$$

$$\beta^d_{yxx} = \beta_{yyy}\langle\cos(\Psi)\sin^2(\Psi)\rangle\,, \tag{6.34}$$

and

$$\beta^d_{yzz} = \beta_{yzz}\langle\cos(\Psi)\rangle\,, \tag{6.35}$$

with the symbol <> expressing thermal average. Finally, in the XYZ reference frame for SHG experiments (see Fig. 8) the **d** tensor components in which we are interested can be expressed as

$$d_{22} = Nf^3\beta^{(d)}_{YYY} = Nf^3\beta^{(d)}_{yyy}\,, \tag{6.36}$$

$$d_{21} = Nf^3\beta^d_{YXX} = Nf^3\left(\beta^{(d)}_{yxx}\cos^2(\theta) + \beta^{(d)}_{yzz}\sin^2(\theta)\right), \tag{6.37}$$

$$d_{23} = Nf^3\beta^d_{YZZ} = Nf^3\left(\beta^{(d)}_{yzz}\cos^2(\theta) + \beta^{(d)}_{yxx}\sin^2(\theta)\right) \tag{6.38}$$

and

$$d_{14} = Nf^3\beta^d_{XYZ} = Nf^3\left(\beta^{(d)}_{yxx}\sin(\theta)\cos(\theta) - \beta^{(d)}_{yzz}\sin(\theta)\cos(\theta)\right), \quad (6.39)$$

where N, θ and f are the number of FLC molecules per unit of volume, the molecular tilt angle and the local field factor. Where the local field-factors for ω and 2ω are assumed to be the same and the Lorentz formula has been used for them, $f = \frac{(n^2+2)}{3}$, with an average refractive index n =1.52.

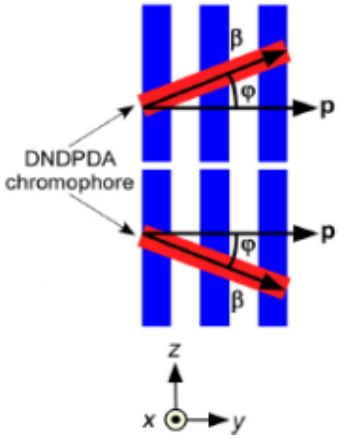

Fig. 15. Two possible molecular orientations with an angle ±φ between the **β** vector component and the polar axis **p** (i.e currently the y axis) in the xyz reference frame.

The term $\langle\cos(\Psi)\rangle$ represents the degree of polar order of the material and links the spontaneous polarization P_s with the molecular dipole moment μ_P along the polar axis through the expression $P_S = N\mu_P\langle\cos(\Psi)\rangle$. If the density of the compound is assumed to be $\rho = 1\text{gcm}^{-3}$ then $N = 3.27\,10^{-26}\text{m}^{-3}$. Taking $\mu_p = 1D$ along the polar axis (calculated using AM1 molecular model) and the experimental $P_S \approx 27$ nC cm^{-2} [28] at 120 °C we get $\langle\cos(\Psi)\rangle = 0.23$.

Assuming a Gaussian distribution for the Ψ angles: $\langle\cos^3(\Psi) \approx 0.7\,\langle\cos(\Psi)\rangle\rangle$. And after careful numerical calculations we obtain: d_{22} = 6.02 and d_{21} = 2.56 pm V^{-1}. Given the roughness of this model and the amount of approximations, the agreement with the experimental results, d_{22} = 6.8 pm V^{-1} and d_{21} =1.8 pm V^{-1}, is rather remarkable.

6.5 THG in the trimer

Besides a strong SHG response in the SmC* phase, the trimer was also found to exhibit a strong THG response. Contrary to SHG, THG occurs in centrosymmetric media. To characterize the THG of the material, measurements were carried out in the isotropic liquid (150 °C) only for simplicity since, in the isotropic state the effect is determined by a single third order susceptibility coefficient $\chi^{3\omega}$.

The trimer is highly absorbing at $\lambda = 520$ nm (see Fig. 7). Unfortunately, to the best of our knowledge, it does not exist a theory of THG for absorbing materials. However, the main features of the THG intensity propagating in an absorbing medium can be deduced on the basic of a simple model. In our experiment the material is transparent for the fundamental wave and therefore we will only consider the TH wave absorption, with an absorption coefficient α (2.57 μm^{-1} from Fig. 7). The electric field of the fundamental wave propagating along the z direction in the medium can be expressed as:

$$\mathbf{E}^{\omega}(z,t) = \mathbf{E}_0^{\omega}\exp[i(k^{\omega}z - \omega t)] \tag{6.40}$$

where $\mathbf{E}_0^{\omega}$ is a constant vector if we assume that the fundamental wave is not depleted, $k^{\omega} = \frac{2\pi}{\lambda}n^{\omega}$, λ being the fundamental wavelength and n^{ω} the corresponding refractive index. The third harmonic electric field generated in a sample slice of thickness dz as that shown in Fig. 16 is given by:

$$d\mathbf{E}^{3\omega}(z) \propto \chi^{3\omega}|\mathbf{E}_0^{\omega}|^2\exp[i3k^{\omega}z]\mathbf{E}_0^{\omega}dz\,. \tag{6.41}$$

Therefore the amplitude of the TH electric field emerging from the sample can be obtained by summing coherently the contribution of the slices of the whole sample, and is given by:

$$\mathbf{E}_0^{3\omega}(L) \propto \int_0^L \chi^{3\omega} |\mathbf{E}_0^{\omega}|^2 \exp[i3k^{\omega}z] \mathbf{E}_0^{\omega} \exp\left[\frac{-\alpha(L-z)}{2} + ik^{3\omega}(L-z)\right] dz\,, \qquad (6.42)$$

where $k^{3\omega} = \frac{6\pi}{\lambda} n^{3\omega}$, $n^{3\omega}$ being the refractive index corresponding to the TH electric field. Here the term $\exp\left[\frac{-\alpha(L-z)}{2}\right]$ takes into account the absorption of the TH signal along its path through the sample. Thus, the THG total intensity emerging from the sample can be expressed as:

$$I^{3\omega} \propto \left|\mathbf{E}_0^{3\omega}(L)\right|^2 \propto [\chi^{3\omega}]^2 I_{\omega}^3 L^2 \exp\left[\frac{-\alpha L}{2}\right] \frac{\sin^2\left(\frac{\Delta K L}{2}\right) + \sinh^2\left(\frac{\alpha L}{4}\right)}{\left(\frac{\Delta K L}{2}\right)^2 + \left(\frac{\alpha L}{4}\right)^2}\,, \qquad (6.43)$$

where $\Delta K = \frac{6\pi}{\lambda}(n_{3\omega} - n_{\omega})$.

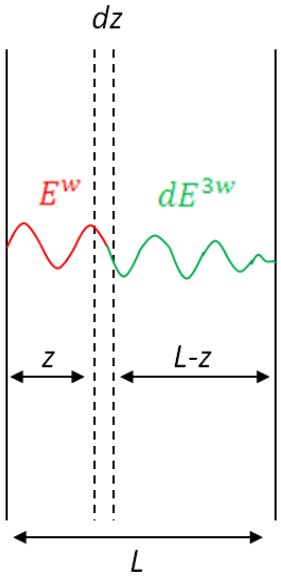

Fig. 16. Schematic representation of the third harmonic generated in a slice of an absorbing sample.

For our measurements we used the same experimental setup and procedure as for SHG, the only difference was that we changed the band pass filter. Also the same samples where used. THG measurements were performed at normal incidence. In this case as a reference we used a $BK7$ sample of 150 nm thickness,

$\chi^{3\omega(BK7)} = 4.4\ 10^{-14}$ esu and a coherence length of $l_c = \pi/\Delta K_{BK7}$ =16.4 μm. $BK7$ is completely transparent at the TH wavelength of 520 nm. First, we checked that the TH signal had the same polarization as the fundamental beam, as expected. The THG data for five samples were compared with the THG at the maximum of the Maker fringe[35] of the $BK7$ under the same conditions of illumination. The dependence of THG intensity ratios on sample thicknesses is shown in Fig. 17. From Eq. (6.43), the ratio of both signals is given by

$$\frac{I_M^{3\omega}}{I_{BK7}^{3\omega}} = \left(\frac{\Delta K_{BK7}}{2}\right)^2 \frac{|\chi_M^{3\omega}|^2}{|\chi_{BK7}^{3\omega}|^2} L_M^2 \exp\left[\frac{-\alpha L_M}{2}\right] \frac{\sin^2\left(\frac{\Delta K_M L_M}{2}\right) + \sinh^2\left(\frac{\alpha L_M}{4}\right)}{\left(\frac{\Delta K_M L_M}{2}\right)^2 + \left(\frac{\alpha L_M}{4}\right)^2}, \quad (6.44)$$

where the subscripts $BK7$ and M refer to the $BK7$ and to the sample respectively.

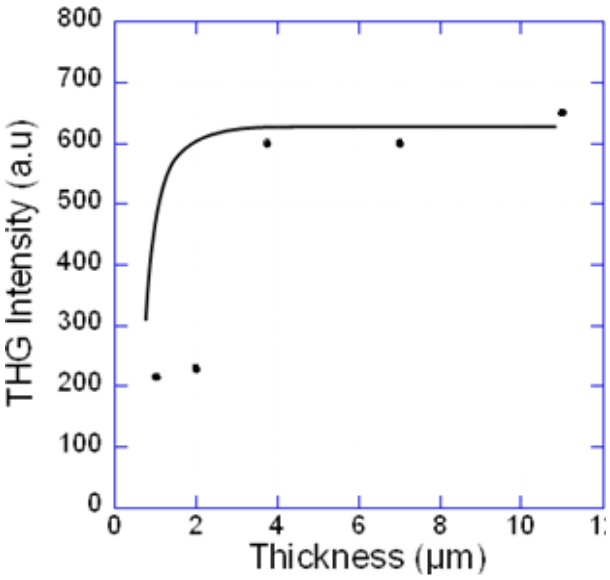

Fig. 17. THG signal intensity as a function of the cell thickness.

Owing to the strong absorption at the third harmonic wavelength, the $\sinh -$ term is always much larger than the $\sin -$term in Eq. (6.44). No oscillations are visible in the intensity ratio, as shown in Fig. 17, and we even

observed saturation for rather small thickness values. Based on the above argument, Eq. (6.44) can be simplified to

$$\frac{I_M^{3\omega}}{I_{BK7}^{3\omega}} \approx \left(\frac{\Delta k_{BK7}}{2}\right)^2 \frac{|\chi_M^{3\omega}|^2}{|\chi_{BK7}^{3\omega}|^2} \frac{1}{4} \frac{\left(1 - 2\exp\left[\frac{-\alpha L_M}{2}\right] + \exp[-\alpha L_M]\right)}{\left(\frac{\Delta k_M}{2}\right)^2 + \left(\frac{\alpha}{4}\right)^2}, \qquad (6.45)$$

Black line in Fig. 17 represents the fit of the measured values to Eq. (6.45). In Eq. (6.45), ΔK_{BK7} and χ_{BK7}^{3w} are known, so there is only one relevant fit parameter. This parameter,

$$\left(\frac{\Delta K_{BK7}}{4}\right)^2 \frac{|\chi_M^{3\omega}|^2}{|\chi_{BK7}^{3\omega}|^2} \frac{1}{\left(\frac{\Delta K_M}{2}\right)^2 + \left(\frac{\alpha}{4}\right)^2}, \qquad (6.46)$$

plays the role of a scale factor, and admixes $\chi_M^{3\omega}$ and ΔK_M, so both quantities cannot be obtained separately.

The numerical value of the parameter finally gives

$$\chi_M^{3\omega} = \sqrt{1 + \left(\frac{n^{3\omega} - n^{\omega}}{0.106}\right)^2}\ 1.5\ 10^{-11}\text{esu}\,. \qquad (6.47)$$

If $n^{3\omega} - n^{\omega} = 0$ the lower limit for $\chi_M^{3\omega}$ is 1.5 10 $^{-11}$ esu. On the other hand, for a conservatively estimated dispersion parameter of $n^{3\omega} - n^{\omega} = 0.18$, a $\chi^{3\omega}$value of ~3 10 $^{-11}$ esu is obtained at $\lambda = 1.56$ μm. This value is comparable to the largest value (4.8 10 $^{-11}$ esu at $\lambda = 1.5$ μm) measured for a PMMA polymer attached with a DNDPDA dye pendant (44 wt% dye content)[37]. This result is consistent with our THG measurements for the trimer, in which DNDPDA dye density is ~ 22 wt%. As far as we know, the trimer not only exhibits the largest third-order susceptibility to date for low-molecular weight LCs[38] but its $\chi^{3\omega}$ value is much larger than $\chi^{3\omega} = 0.74\ 10^{-11}$ esu at $\lambda = 1.9$ μm for the commonly

used NLO chromophore 4-diethylamino-4′- nitrostilbene (DEANS) in single crystals[39] and the largest $\chi^{3\omega}$ value of 0.58 10^{-11} esu at $\lambda = 1.064$ μm (0.056 10^{-11} esu at $\lambda = 1.579$ μm) for a series of nematic liquid crystalline polymers[40]. However, the obtained result is resonance enhanced. A characterization of the THG dispersion will be required in order to determine the transparency-efficiency trade-off in this material. This task should be tackled in the future.

6.6 Conclusions

We report a laterally azo-bridged trimesogen which incorporates a strong chromophore along its FLC polar axis. It is remarkable that the compound, which links three rod-like units together via two azo groups, exhibits a SmC* phase with a broad phase temperature range of 103 K during cooling. It is worthy to note that, like rod-shaped liquid crystals for display applications, the trimer can be easily aligned in homeotropic configuration upon applying a relatively weak in-plane E-field. In addition the mesophase is thermodynamically stable. The main components of the second order susceptibility tensor **d** have been determined by means of SHG measurements, using a fundamental wavelength fare away from absorption (1560 nm). It is remarkable the high performance exhibited by the material which is very outstanding among liquid crystals. The largest measured coefficient d_{22} is the optimal one from the viewpoint of molecular design. In addition, a theoretical estimation of the macroscopic NLO coefficients has been made in terms of the molecular and structural parameters. Good agreement is found between the estimated and the experimental d_{22} and d_{21} values.

Besides a strong SHG response in the SmC* phase, the trimer was also found to exhibit a strong THG response. To the best of our knowledge, the measured χ^3

value is the highest one reported for a LC. Nevertheless, our measurements where made under high absorption and this result is resonantly enhanced.

[1] Y. Shi, C. Zhang, H. Zhang, J. H. Bechtel, L. R. Dalton, B. H. Robinson and W. H. Steier, *Science*, **288**, 119 (2000).

[2] M. Lee, H. E. Katz, C. Erben, D. M. Gill, P. Gopalan, J. D. Heber and D. J. McGee, *Science*, **298**, 1401 (2002).

[3] J. M. Hales, J. Matichak, S. Barlow, S. Ohira, K. Yesudas, J. L. Bredas, J. W. Perry and S. R. Marder, *Science*, **327**, 1485 (2010).

[4] H. S. Nalwa and S. Miyata, "*Nonlinear optics of organic molecules and polymers*", CRC Press Inc (1996).

[5] S. Yitzchaik and T. J. Marks, *Acc. Chem. Res.* **29**, 197 (1996).

[6] S. R. Marder, *Chem. Commun.* **2**, 131 (2006).

[7] P. Innocenzi and B. J. Lebeau, *Mater. Chem.* **15**, 3821 (2005).

[8] B. J. Coe, *Acc. Chem. Res*. **39**, 383 (2006).

[9] P. A. Sullivan and L. R. Dalton, *Acc. Chem. Res.* **433**, 10 (2010).

[10] S.T. Lagerwall, "*Ferroelectric and antiferroelectric liquid crystals*", Wiley (1999).

[11] Y. Zhang and J. Etxebarria, "*Liquid crystals beyond displays*", Wiley (2012).

[12] B. Champagne, J. Guthmuller, F. Perreault and A. J. Soldera, *Phys. Chem.* **116**, 7552 (2012).

[13] S. J. Frank L. Pedrotti and L. S. Pedrotti, "*Introduction to optics*", Prentice Hall (1993).

[14] P.A. Franken, A. E. Hill, C. W. Peters and G. Weinreich, *Phys. Rev. Lett*. **7**, 118 (1961).

[15] F. Agulló-López, J.M Cabrera and F. Agulló-Rueda, "*Electrooptics. Phenomena, Materials and Applications*", Academic Press London (1994).

[16] A. Yariv, "*Optical Waves in Crystals*", Wiley (1984).

[17] D. A. Kleinman, *Phys. Rev.* **126**, 1977 (1962).

[18] C. I. Pintre, J. L. Serrano, M. B. Ros, J. M. Perdiguero, I. Alonso, J. Ortega, C. L. Folcia, J. Etxebarria, R. Alicante and B. Villacampa, *J. Mater. Chem*. **20**, 2965 (2010).

[19] J. Ortega, J. A. Gallastegui, C. L. Folcia, J. Etxebarria, N. Gimeno and M. B. Ros, *Liq. Cryst.* **31**, 579 (2004).

[20] N. Pereda, C. L. Folcia, J. Etxebarria and J. Ortega, *Liq. Cryst.* **26**, 375 (1999).

[21] H. Figi, L. Mutter, C. Hunziker, M. Jazbinsek, P. Günter and B. J. Coe, *J. Opt. Soc. Am. B*, **25**, 1786 (2008).

[22] M. J. Choi, D. H. Choi, P. A. Sullivan, A. J. P. Akelaitis and L. R. Dalton, *Prog. Polym. Sci.* **33**, 1013 (2008).

[23] J. M. Perdiguero, Y. Zhang, C. Walker, J. Etxebarria, C. L. Folcia, J. Ortega, M. J. O'Callaghan and U. Baumeister, *J. Mater. Chem.* **20**, 4905 (2010).

[24] J. Ortega, N. Pereda, C.L Folcia, J. Etxebarria and M.B. Ros, *Phys. Rev. Lett.* **81**, 4408 (2000).

[25] D. M. Walba, D. J. Dyer, T. Sierra, P. L. Cobben, R. Shao and N. A. Clark, *J. Am. Chem. Soc.* **118**, 1211 (1996).

[26] D. M. Walba, L. Xiao, P. Keller, R. Shao, D. Link and N. A. Clark, *Pure Appl. Chem.* **71**, 2117 (1999).

[27] D. M. Walba, L. Xiao, E. Korblova, P. Keller, R. Shoemaker, M. Nakata, R. Shao, D. R. Link, D. A. Coleman and N. A. Clark, *Ferroelectrics,* **309**, 77 (2004).

[28] Y. Zhang, J. Ortega, U. Baumeister, C. L. Folcia, G. Sanz-Enguita, C. Walker, S. Rodriguez-Conde, J. Etxebarria, M. J. O'Callaghan and K. More, *J. Am. Chem. Soc.* **134**, 16298 (2012).

[29] Y. Zhang, J. Martinez-Perdiguero, U. Baumeister, C. Walker, J. Etxebarria, M. Prehm, J. Ortega, C. Tschierske, M. J. O'Callaghan, A. Harant and M. Handschy, *J. Am. Chem. Soc.* **131**, 18386 (2009).

[30] J. Etxebarria, J. Ortega, C. L. Folcia, Y. Zhang and C. Walker, *Phys. Rev. E*, **86,** 051707 (2012).

[31] I. Drevensek-Olenik and M. Copic, *Phys Rev. E*, **56**, 581 (1997).

[32] H. Hoshi, D. H. Chung, K. Ishikawa and H. Takezoe, *Phys. Rev. E*, **63**, 056610 (2001).

[33] V. A. Belyakov and N. V. Shipov, *Phys. Lett.* **86**, 94 (1981).

[34] J. Jerphagnon and S. K. Kurtz, *J. of Appl. Phys.* **41**, 1667 (1970).

[35] H. Suzuki and H. Hiratsuka, *Proc. SPIE*, **971**, 97 (1988).

[36] D. S. Chemla and J. Zyss, "*Nonlinear optical properties of organic molecules and crystals*", Academic New York (1987).

[37] T. Kaino, S. Tomaru, T. Kurihara and M. Amano, *M. Mater. Res. Soc. Symp. Proc.* **247**, 179 (1992).

[38] H. S. Nalwa, *Adv. Mater*, **5**, 341 (1993).

[39] T. Kurihara, H. Kabayashi, K. Kubodera and T. Kaino, *Opt. Commu*n. **84**, 149 (1991).

[40] D. A. Smith and H. J. Coles, *Liq. Cryst.* **14**, 937 (1993).

APPENDIX

Appendix

In this appendix we want to show how the second component of Eq. (6.1), for the particular case of SHG, takes the form of Eq. (6.2).

First of all, let us recall Eq. (6.1):

$$P_i = \varepsilon_0 \chi_{i\,j} E_j + 2 d_{i\,j\,k} E_j E_k + 4 \chi_{i\,j\,k\,l} E_j E_k E_l + \cdots, \tag{6.1}$$

where P_i and E_i denote the polarization and electric field components respectively and their dependence in t and z has been omitted for the sake of simplicity. ε_0 is the electric permittivity of vacuum and $\chi_{i\,j}$, $d_{i\,j\,k}$, $\chi_{i\,j\,k\,l}$ are the susceptibility tensors of first, second and third order respectively. Higher order terms have been suppressed in Eq. (6.1). Subscripts i, j, k and l denote the Cartesian coordinates and summation over repeated indices is assumed (Einstein's notation).

Let's consider the time dependent part of two electric fields with frequencies $\omega 1$ and $\omega 2$:

$$E_j^{\omega 1}(t) = \frac{1}{2}\left(E_j^{\omega 1} \exp[i\omega 1 t] + c.c\right) \tag{AI.1}$$

and

$$E_k^{\omega 2}(t) = \frac{1}{2}\left(E_k^{\omega 2} \exp[i\omega 2 t] + c.c\right), \tag{AI.2}$$

where $E_j^{\omega 1}$ and $E_k^{\omega 2}$ are the time independent parts of the fields, the subscripts j, k and l denote the Cartesian coordinates and $c.c$ refers to the complex conjugate.

Focusing our attention on the second order term of Eq. (6.1) and, using Eqs. (AI.1) and (AI.2) we can obtain the polarization component of the frequency sum, i.e. at $\omega 3 = \omega 1 + \omega 2$ as follows:

$$P_i^{\omega 1+\omega 2}(t) = 2d_{i\,j\,k}\left(\frac{1}{2}E_j^{\omega 1}\exp[i\omega 1t] + \frac{1}{2}E_j^{\omega 2}\exp[i\omega 2t] + c.c\right)\left(\frac{1}{2}E_k^{\omega 1}\exp[i\omega 1t] + \frac{1}{2}E_k^{\omega 2}\exp[i\omega 2t] + c.c\right). \quad (AI.3)$$

Since we are concerned with SHG, we consider only the sum-frequency terms, so we have

$$P_i^{\omega 1+\omega 2}(t) = \frac{1}{2}\left(d_{i\,j\,k}E_j^{\omega 1}E_k^{\omega 2}\exp[i(\omega 1+\omega 2)t] + d_{i\,k\,j}E_k^{\omega 2}E_j^{\omega 1}\exp[i(\omega 1+\omega 2)t] + c.c\right). \quad (AI.4)$$

In a non-absorbing media or in the particular case of SHG, $d_{i\,k\,j} = d_{i\,j\,k}$, therefore

$$P_i^{\omega 1+\omega 2}(t) = \frac{1}{2}d_{i\,j\,k}\left(2E_j^{\omega 1}E_k^{\omega 2}\exp[i(\omega 1+\omega 2)t] + c.c\right). \quad (AI.5)$$

On the other hand, we can write the polarization as follows:

$$P_i^{\omega 1+\omega 2}(t) = \frac{1}{2}(P_i^{\omega 1+\omega 2}\exp[i(\omega 1+\omega 2)t] + c.c), \quad (AI.6)$$

where $P_i^{\omega 1+\omega 2}$ is the time independent part of the polarization.

Therefore, we get:

$$P_i^{\omega_1+\omega_2} = 2d_{i\,j\,k}E_j^{\omega_1}E_k^{\omega_2}. \quad (AI.7)$$

Note that for the particular case of SHG, since just one field is involved, from Eq. (AI.5) it can be deduced that:

$$P_i^{2\omega} = d_{i\,j\,k}E_j^{\omega}E_k^{\omega}. \quad (AI.8)$$

General conclusions

This dissertation deals with optical functionalities of LCs. The main part (chapters 2, 3, 4 and 5) is dedicated to CLCs and their ability for light amplification. On the other hand, chapter 6 is in some way independent of the previous chapters and deals with NLO. In this section we are going to expose briefly the main conclusions of this dissertation.

CLCs are compelling materials for laser generation due to several features as ease of construction and wavelength tunability. In order to use simpler and more economic pumping sources their performance must be optimized. In this respect, we have studied the dependence of the lasing efficiency on the sample thickness. One of the main conclusions we have drawn is that the slope efficiency $\eta(L)$ presents a very pronounced variation with the sample thickness and therefore, contrary to the general belief, it is the parameter that must be optimized instead of the threshold energy $E_{th}(L)$. In addition, we have determined that there is minimum for $E_{th}(L)$ and a maximum for $\eta(L)$ at somewhat different thicknesses. The experimental results are in good agreement with numerical calculations based in previous theoretical models. As a further step, analytical expressions for E_{th} and η have also been deduced. These expressions are in excellent agreement with previous numerical calculations and permit to analyze easily the influence of the dye and CLC parameters on the performance of the laser. So, they are a powerful and novel tool for laser optimization. Such expressions also show that the quantum yield to the triplet level and the width of the pumping pulse have a similar effect in the laser operating mechanism. The increase of both is detrimental to the laser. This explains, partially, the difficulty in the realization of CLC lasers pumped by CW light sources. On the basis of the same numerical models, we have also described in detail the kinetic behavior of these devices. In such respect, we have confirmed experimentally the predicted results, i.e. as the pumping energy

increases, duration of the fluorescence pulse decreases, reaching a minimum at the threshold energy. Above the threshold the temporal profiles are irregular and consist of a set of narrow pulses whose measured duration is limited by the detector risetime.

Finally we have tackled the controversial problem of explaining the alteration of the fluorescence spectrum of the dye when it is dissolved in a CLC structure since, according to the experiments of other authors, the fluorescence time τ_f is not substantially altered by the CLC cavity. On the basis of the previous numerical model, we have shown that the fluorescent output power is proportional the inverse of the radiative time of the dye ($\propto 1/\tau_r$) and the pulse duration is driven by τ_f. Therefore, in order to conciliate both the results, the modifications of the radiative and nonradiative de-excitation rates in the CLC cavity must be opposite to each other.

One of the main drawbacks of these devices is their degradation due to dye bleaching. Another indirect but important consequence of the dye degradation can also be the light scattering inside the cavity. We have shown that, in last instance, the origin of this problem is the heating of the dye molecules, the performance of CLC lasers should highly improve with dyes showing low quantum yields to triplet states. Nevertheless, it is remarkable to say that by optimizing the laser cavity parameters, low pumping energies can be used. In this way, thermal degradation of the dye molecules can be made negligible in many practical situations. Actually, some of the samples used in this dissertation have lasted for months without showing deterioration.

Finally chapter 6 is dedicated to NLO. In this respect, we report a laterally azo-bridged trimesogen, which incorporates a strong chromophore along its FLC polar axis. It is worth mentioning that the compound, which consist of three rod-like units linked by two azo groups, exhibits a SmC* phase with a broad

phase temperature range. It is remarkable the high performance exhibited by the material which is very outstanding among liquid crystals. In addition, a theoretical estimation of the macroscopic NLO coefficients has been made in terms of the molecular and structural parameters. Good agreement is found between the estimated and the experimental d_{22} and d_{21} values.

Apart from a strong SHG response in the SmC* phase, the trimer also exhibited a strong THG response. Up to our knowledge, the measured χ^3 value is the highest one reported for a LC. However, our measurements where made under high absorption and presumably the results are resonantly enhanced.

List of publications

"Role of the sample thickness on the performance of cholesteric liquid crystal lasers: Experimental, numerical, and analytical results"

G. Sanz-Enguita, J. Ortega, C. L. Folcia, I. Aramburu, J. Etxebarria.

Journal of Applied Physics.

"Kinetic behavior of light emission in cholesteric liquid crystal lasers: An experimental study"

J. Ortega, C. L. Folcia, G. Sanz-Enguita, I. Aramburu, J. Etxebarria.

Optics Express.

"Thermally induced light-scattering effects as responsible for the degradation of cholesteric liquid crystal lasers"

J. Etxebarria, J. Ortega, C. L Folcia, G. Sanz-Enguita, I. Aramburu.

Optics Letters.

"An azo-bridged ferroelectric liquid crystal with highly enhanced second and third harmonic generation"

Y. Zhang, J. Ortega, U. Baumeister, C. L. Folcia, G. Sanz-Enguita, C. Walker, S. Rodriguez-Conde, J. Etxebarria, M. J. O'Callaghan, and K. More.

Journal of the American Chemical Society.

Agradecimientos

Los resultados expuestos en esta tesis son el fruto de varios años de trabajo por parte de todo el grupo de investigación con el que he tenido el placer de colaborar. Sin los miembros de dicho grupo no habría sido posible esta tesis. Por ello, en primer lugar quiero dar las gracias a mis tutores Josu Ortega Aperribay y César Luis Folcia Basa. Así como a los profesores Jesús Etxebarria e Ibón Aramburu; gracias a todos. Sin olvidarme de la que durante varios años ha sido mi compañera de laboratorio y amiga Sofía Rodríguez Conde. Además, parte del trabajo llevado a cabo durante estos años habría sido imposible sin el grupo de Química Orgánica de la Universidad de Zaragoza y sin los distintos miembros que lo componen; especialmente, en el presente caso, sin Blanca ni Neli.

Durante mi penúltimo año de doctorado he tenido la oportunidad de realizar una estancia de 3 meses en la Universidad de Calabria (Italia). Durante dicha estancia colaboré con el grupo de fotónica del departamento de Física. Por la experiencia y por todo lo aprendido estoy especialmente agradecido a Gabriella, Alfredo, Josue, Pascuali, Clementina, Gia y Daniele.

En cuanto a mi vida en Bilbao, estos años no habrían sido lo mismo sin la distinta gente que ha pasado por el becádromo. Sin la gente del pintxo-pote de los jueves, especialmente Toni. Sin mis distintos compañeros de piso como Dani o Telmo, con quien además de compartir piso he compartido departamento. Y sin mis compañeros de monte Santi y Marcos.

A su vez estoy especialmente agradecido a Anna por el apoyo que me ha prestado durante todos estos años y a toda mi familia en general, especialmente a mis padres y a mi chirmán.

Por último agradecer a la UPV la beca de la que he disfrutado durante estos años.